INDIAN JOURNAL OF PURE & APPLIED PHYSICS

Indian Journal of Pure & Applied Physics

VOLUME 18   No. 4   APRIL 1980

CSIR SCIENTIFIC PERIODICALS

**JOURNAL OF SCIENTIFIC &
INDUSTRIAL RESEARCH** (monthly)

With a fine record of over 35 years' service to the scientific community, this Journal has grown into India's leading general science periodical. Intended to fulfil the responsibility of helping the research workers to keep themselves abreast of current developments in various fields of science and technology, the Journal carries editorial features highlighting important scientific events in India and abroad; articles on science policy and management of science; review articles on topics of current research interest; technical reports on international and national conferences; reviews of scientific and technical publications; and notes on major advances in various fields.

Annual subscription	Rs 60.00	£ 10.00	$ 25.00
Single copy	6.00	1.00	2.50

INDIAN JOURNAL OF CHEMISTRY (monthly)

This Journal which is running the 18th year of its publication, Consists of the following two sections.

Section A: This section is devoted to papers in Inorganic, Physical, Theoretical and Analytical Chemistry.

Annual subscription	Rs 70.00	£ 12.00	$ 30.00
Single copy	7.00	1.20	3.00

Section B: This section is devoted to papers in Organic Chemistry including Medicinal Chemistry.

Annual subscription	Rs 70.00	£ 12.00	$ 30.00
Single copy	7.00	1.20	3.00

**INDIAN JOURNAL OF
PURE & APPLIED PHYSICS** (monthly)

This Journal, which is running the 18th year of its publication, is devoted to original research communications (full papers and short communications) in all conventional branches of physics (except radio and space physics).

Annual subscription	Rs 100.00	£ 16.50	$ 42.00
Single copy	10.00	1.80	4.50

**INDIAN JOURNAL OF
RADIO & SPACE PHYSICS** (bimonthly)

This Journal serves as a medium for the publication of original rearch work (full papers and communications) in various areas of radio and space physics.

Annual subscription	Rs 60.00	£ 10.00	$ 25.00
Single copy	12.00	2.00	5.00

**INDIAN JOURNAL OF TECHNOLOGY
(INCLUDING ENGINEERING)** (monthly)

This Journal publishes papers reporting results of original research of applied nature pertaining to unit operations, heat and mass transfer, products, processes, instruments, and appliances, etc. The Journal is of special interest to research workers in the departments of applied sciences in universities, institutes of higher technology, commodity research laboratories, industrial cooperative research institutes, and industrial research laboratories.

Annual subscription	Rs 60.00	£ 10.00	$ 25.00
Single copy	6.00	1.00	2.50

**INDIAN JOURNAL OF
EXPERIMENTAL BIOLOGY** (monthly)

This Journal, devoted to the publication of research communications in the fields of experimental botany, zoology, microbiology, pharmacology, endocrinology, nutrition, etc., is the only one in India with such a wide coverage and scope.

Annual subscription	Rs 120.00	£ 20.00	$ 50.00
Single copy	12.00	2.00	5.00

**INDIAN JOURNAL OF
BIOCHEMISTRY & BIOPHYSICS** (bimonthly)

This Journal, published in association with the Society of Biological Chemists (India), Bangalore, is the only research Journal in India devoted exclusively to original research communications in biochemistry and biophysics.

Annual subscription	Rs 40.00	£ 7.00	$ 17.00
Single copy	8.00	1.40	3.50

**INDIAN JOURNAL OF
MARINE SCIENCES** (quarterly)

Commencing publication from June 1972, this Journal is devoted to research communications (full papers and short communications) pertaining to various facets of marine research, viz. biological, physical, geological and chemical oceanography.

Annual subscription	Rs 40.00	£ 7.00	$ 17.00
Single copy	12.00	2.00	5.00

RESEARCH & INDUSTRY (quarterly)

Intended to serve as a link between science and industry, this Journal is addressed primarily to technologists, engineers, executives and others in industry and trade. It publishes informative original articles containing practical details of processes and products developed in India, which show promise of ready utilization, and technical digests on new processes, products, instruments and testing methods which are of interest to industry. Developments in Indian industry are regularly reported.

Annual subscription	Rs 24.00	£ 4.00	$ 10.00
Single copy	7.25	1.30	3.50

INDIAN JOURNAL OF TEXTILE RESEARCH (quarterly)

Commencing publication from March 1976, this Journal is devoted to the publication of papers reporting results of fundamental and applied researches in the field of textiles.

Annual subscription	Rs 36.00	£ 6.00	$ 15.00
Single copy	12.00	2.00	5.00

Please contact

**THE SALES & DISTRIBUTION OFFICER
PUBLICATIONS & INFORMATION DIRECTORATE, CSIR
HILLSIDE ROAD, NEW DELHI 110 012**

CONTENTS

CONTENTS

Elastic Constants of AgCl-AgBr Mixed Crystals

U C SHRIVASTAVA

School of Studies in Physics, Jiwaji University, Gwalior 474 002

A model potential is proposed for AgCl-AgBr mixed crystals and the elastic constants are evaluated for varying compositions, and these agree excellently with the experimental values. The homogeneous strain theory has been put forward to predict the observed crystal symmetry in the AgCl-AgBr mixed crystals and to explain the change in the lattice parameter, as AgBr is added to AgCl gradually.

1. Introduction

Mixed crystals of ionic solids have been extensively studied in the past decade because of their many technological interests. The criterion for formation of mixed crystals has been discussed by Bhimasankaram[1] and the lattice parameter of mixed crystals have been studied by Slagle and McKinstry.[2] The plastic properties of many alkali halide mixed crystals have revealed that the microhardness of KCl-KBr (Ref 3) and NaCl-NaBr (Ref. 1) increases 2-3 times in the mixed crystals compared to their constituent single crystal values. The yield stress of KBr-KCl (Refs. 4, 5) mixed crystal increases enormously as one component is added to the other. But the elastic properties of mixed crystals such as elastic stiffness constants, Debye temperature of KCl-KBr (Ref. 6), KBr-KI (Ref. 7) and NaCl-NaBr (Ref. 8), melting point and Grüneisen parameter of AgCl-AgBr (Ref. 9) lie well within the constituent single crystal values. Of course, elastic properties have neither any linear relation with single crystal elastic properties nor follow the additive rule. All the above experiments on the mixed crystals have shown the existence of a crystal symmetry in them inspite of the fact that a bigger ion is substituted in the place of a smaller ion but so far we do not have any subsequent theory to explain the above fact. In order to understand such a mechanism of mixed crystals formation we extend the work of Cain[10] introducing many-body effect[11] in the mixed crystals of AgCl-AgBr crystals. The AgCl-AgBr mixed system is chosen because the crystals in this system have three distinct elastic constants (having sufficient Cauchy's discrepancies[9]). Further, silver ions being smaller ions and having poor affinity to halides are less affected by the supstitutions.

2. Theory

2.1 Stiffness of Mixed Crystals

Let us suppose that AgCl-AgBr mixed crystals form a group of isostructural crystals (AgCl and AgBr crystallizing in NaCl-like structure). Then one may expect that this group of crystals may also have some relation like the Gmelin[12] relation for alkali halides and alkaline earth oxides isostructural series, in which the stiffness has a definite relation with the atomic volume of the crystals. A plot of log f_m (f_m being the mean stiffness determined by the Hills geometrical averaging method[13] as given in Appendix and using the data in Table 1) versus the mean atomic volumes V_m (volume of unit cell for AgCl-AgBr mixed crystals) is found to be a straight line and may be represented empirically as

$$\log f_m = mV_m + c \qquad \ldots(1)$$

where m and c are the parameters of the straight line.

From Slagle and McKinstry,[2] we have seen that in mixed crystals the atomic volume V_m

$$V_m = \lambda_1 V_1 + \lambda_2 V_2 \qquad \ldots(2)$$

Table 1—Room Temperature Data of AgCl-AgBr Mixed Crystals [Ref. 9]

% AgCl	$a \times 10^{-8}$ cm	Elastic constant, $\times 10^{11}$ dyne/cm^2		
		C_{11}	C_{12}	C_{44}
0.0	2.8874	5.61	3.27	0.72
19.5	2.8665	5.61	3.27	0.70
39.1	2.8445	5.59	3.27	0.68
56.6	2.8250	5.60	3.30	0.66
78.7	2.8000	5.74	3.42	0.64
100.0	2.7750	5.97	3.65	0.62

where λ_1, λ_2 are the fractional concentrations in the mixed crystals and V_1 and V_2 are the atomic volumes in single crystals of AgCl and AgBr.

Since the single crystals of AgCl and AgBr also lie on the same line

$$\log f_1 = mV_1 + c \qquad \ldots(3)$$

$$\log f_2 = mV_2 + c \qquad \ldots(4)$$

From the properties of Eqs. (2), (3) and (4), Eq. (1) can be modified as:

$$\log f_m = \lambda_1 \log f_1 + \lambda_2 \log f_2 \qquad \ldots(5)$$

which holds for the AgCl-AgBr mixed crystals.

2.2 Model Potential for Mixed Crystals

In order to calculate the elastic constants for the mixed crystals, let us suppose that the potential for this mixed crystal group is given by:

$$\phi = - \frac{\alpha_m e^2}{r} + V_{ij}(r) + f_{ijk}(r) \qquad \ldots(6)$$

where α_m is the Madelung constant to this isostructure group, $V_{ij}(r)$ is the two-body repulsive potential limited to the nearest neighbours and $f_{ijk}(r)$ is many-body interaction which is of the form[14]:

$$f_{ijk}(r) = \sum_k f_k(r_{ij}) \frac{\epsilon(k)}{r_{ik}}$$

From the theory of Puri and Verma[14] we get expressions for the elastic constants as follows

$$C_{11} = \frac{e^2}{4\,a^4}\{A + 4.388\,B + \Delta\} \qquad \ldots(7)$$

$$C_{12} = \frac{c^2}{4\,a^4}\{-1.194\,B + \Delta\} \qquad \ldots(8)$$

$$C_{44} = \frac{e^2}{4\,a^4}\{-1.194\,B\} \qquad \ldots(9)$$

The parameters A and B are related to the second and first derivatives of $V_{ij}(r)$ through the lattice spacing (r). The parameter Δ represents the contribution of the many-body interaction and is related to Cauchy's discrepancies[14] by the relation

$$(C_{12} - C_{44}) = \frac{e^2\,\Delta}{4\,a^4} \qquad \ldots(10)$$

If we assume the two-body potential of Born-Mayer, the expressions for A and B will have the term $\exp(-r/\rho)$. Using Eq. (5) for the repulsive contributions (A and B) in the mixed crystals, we have

$$\log A_m = \lambda_1 \log A_1 + \lambda_2 \log A_2 \qquad \ldots(11)$$

$$\log B_m = \lambda_1 \log B_1 + \lambda_2 \log B_2 \qquad \ldots(12)$$

3. Calculation and Results

The parameters A_m and B_m are calculated for varying compositions of AgCl-AgBr mixed crystals using single crystal elastic constants data of AgCl and AgBr (Table 1). Values of A_m and B_m are presented in Table 2. The remaining third parameter Δ_m arising due to many-body interaction is yet not possible to calculate theoretically, since the behaviour of the many-body effect in mixed crystals is much complicated. At this stage, parameter Δ_m is calculated from the experimental values of Cauchy's discrepancies in mixed crystals using Eq. (10) and these are also presented in Table 2.

Elastic constants of mixed crystals are calculated using Eqs. (7)-(9) and the variation of these theoretical elastic constants with concentration of AgCl in the mixed crystals has been plotted alongwith the experimental values[9] (Fig. 1). We see that the agreement between the theoretical and the experimental values of the elastic constants is fairly good.

4. Discussion

Repulsive interaction may be of Born-Mayer type in mixed crystals, constituting of two components and the parameters A_m and B_m will be expressable in the form : $b'\exp(-r/\rho_m)$. Proper analysis of Eqs. (11) and (12) leads to:

$$(\rho_m)^{-1} = \lambda_1\,(\rho_1)^{-1} + \lambda_2\,(\rho_2)^{-1} + (\log b_m$$
$$-\lambda_1 \log b_1 - \lambda_2 \log b_2)/r \qquad \ldots(13)$$

Eq. (13) shows that the inverse of the effective range parameter in the mixed crystals has a linear relation with the inverse of range parameters of the constituent single crystals. The following condition for the stability is frequently obeyed by the mixed crystals:

$$B = -1.165\{1 + 12\,f(r)\} \qquad \ldots(14)$$

where $f(r)$ is the force of the many-body interactions. From this theory we see that mixed crystals of AgCl-AgBr are cubic symmetric in which the Coulomb forces are balanced by the repulsive and many-body forces. Coulomb forces in AgCl-AgBr

Table 2—Calculated Values of Parameters for AgCl-AgBr Mixed crystals

% AgCl	λ_1	λ_2	A_m	B_m	Δ_m
0.0	0.000	1.000	6.8856	−0.7277	3.0772
19.5	0.195	0.805	6.5603	−0.6852	3.0124
39.1	0.391	0.609	6.2489	−0.6450	2.9434
56.6	0.566	6.434	5.9823	−0.6112	2.9191
78.7	0.787	0.213	5.6640	−0.5709	2.9667
100.0	1.000	0.000	5.3724	−0.5346	3.1194

228
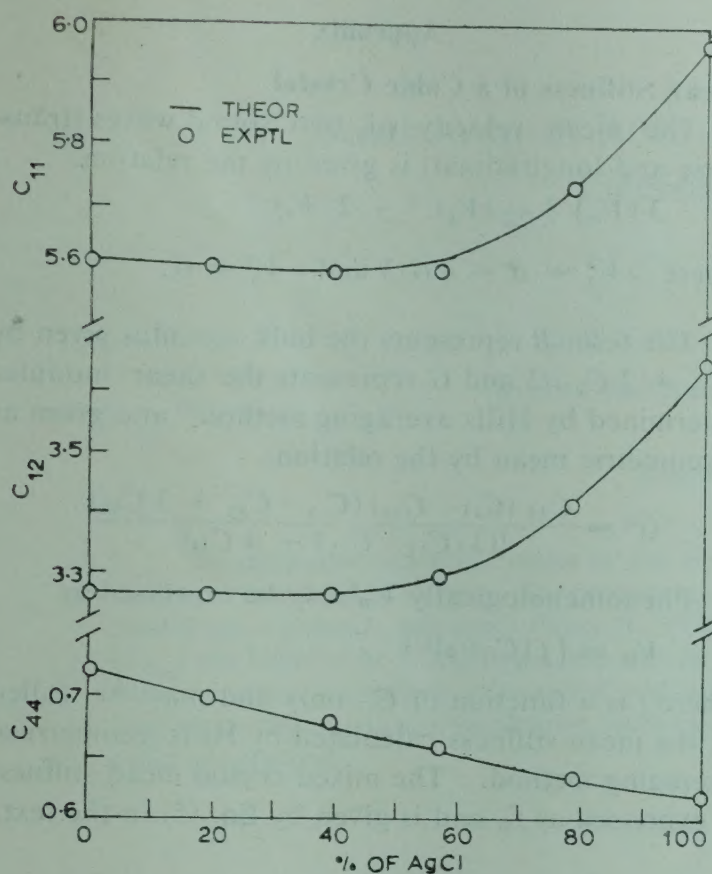
Fig. 1—Variation of elastic constants C_{11}, C_{12} and C_{44}
($\times 10^{12}$ dyne/cm^2) of AgCl-AgBr mixed crystals
with concentration of AgCl (in molar %)

are as simple forces as in any single crystals and the repulsive interaction have some definite contribution to its constituent repulsive interactions. The many-body interaction, which in this case is limited to three-body interaction between nearest neighbours only, is not yet well defined and for this we are still dependent on the experimental values of Cauchy's discrepancies and have to make use of the relation reported by Puri and Verma[14] for single crystals.

The present study shows that the mixture of AgCl-AgBr has a crystal structure with cubic symmetry and this observation is confirmed by the experimental studies. We may conclude that the mixed crystals do not get distorted even by substitution of ions of different sizes. However, the difference in the sizes is small and it appears that in mixed AgCl-AgBr crystals Br$^-$ ions remain compressed. Such compression of ions will not show any external evidence since the spacing between two ions is not the sum of the radii of the spheres of two ions made of some perfect rigid materials but is really the distance at which the attractive and the repulsive forces are in balance. In phase transition of KBr from the NaCl-structure to that of CsCl-structure, Br$^-$ ions are subjected to a change in the lattice spacing of 0.179×10^{-8} cm (Ref. 15). This value is much larger compared to the change in the lattice

spacing of 0.112×10^{-8} cm suffered by Br$^-$ ions in the AgCl-AgBr mixed crystals. Any substitution not only changes the ion at that very point, but also affects all the six nearest neighbours and twelve next nearest neighbours and so on, through the elastic forces. So whatever strain is produced due to substitution, is uniformly distributed throughout the crystal by means of coupling between neighbours. This is why we get the expansion in the lattice as AgBr is added in AgCl, unlike in the case of doping in which substitutional sites are relatively very small and hence distortion in lattice and local elastic constants are different.[16] In mixed crystals, substitutions affect number of sites and the strain fields of elastic forces due to substitutions overlap each other. This results in a homogeneous redistribution of the lattice points tending towards the crystal symmetry satisfying the crystal stability condition and giving rise to the observed lattice expansion as AgBr is added in AgCl, or contraction in lattice as AgCl is added in AgBr gradually. However, no relation between the resulting lattice parameters could be obtained.

5. Conclusion

It is obvious that in AgCl-AgBr mixed crystals, the number of Cl$^-$ ions are comparable to the number of Br$^-$ ions and hence the local distortion in the lattice points may not be as simple as in the case of doped single crystals, but as we add AgBr in AgCl, the number of substitutions of Cl$^-$ ions with Br$^-$ ions is comparable to the number of Cl$^-$ ions in AgCl-AgBr mixed crystals. The strain fields of elastic forces produced due to these substitutions overlap each other. Due to this overlapping, the interaction system tends towards stability after a homogeneous redistribution of the strain throughout the lattice, in which coulomb forces are now balanced by the repulsive and many-body forces, giving rise to a change in lattice parameter. Hence a simple model based on the above three (Coulomb, repulsive and many-body) interactions would be able to explain the elastic properties of mixed crystals.

References

1. Bhimasankaram T, *Defect studies of* NaCl-NaBr *mixed crystals*, Ph D thesis, Osmania University, Hyderabad, 1974.
2. Slagle O D & McKinstry H A, *Acta Crystallogr.*, **21** (1966), 1013.

3. Stoloff N S, Lezius D K & Johnston T L, *J. appl. Phys.*, 34 (1963), 3315.
4. Kataoka T & Yamada T, *Japan J. appl. Phys.*, 16 (1977), 1119.
5. Kataoka T, Umatsu T & Yamada T, *Japan J. appl. Phys.*, 17 (1978), 271.
6. Sharko A V & Botaki A A, *Izv. Vuz. Fiz.*, 12 (1971), 126.
7. Botaki A A, Gyrbu I N & Sharko A V, *Izv. Vuz. Fiz.*, 6 (1972), 150.
8. Avericheva V E, Botaki A A, Dvornikov G A & Sharko A V, *Izv. Vuz. Fiz.*, 4 (1974), 148.
9. Cain L S, *J. Phys. Chem. Solids*, 38 (1977), 73.
10. Cain L S, *J. Phys. Chem. Solids*, 37 (1976), 1178.
11. Sarkar A K & Sengupta S, *Proc. Nuclear Phys. and Solid State Phys. Symp.*, (Department of Atomic Energy, Government of India, Bombay 1) 12c (1969).
12. Gmelin E, *Z. Naturf.*, 25a (1970), 887.
13. Hill R, *Proc. phys. Soc. Lond.*, A65 (1952), 349.
14. Puri D S & Verma M P, *Solid State Commun.*, 18 (1976), 1295.
15. Sarkar A K & Sengupta S, *Phys. Status Solidi*, (b) 58 (1973) 775.
16. Kesharwani K M & Agrawal B K, *Phys. Rev.*, B9 (1974), 3630.

Appendix

Mean Stiffness of a Cubic Crystal

The mean velocity of two sound waves (transverse and longitudinal) is given by the relation.

$$3 (V_m)^{-3} = (V_1)^{-3} + 2 (V_t)^{-3}$$

where $\rho V_1^2 = B + 4 G/3$ and $\rho V_t^2 = G.$

The term B represents the bulk modulus given by $(C_{11} + 2 C_{12})/3$ and G represents the shear modulus determined by Hills averaging method[13] and given as a geometric mean by the relation:

$$G^2 = \frac{C_{44} (C_{11} - C_{12}) (C_{11} - C_{12} + 3 C_{44})}{[(3 (C_{11} - C_{12}) + 4 C_{44}]}$$

Phenomenologically V_m may be expressed as

$$V_m = [f(C_{ij})/\rho]^{1/2}$$

where f is a function of C_{ij} only and may be called as the mean stiffness calculated by Hills geometrical averaging method. The mixed crystal mean stiffness is expressed as f_m and is given by Eq. (5) in the text.

Breakdown of RbCl Films Due to Application of Electric Voltage Pulses

B R YADAV & R K SHRIVASTAVA

Physics Department, University of Saugar, Sagar

On application of voltage pulses in the frequency range 100Hz-100kHz, breakdown was observed in rubidium chloride (RbCl) films. The processes in this breakdown were analogous to those occurring in dc breakdown. [*Indian J. pure appl. Phys.*, 16 (1978), 861]. The maximum value of voltage pulse for breakdown (V_{Pm}) was found to be 5-20% larger than that for dc voltage (V_{dm}). V_{Pm} was also measured as a function of pulse frequency, for various pulse widths. Micrographs of pulse breakdown of RbCl films were also obtained from which the initiation of breakdown and its subsequent development with other factors mentioned above, could be visualized.

1. Introduction

Investigations of dc breakdown in RbCl film and bulk have been reported in our previous papers.[1] Now-a-days, the insulating films are used extensively in electronic and integrated circuits. The electric field operative on the insulating films could achieve values greater than 10^6 V/cm. It is also advantageous to carry out tests on capacitor samples with self-healing and non-shorting breakdowns. A large number of exploratory experiments can be carried out on one sample, as the follow-up current does not destroy the evidence of a single breakdown event. Dean observed in 1910 that the breakdown was initiated at certain regions called 'spots'. There was no short-circuiting produced in such capacitor samples, because the thin electrodes (thickness less than 2000 Å) do not completely melt but evaporate at the breakdown spots. The breakdown experiments can be repeated, therefore, on one specimen many times. Klein[2] and Klein and Burstein[3] have investigated the mechanism of the breakdown process on self-healing specimen. They had suggested the formation of a conducting channel in the insulator followed by the discharge of electrostatic energy, causing destruction mainly by evaporation. The breakdown was interpreted to consist of a succession of processes,[3] viz. (1) triggering of breakdown by an extremely small charge or current pulse due to the field; (2) thermal runaway induced by the temperature rise produced by the first process and (3) local destruction of the energy stored in the specimen by the full establishment of the discharge.

2. Experimental Details

2.1 Samples and Equipment

Test samples were thin-film capacitors produced by evaporation of RbCl at a pressure of 10^{-5} torr on 1mm thick glass slide as substrate. The aluminium electrodes were of about 1500 Å thickness, ensuring self-healing breakdowns. The RbCl film thickness was about 1000Å. About 100 capacitors were deposited with the same technique as reported earlier.[1] The voltage source used in this study was a pulse generator, type PG 850, having a calibrated voltmeter, with facility to change the frequency and the pulse width of the output voltages. The leakage current was measured with the Universal AVO meter having least count of 10^{-6}A. The series resistance R_s varied between 10 kΩ and 20 kΩ and this was sufficient to control propagating breakdown. The electrical circuit diagram is shown in Fig. 1.

2.2 Observation of the Breakdown

The dc breakdown was determined by the usual method, with series resistance R_s connected to the dc source. The V-I characteristics were determined with the help of the pulse generator. The rectangular voltage pulses were applied directly to the specimen as shown in Fig. 1. As soon as the critical breakdown voltage was reached, a few transient pulses appeared on the CRO screen as shown in Fig. 2(a). Further increase in the voltage produced a complete break-up of the horizontal trace [Fig. 2 (b)] on the screen, indicating that the process was much faster and more discharge current flowed through
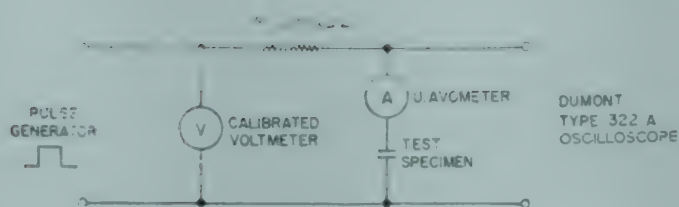
Fig. 1—Electrical circuit diagram for obtaining, *V-I* characteristics
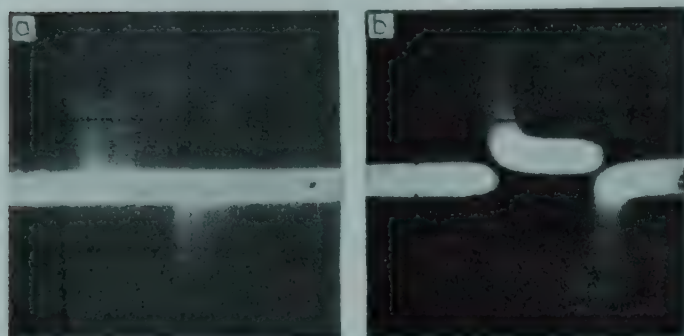
Fig. 2—(a) The oscillogram corresponding to critical pulse breakdown: (b) Oscillogram showing stable break-up in trace corresponding to pulse breakdown

the system. These observations were found to be essentially the same for most of the present studies.

Micrographs of the tested samples at the initial stage and subsequent stages of breakdown were taken with transmitted light using an optical microscope, having magnification 10×10 and 10×40.

3. Results

The *V-I* characteristics for the maximum dc. and pulse breakdown are shown in Fig. 3. It is seen that the maximum pulse breakdown value for a pulse width of 10 μsec at 100 Hz frequency is found 20% larger than maximum dc breakdown value. The curves show, linear rise in current followed by an exponential rise for dc voltages. However, in case of voltage pulse, the current remains nearly constant over the low voltage region, finally showing the fast exponential rise as the breakdown voltage is reached. Fig. 4 indicates the variation of leakage current with voltages, for various pulse widths at 100 Hz pulse frequency. A similar variation in current is observed for all the pulse widths used. Fig. 5 shows the relation between the maximum breakdown voltages and pulse frequencies, for various pulse widths. This is found to be practically constant in the 100-1000 Hz pulse frequency range; beyond this range V_{Pm} decreases as shown on a logarithmic scale.

Figs. 6 a-f exhibit magnified micrographs of pulse breakdown of RbCl films. As soon as the breakdown value is reached, the film which was initially opaque and smooth (Fig. 6a), becomes full of spots (scratch-like) distributed randomly (Fig. 6b) Some spots are

wider in extension than others. The increase in voltage produces well defined rings (pores) (Fig. 6c). This may correspond to the initiation of breakdown through material with maximum cross-section towards the anode. Further increase in voltage produces bright active regions with a few small dark spots inside which are also well defined (Fig. 6d). This may be interpreted as the situation corresponding to breakdown through both the upper and lower electrodes as well as the film material. However
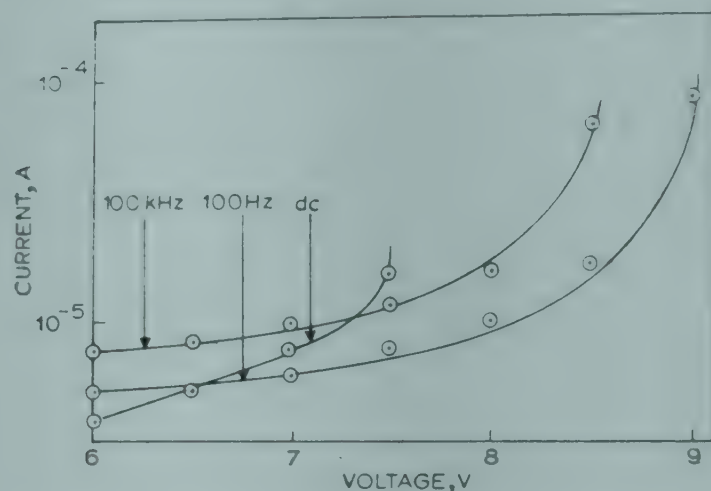
Fig. 3—Maximum breakdown voltages for various pulse frequencies at 10 μ sec pulse width
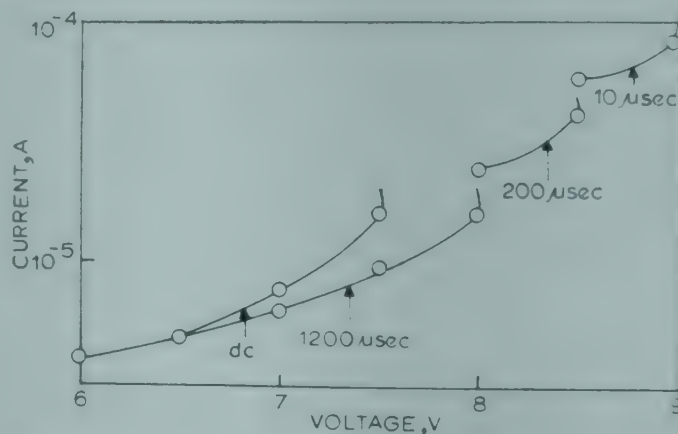
Fig. 4—Maximum breakdown voltages for various pulse widths at 100 Hz pulse frequency

Fig. 5—Maximum breakdown voltage variation with pulse frequency for different pulse widths
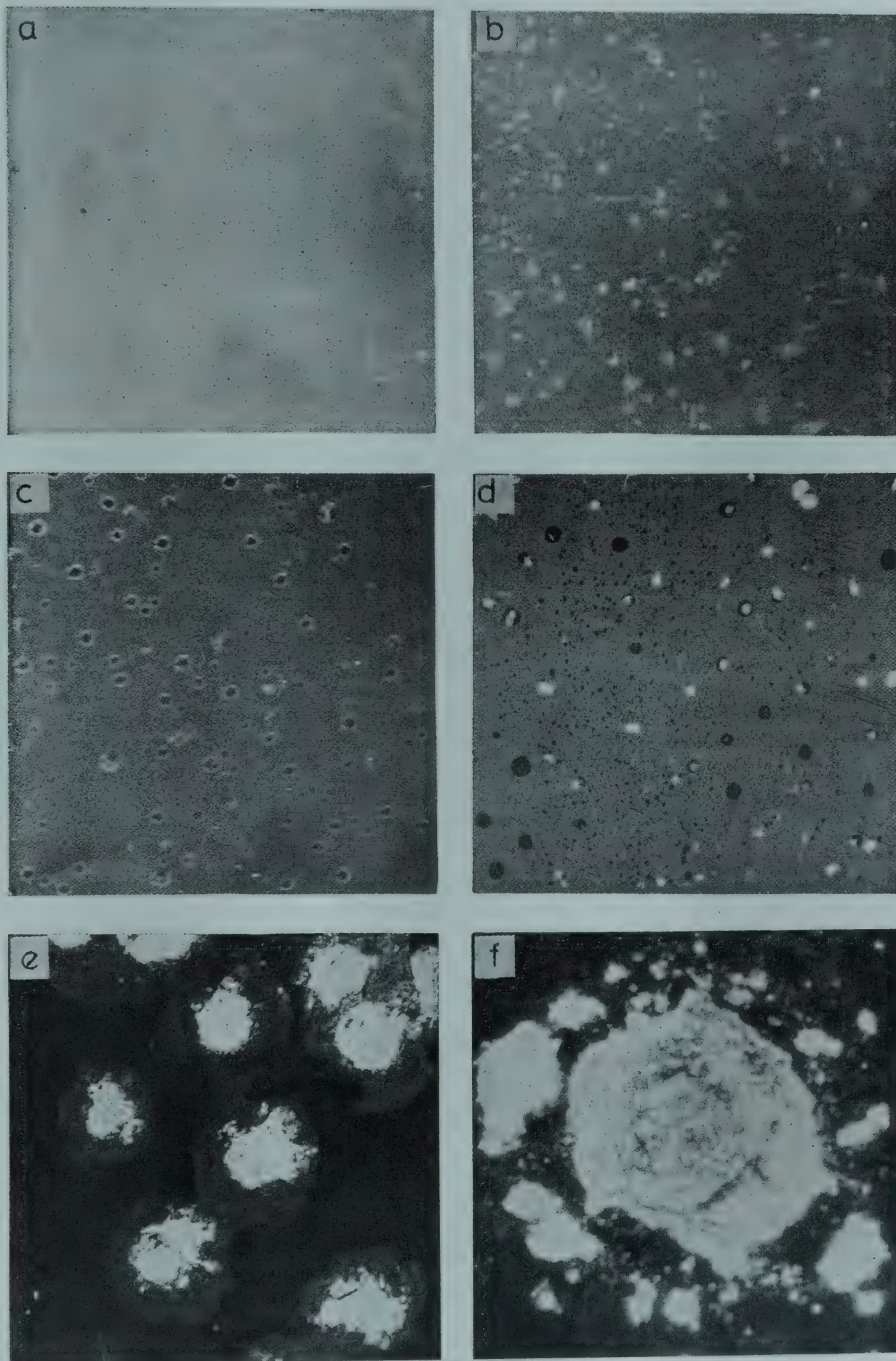
Fig. 6—Magnified micrographs at different stages of breakdown in RbCl films: (a) opaque and smooth surface; (b) scratch-like spots; (c) rings (pores) showing material and anode both damaged; (d) stage of dark and bright spots; (e) advance stage of propagating breakdown: and (f) (10×40) magnified bright spot.
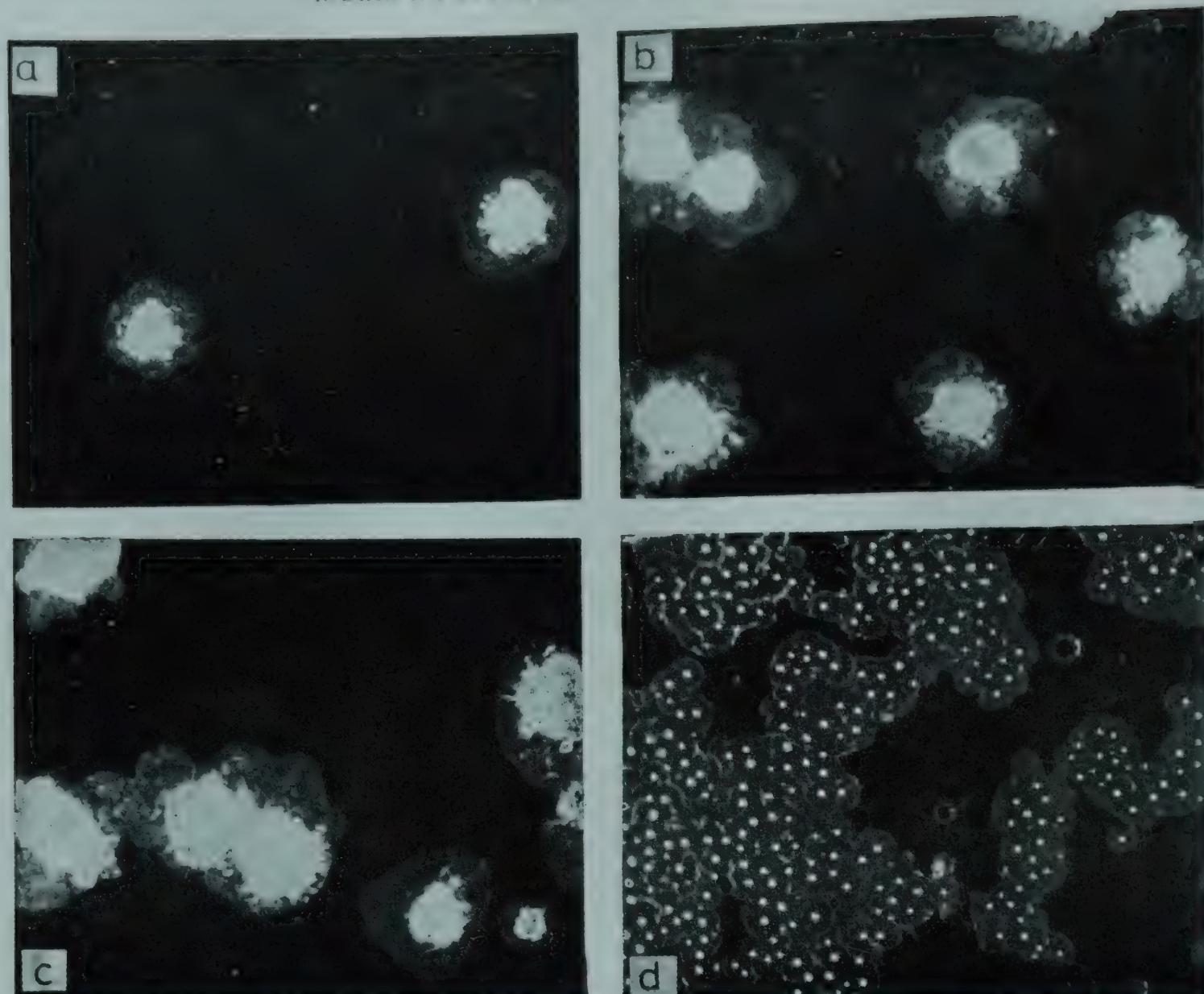
Fig. 7—Micrographs showing breakdown of RbCl films

	Serial resistance R	Pulse frequency Hz	Pulse width μ sec
a	10	100	10
b	10	100	1200
c	10	105	1200
d	20	100	10

there are some additional dark spots corresponding to the single hole breakdown only through the material. At maximum breakdown voltages the bright spots appear to be irregular in shape corresponding to large breakdown area (Fig. 6e). If an objective with more magnifying power (10 × 40) is used to view one of these big bright spots, the micrograph thus obtained (Fig. 6 f) shows the propagating mechanism in the surrounding region of a big spot. Besides these, a series of micrographs (Fig. 7a-d) are also taken with different combinations of the following parameters: (1) serial resistance (2) pulse width (3) pulse frequency.

4. Discussion

Earlier studies of Klein,[2] and Klein and Burstein[3] showed that the breakdown voltage of thin films could be broadly classified into three stages according to the voltage applied to the specimen.

(1) At a critical voltage, the CRO observation (Fig. 2a) shows the presence of a few pulses which may also correspond to the appearance of rings (pores) on the film (Fig. 6c). This is the first stage called single hole breakdown in the film at weak spots on the material.

(2) The second stage is reached at a slightly higher voltage when pores are changed into bright spots

and grow due to the propagation of breakdown. This is also shown by the appearance of break-up in the CRO trace (Fig. 2b). The electrode material evaporates at this stage as suggested by Klein.[2]

(3) Finally when the voltage is further increased, these spots grow wider showing melting of material and evaporation of the electrodes. This voltage has been referred to as the maximum breakdown voltage in the present studies. However, a serial high resistance is used in the experiment to minimize the damage by propagating breakdown at this stage (Fig. 7d).

The *V-I* curves are exponential in nature and can be explained in the same way as in the earlier communication.[1] The maximum pulse breakdown voltage is larger than maximum dc breakdown value (Fig. 3). This may be explained as follows. The thin film has a poly-crystalline structure in which poly-crystals are separated by small spaces. This is electrically equivalent to a number of capacitors joined in series and consequently its pulse impedance is less than that for dc voltages. This results in a greater flow of current and hence the pulsed voltage-current characteristics are much above the dc characteristics at low voltages. However, with the application of dc voltages, Joule heat is evolved in the film, resulting in providing a conducting channel for the mechanism to progress without any possible hindrance. Consequently, the breakdown stage is reached but the same stage is likely to be reached at higher voltages when the pulsed voltages are applied. This is due to the fact that the periodic application of the voltage pulse, results in a discontinuous heat input in the material with a quiescent interval. This results in providing a comparatively weaker channel. Therefore, the breakdown voltage needed in this case is expected to be greater than dc breakdown value.

As the duration of the pulse width increases, the voltage becomes operative for a greater length of time and, therefore, is useful in providing greater heat input to the film. Hence V_{Pm} decreases with increase in the width of the voltage-pulse as shown in Fig. 4.

Klein and Levanon[4] have shown theoretically that V_{Pm} is independent of frequency in the lower frequency range (up to 1000 Hz). However, the pulse frequency influences the dielectric loss in the material which is noticeable only above 1000 Hz frequency, the process of polarization in the material increases the dielectric loss which appears in the form of heat. This is in addition to the Joule heat corresponding to the leakage current referred to earlier. Thus the magnitude of V_{Pm} decreases with the rise in frequency of the voltage pulse.

The breakdown mechanism can be further elaborated as proposed by Frohlich[5] and Seitz.[6] According to the theory, impact ionization initiated by a single electron statistically available at the cathode produces an avalanche which by diffusion grows like a cone with maximum cross-section towards the anode. On breakdown of the material at a weak spot, the heat produced by electrons in the avalanche may cause destruction at the anode (Fig. 6c). The avalanche process serves to trigger the destructive breakdown by producing a considerable rise in temperature in the channel. The increase in the electrical conductivity caused by the temperature rise, is sufficient to make the breakdown channel thermally unstable. As the applied voltage increases, the destruction starts in the channel and finally leads to breakdown (Fig. 2b).

It may also be suggested here that a big spot can be formed if the 'effective work function' of the material is quite low. This is further reduced due to heat formation at the spots resulting in wider spots (Fig. 6e). However, when the current available is low as happens for higher resistance, many spots with low work function provide the initiating triggering electrons.

Thus the breakdown mechanism may consist of three consecutive stages: (1) a conductive channel is formed by the initiating breakdown process in the film material (Fig. 6b); (2) the energy being stored in the micro-condenser, discharges through the channel causing melting of material and evaporating the electrodes; and (3) the propagating mechanism with energy being continuously supplied from the source.

Acknowledgement

References

1. Yadav B R & Shrivastava R K, *Indian J. pure appl. Phys.*, 16 (1978), 861.
2. Klein N, *Adv. Electron., Electron Phys.*, 26 (1969), 309.
3. Klein N & Burstein E, *J. appl. Phys.*, 40 (1969), 2728.
4. Klein N & Levanon N, *J. appl. Phys.*, 38 (1967), 3721.
5. Frohlich H, *Report of the British Electrical and allied industries Research Association L/T.* 113, 1940.
6. Seitz F, *Phys. Rev.*, 76 (1949), 1376.

Dislocation Velocities in Zinc Single Crystals*

RAHUL BASU†

Indian Institute of Science, Bangalore 560 012

Seeger's equation describing wave-like propagation in the processes of plastic deformation is studied by the use of Laplace transform and perturbation analysis and dimensionless parameters obtained. The variation of the Peierls stress with the interparticle spacing is evaluated. Experimental results for the yield point in zinc single crystals are studied. It was found that there are two distinct regions in the stress-velocity (strain) curves. The sudden change at 24 Mdyne/sq cm in the deformation characteristics is attributable to the presence of interstitials such as nitrogen atoms and clusters and Zn_3N_2 precipitates. The interparticle spacing is 10 microns.

1. Introduction

The object of the present paper is to obtain a theoretical expression connecting the internal motion of dislocations subjected to certain boundary cons-traints, to the macroscopic mechanical behaviour of the crystalline material, viz. zinc single crystal. In the process, various parameters are obtained, and the solution of the differential equation gives an expres-sion relating the strain with the stress and the inter-particle spacing. This equation holds true only for pinned lines. Even before the dislocation line has broken free of the constraining precipitates and inter-stitial impurities that make up the so-called Cottrell atmosphere, the fracture process starts. This is not treated in the present work.

The ultimate tensile strength (UTS) and the lower yield point (elastic to plastic transition) can be connected to the interparticle spacing l by the Ansel and Lenel[1] or the Peckner[2] expressions: $\sigma = \sigma_0 + kl^{-1/2}$ and $\sigma = \sigma_0 + C \exp(-l)$. These expressions are valid both in the elastic as well as the plastic regions up to the fracture initiation at a stress typically of the order of $G/10$, where the breakaway from the Cottrell atmosphere occurs. For the elastic region ($10^{-2}G$ to $10^{-4}G$) the well known Hooke's law applies, where the stress is linearly proportional to the strain, and this proportional ratio gives the elastic modulus. Garland and Plateau[3] have given an expression for the strain at rupture for a material containing inclu-sions. It is presumed that thermal activation is negligible within the limits of experimental error. The conditions of the experiment do not permit any appreciable thermal motion of the dislocation lines. This can be clearly seen by calculating the diffusive velocity as in Hirth and Lothe,[4] where the coefficient is found to be approximately $10^{-4} \exp(-76)$ and the corresponding velocities are thus negligible. This of course, can be easily confirmed by optical microscopy. The presence of the yield point is attributed to the presence of point obstacles such as interstitials, and inclusions or precipitates which impede the passage and motion of dislocations. The general effect of the solute is to raise the yield point which results from deformation after dislocations are locked in position.[2-5]

It is not possible to avoid the absorption by the crystalline material of interstitials from the environ-ment. This might happen during preparation, anneal-ing, or testing. Of course, when initial preparation is done by cleaving the bulk crystal in liquid nitrogen, a major source of contamination occurs. As far as this particular research is concerned, it is incidental to the main idea of the formulation of the Boundary Value Problem (BVP), solving this and evaluating certain parameters and verifying experimental results. Suffice it to say that the local pinning is very strong, between interstitial and line, and unpinning occurs at a stress typically about $G/10$. This might occur with the presence of voids, cavities and high stress concentration factors. However, when dealing with single crystals, and in the stress range of the experi-ment, the value $G/10$ quoted by Hirth and Lothe[4] is not attained.

2. Experimental Details

The experimental equipment consisted of the usual apparatus for these type of researches, viz. a

Hopkinson's bar with attached strain gauges. The stress was produced by an impacting steel projectile with a curved impacting surface providing for central impact. This projectile caused a short stress pulse to travel through the equipment with the specimen attached, and the rise time of the stress wave was 10 μ sec, thereby preventing the excitation of significant radial vibrations and dispersion. An oscilloscope was also used in connection with the strain gauges to record the stress waveform during each test and this pulse was photographically recorded after calibration, for each specimen tested. Calibration was effected by performing a reference test with a known impacting velocity and known stress level, viz. impact stress $= 1\cdot29 \times 10^6 \, V$ dyne/cm^2.

Slip occurs on the pyramidal and basal systems of the crystalline specimens (hcp zinc). The crystalline geometry is illustrated in Fig. 1.

After cleaving in liquid nitrogen, the crystals were subsequently oriented by X-ray Laue diffraction on a goniometer, acid lapping and repeating the process. All orientations were $\pm 0\cdot3$ degrees. As prepared crystals had an orientation and geometry such that the pyramidal systems and basal systems occurred on the faces of the specimen of rectangular cross-section. Observation of the slip processes was then easily performed directly on these faces, where the pyramidal system $(\bar{1} \, 2 \, \bar{1} \, 2) \, (1 \, \bar{2} \, 1 \, 3)$ and the basal system $(0001) \, (1 \, 0 \, \bar{1} \, 0)$. After preparation, the specimens were annealed in an atmosphere of argon. A resultant impurity content of $0\cdot001\%$ may be taken as an acceptable figure, and the crystals as supplied for experiment had a purity of $99\cdot999\%$.
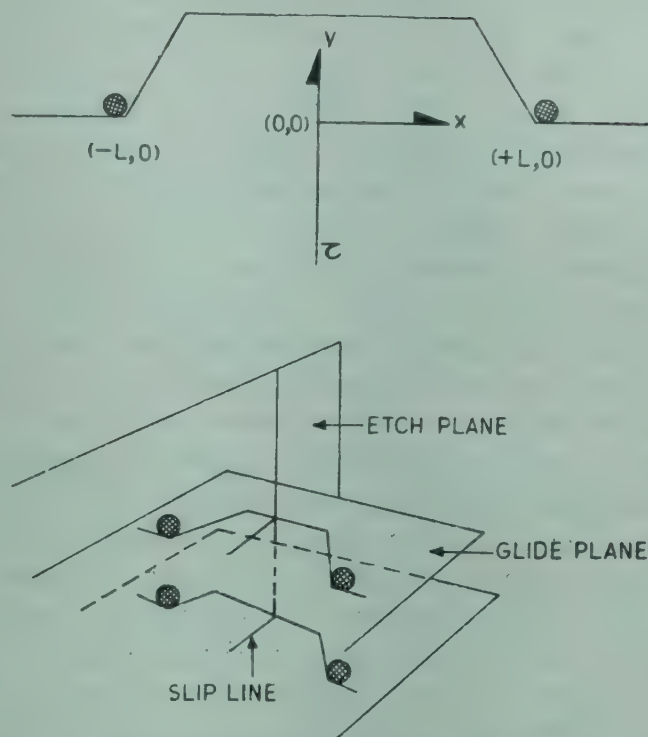
Fig. 2—Coordinates and geometry of the BVP

X-ray Berg Barrett photography and chemical means were used to reveal the slip lines on the appropriate planes. The chemical etch was always far more effective than the X-ray method. A possible mechanism for production and occurrence of slip lines by such an etching process is illustrated in Fig. 2. The stress level on the basal plane and basal slip system is the measured stress, whereas on the pyramidal slip system, the stress level is given by $0\cdot41 \, \tau \, (t)$, and the impulse given by integrating over the pulse duration, i.e. $0\cdot41 \int \tau \, (t) \, dt$, where $\tau \, (t)$ is the compressional stress. It is postulated that the slip on basal planes is solely due to the screw component of the dislocation, and the slip on the pyramidal planes is due to the edge component. These are made apparent by etching and are of sufficient magnitude to be measured optically, whereby the velocity of the dislocation line is given by taking the average slip length over the stress duration or time of slip. This averaging procedure is further carried by making measurements over parallel surfaces and thus mullifying the effect of bending moment due to off-centre loadings.

3. Results and Discussion

It is found experimentally, that there are two distinct regions to the stress-dislocation velocity curve. It follows that the stress-strain curve also follows the same behaviour, since the strain is derivable from the strain rate given as $e' = \rho \, b \, V$, where ρ = dislocation density, b = magnitude of Burgers vector, and V = velocity of dislocations. Since the time of movement is known from the stress loading,
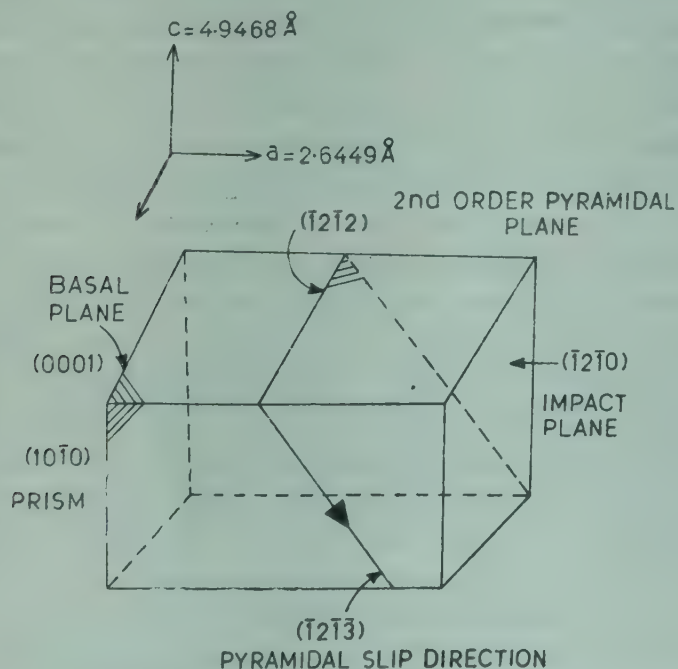
Fig. 1—Specimen orientation and major slip systems and planes

the strain is derivable by integrating the strain rate over time. The transition is sharp and clearly defined, and divides the two sections into an elastic and a plastic region. The yield point, which is the transition point in Fig. 3 appears at approximately 10 cm/sec and 24 Mdyne/cm². In Zn as in hcp crystalline materials, the Peierls stress is of a lesser magnitude compared to the other interaction stresses in the crystalline lattice. According to Dorn and Rajnak,[6] the effects of thermal agitation are slight, the main parameter being τ/τ_p, and also the shape of the lattice potential is unimportant. In the following analysis, the lattice potential is assumed as sinusoidal, without loss of generality. At 0 K, the transition stress gives a good indication of the Peierls stress, for a pure lattice. Yokobori[7] gives a detailed discussion of the components comprising the transition stress, and this stress is termed the region 2 transition from elastic to plastic regions. The Burgers vectors and the Peierls stresses are not the same for the two components of the dislocation beyond the elastic region, and correspondingly, cross slip on more than one plane can occur.[7] Ashby[5] also postulates this. Clearly this mechanism is highly probable in the second portion of the diagram (Fig. 3), and in fact the edge and screw components appear to follow different characteristics on this figure after the transition stress is reached. Since the breakaway stress signifying the onset of fracture typically occurs about a stress level of $G/10$ or 10,000 Mdyne/cm², it is unlikely that this is the mechanism causing the observations in Fig. 3 beyond the critical stress.[4]

In the following analysis, the concept of the Peierls stress arising from the interatomic potential of the crystal lattice is of crucial importance.
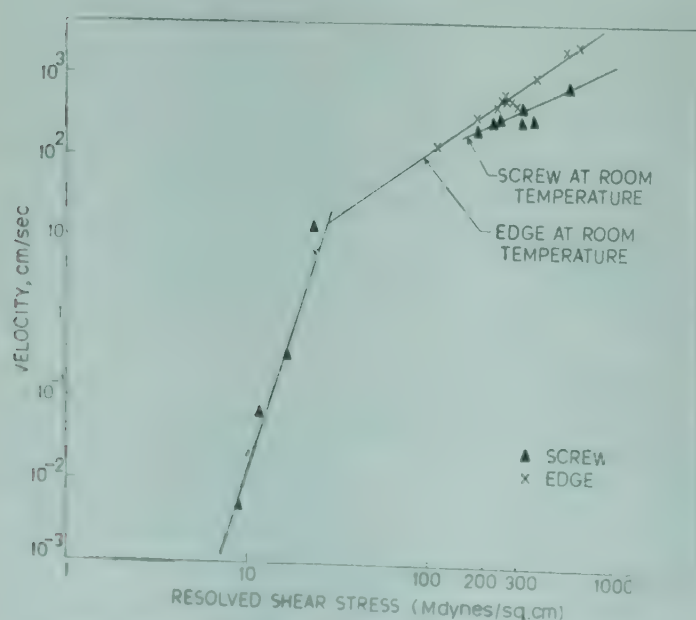
Fig. 3—Resolved shear stress versus dislocation velocity in zinc single crystals at 300 K

Together with this force, there are other stresses and forces caused by inclusions, imperfections, voids, cavities and other dislocation arrangements in the lattice. A straight dislocation line has its minimum energy when it lies in a potential trough parallel to lines of closest packing in the slip plane. Motion of such a line from one valley to the next requires change of geometry and bonding. The Peierls stress is the minimum shear stress required to promote forward motion of the line, the temperature dependence of which is given by $\tau_p = \tau_0 \exp(-AT)$ having its extreme at absolute zero. Assuming the dislocation line to be pinned by two impurity atoms, particles or inclusions a certain distance apart, the motion of this line under an applied shear stress is then impeded by friction and forces from the other disturbances of the perfect, crystalline lattice. This pinning of the dislocation line causes the appearance of the yield point, which does not appear in perfect lattices and absolutely pure material. The occurrence of the yield point in zinc has been attributed to the presence of nitrogen in very minute, trace quantities.[8-10] This could happen by absorption from the atmosphere, a very plentiful and inexhaustible supply of N_2. Another more concentrated source is the liquid nitrogen in which the bulk sample is placed when cleaving to produce a reference basal plane, as the crystal shears easily on the basal planes, the lattice spacing between these parallel planes being $c = 4\cdot9468$ Å as compared to $a = 2\cdot6449$ Å in the basal plane systems. According to Sommer,[10] the average distance is $2L = b/c^{1/3}$, where b is the magnitude of Burgers vector and c the concentration of the solute.

The numerical concentration is a rather high number, being $3\cdot1 \times 10^{17}$ per cc of zinc for $0\cdot001\%$ solute and similarly for $0\cdot0001\%$ solute it is less by a factor of 10. Yokoboru[7] states that even $0\cdot0001\%$ trace interstitial nitrogen is sufficient to cause the yield phenomenon. This is what has been observed experimentally (Fig. 3) and the only logical explanation is to follow the ideas of these researchers. Assuming a random distribution within the surface layers after absorption, the interstitial nitrogen then should occupy all positions in the lattice, with a certain inter-particle spacing. As one proceeds towards the interior of the crystal away from the surface, the concentration decreases and thus the inter-particle spacing increases, as the absorption takes place by diffusion from the surface. The process of etching away the surface layers of the specimen shows that this is indeed the case, the slip lines becoming less in number and eventually disappearing after sufficient surface layers are removed. It then appears that most of the deformation occurs within a small layer near

the surface, as the pinning points responsible for this reside there. The Peierls stress also varies with the level of impurity concentration, and should also decide the resultant characteristic behaviour. An expression for the variation of this stress with the solute level has been derived in the following analysis.

3.1 Mathematical Analysis and Solution

An expression for the slip of the line pinned at its extremities is given by Seeger[11] as

$$E(y)\frac{d^2y}{dx^2} = \frac{dE(y)}{dy} - b\tau + m\frac{d^2y}{dt^2} \qquad ...(1)$$

where $E(y)$, the energy per unit length of the line, is given by

$$E(y) = \alpha_1 \cos \frac{2\pi y}{a} - \alpha_2 \cos \frac{4\pi y}{a} \qquad ...(2)$$

$$(E_0 >> \alpha_1 >> \alpha_2)$$

where $m =$ mass per unit length of the line; $\tau_p =$ Peierls stress; $a =$ lattice parameter; $b =$ Burgers vector; and $\sigma =$ applied shear stress.

The boundary conditions for this problem are $dy/dx = 0$ at $x = 0$ and $y = 0$ at $x = \pm L$. Fig. 2 gives a graphical description of the coordinates. Eq. (1) can be solved by methods such as the Laplace transform and perturbation analysis, provided that some simplifying assumptions are made, viz. small displacement (y is small) and steady state is attained so that the term in time is neglected. For small y, the sine and cosine terms can be replaced by the values y and 1 respectively. Expression (2) is then substituted for $E(y)$ in (1) and after performing some algebra and calculus, the resulting linearized equation is:

$$(E_0 - \alpha_1 - \alpha_2)\frac{d^2y}{dx^2} = \frac{4\pi^2 y}{a^2}(\alpha_1 + 4\alpha_2) - b\tau \quad ...(3)$$

Since $\alpha_1 >> \alpha_2$, the solution becomes quite straightforward, as Eq. (3) is linear.

For a more exact solution taking the non-linearity into consideration, the procedure is as follows: the variables in Eq. (1) are scaled and non-dimentionalized, and a suitable small parameter chosen to facilitate the perturbation expansion. This is done as follows:

Choose $y = aY$, $x = a(E_0/2\pi\alpha_1)^{1/2} X$, $\bar{t} = Tt$, $\epsilon = \alpha_1/E_0$ where X, Y and T are the new non-dimensionalized variables. The boundary conditions are then

At $X = 0$, $dY/dX = 0$, and $Y = 0$ at $X = \pm L/a(2\pi\epsilon)^{1/2}$

Assuming a solution in a series type expansion of the form

$$Y = Y_0 + \epsilon Y_1 + \epsilon^2 Y_2 + \cdots \qquad ...(4)$$

the zeroth order solution Y_0 is obtained after some algebraic transformation to be

$$Y_0 = \bar{\tau}/2\pi\left(1 - \frac{\cosh\sqrt{\frac{2\pi}{1-\epsilon}}X}{\cosh\frac{2\pi L}{a}\sqrt{\frac{\epsilon}{(1-\epsilon)}}}\right) \qquad ...(5)$$

where the higher order terms are neglected.

When $y = a/2$ the applied shear stress is equivalent to the Peierls stress assuming other stress fields to be negligible. This gives, after some algebraic manipulation, the Peierls stress as

$$\tau_p = \frac{(2\pi)^2 \alpha_1 \cosh\frac{2\pi L}{a}\sqrt{\frac{\epsilon}{1-\epsilon}}}{2ab\left(\cosh\frac{2\pi L}{a}\sqrt{\frac{\epsilon}{1-\epsilon}} - \cosh\sqrt{\frac{2\pi}{1-\epsilon}}a/2\right)} \qquad ...(6)$$

3 2 Comparison of Experimental Results with Theoretical Expressions

From Seeger,[11] the following expression is obtained. α_1, τ_p and Γ_c were given by previous workers:

$$\alpha_1 = ab\tau_p/2\pi \qquad ...(7)$$
$$(Seeger^{11})$$

$$\tau_p = \mu\pi\Gamma_0/ab \qquad ...(8)$$
$$(Dorn\ and\ Rajnak^6)$$

$$\Gamma_c^\circ = R\Gamma_0 \qquad ...(9)$$
$$(Dorn\ and\ Rajnak^6)$$

There is no loss of generality in using the experimental transition stress as τ_p, since the analysis of both Seeger[11] and Dorn and Rajnak[6] applies when this value is used, considering the immediate locality of the pinned line, i.e. the forces experienced by the line are for its purposes the stress τ_p in Eqs. (1), (2), (7) and (8).

The resulting parameters are then calculated for α_1 and Γ_0 and are the result of both the Peierls stress and the interaction with the solute atmosphere surrounding the dislocation line. As stated by Yokobori,[7] the transition stress consists of other interaction stresses and since the proportion of interstitials is far higher than the dislocation density (Table 1) the parameters calculated are primarily the result of this effect.

From Eqs. (7) and (8) the values are obtained as follows:

$$\alpha_1 = 2.7 \times 10^{-9} \text{ dyne}; \ \Gamma_0 = 5.4 \times 10^{-5} \text{ erg/cm}$$

Table 1—Stress, Velocity & Damping Coefficient Data

Velocity (cm/sec)	10	1	0·1	0·01
Applied shear stress (Mdyne/sq cm)	23	19·8	14	10
Damping coefficient (Mdyne-sec/cm²)	$6·1 \times 10^{-8}$	$5·27 \times 10^{-7}$	$3·73 \times 10^{-6}$	$2·66 \times 10^{-5}$
Density of dislocations (cm^{-2})	$6·95 \times 10^6$	$5·98 \times 10^7$	$4·23 \times 10^8$	$3·02 \times 10^9$

Comparing expressions of Seeger[11] and of Dorn and Rajnak,[6] the parameter α_1 is also given by $(\Gamma_c - \Gamma_0)/2$ and substitution of the values gives a new estimate for α_1 as $1·08 \times 10^{-9}$ dyne which compares favourably with the previous value. This indicates that the models of Seeger[11] and of Dorn and Rajnak[6] can be favourably compared.

Cottrell[12] who has done some of the pioneering work on yield points in zinc single crystals has measured the yield stress as 6·7 Mdyne/cm² in samples containing nitrogen. He states that this is absorbed from the atmosphere. Taking this as the original Peierls stress for dilute concentration of nitrogen in zinc, the present experimental results may be explained by the formula $2Gb/L$ to be due to an interparticle spacing of 10μ. This is by the use of the model of Orowan leading to this well known formula expressing the increase in stress limit to impurity concentration.

It may be remarked that in the preceding calculations, no estimate of the thermal fluctuations was made, and that the parametric analysis led to consistent results comparing two different approaches successfully. This is also mentioned by Dorn and Rajnak,[6] who state that the thermal effect on equilibrium dynamics is negligible and that the main parameter to be considered is τ/τ_p. Dorn and Guyot[13] also state that the shape of the lattice potential or Peierls hill is of little consequence and that the potential could be taken as sinusoidal, with no loss of generality. It is also clear that the line is not released from the constraining precipitate/interstitial constraints during the very short interval of the experiment, a few microseconds. Ashby[14] has given an expression for the 'waiting time' for release, and this, after some calculation, is found to be of the order 10^{12} exp (76) sec, which is also inversely proportional to the diffusion coefficient of Hirth and Lothe.[4]

Self-consistent results are thus obtained by use of a pinned line model to explain the experimental results. Other mechanisms might be responsible, although as yet unknown to the author. The work of Seeger[11] shows that the drag is of no consequence in the steady state solution of Eq. (1). This solution is measurable optically by the slip lines produced on etching, as shown in Fig. 2. Moreover, the drag is dependent on velocity, and cannot affect the solution in the steady state, for a time interval greater than 10μ sec. Drag can affect the cumulative term τ_b in Eq. (1) as a friction term. Ashby[14] has given an expression for drag of the form: $BV = \tau_b$ where $V = dy/dt$, which is a non-steady state term, being a function of time t.

4. Conclusions

1. The deformation behaviour of the zinc single crystals shows an increase in the flow or transition stress which is due to the presence of point obstacles. These are assumed to be clusters of nitrogen atoms, or molecules of Zn_3N_2.

2. The evaluation of certain non-dimensional parameters has indicated that the Seeger and Dorn theories can be favourably compared and have given good estimates of these parameters. The proportion of interstitial is too high to be neglected and these interactions are predominant. The analysis given is consistent to a factor of 10^{-9}. The dislocations remain pinned during the microsecond duration of the experiment, and are not released from the constraining pinning points.

Nomenclature

τ = Applied shear stress
τ_p = Peierls stress
G = Shear modulus
K = Hall-Petch and Ansell-Lenel constant
b = Magnitude of Burgers vector = 265 Å
C = concentration of solute
E_0 = mean energy per unit length of line
Γ_c = maximum line energy
Γ_0 = minimum line energy
Y = displacement coordinate of line
a, c = lattice parameter
$E(y)$ = line energy per unit length of line Fourier coefficient in $E(y)$
m = Mass per unit length of line constants
T = absolute temperature
e' = strain rate
ρ = dislocation density
B = drag coefficient
V = velocity of dislocation
ϵ = perturbation parameter = α_1/E_0
μ = 10^{-4}
R = $1 + 10^{-4}$

References

1. Ansell G H & Lenel P V, *Acta Met.*, **8** (1960), 612.
2. Peckner D, *The strengthening of metals*, (Reinhold Press, New York), 1964, 164.
3. Gurland J & Plateau J, *Trans. Am. Soc. Metals*, **56** (1963), 442.
4. Hirth J P & Lothe J, *Theory of dislocations*, (McGraw-Hill, New York), 1968, 616.
5. Ashby M F, *Phil. Mag.*, **14** (1966), 1157.
6. Dorn J, & Rajnak S, *TMS AIME*, **230** (1964), 1052.
7. Yokobori T, *An interdisciplinary approach to the fracture and strength of solids* (Wolters Noordhoff, Groningen, Holland), 1965, 79.
8. Hall E O, *Yield point phenomena in metals and alloys* (McMillan, London), 1970, 244.
9. Evers M, *Z. Metallkunde*, **50** (1959), 638.
10. Sommer A, *Peierls-Nabarro hardening in the presence of point obstacles* (N American Rockwell Corpn., and UCLA Engineering School, California, USA), 1970.
11. Seeger A, *Phil. Mag.*, **1** (1956), 651.
12. Cottrell A H, *Proc. phys. Soc.*, **B63** (1950), 339.
13. Dorn J & Guyot P, *Can. J. Phys.*, **45** (1967), 983.
14. Ashby M F, *J. appl. Phys.*, **42** (1971), 5273.

Electrical Properties of Sintered Selenium Powder Compacts

M M IBRAHIM

Physics Department, Faculty of Science, Assiut University, Souhag, Egypt

Two main types of conduction have been found for sintered selenium powder compacts; ohmic and space-charge limited for low and moderate applied fields, respectively. In addition, a low resistance state (switching on an abrupt increase in current) could be observed when the applied field reaches or exceeds a certain value which is minimum for compacts sintered at 160°C, and it decreases with increasing the annealing time. The conductivity-temperature relation obtained is characterized by extrinsic and intrinsic regions, as in a semiconductor. In addition, metallic conduction could also be observed at the higher temperature range, especially for compacts which were pre-sintered at higher temperatures. It is found that the activation energy for the compact which was pre-sintered at 160 C passes through a maximum in the instrinsic region, while it decreases continuously with increasing sintering temperature in the extrinsic region. X-ray diffraction studies show that selenium powder compacts suffer recrystallization with a degree that depends on both sintering temperature and annealing time.

1. Introduction

Studies on the electrical conductivity of selenium single crystals have been made in the condensed state, because of the use of this material in the design of semiconductor devices, photoconductive and photovoltaic applications. But attention on the amorphous and powder phases of selenium has been less dispite the fact that these phases are much more abundant in nature.

Sintering process is one of the easier and inexpensive methods for producing lumps of powdered materials in a bulky form without affecting their chemical properties, while their physical properties approach those of the single crystal phase. However, the process is often associated with the formation of new bonds, densification, grain growth, and may be crystallization. Besides, all these above mentioned properties are controllable so that a specimen of special character can be prepared.

It was found previously[1] that amorphous selenium suffers grain growth during thermal treatments with a rate that increases with temperature with the maximum occurring somewhat below the melting point. Also the nucleation rate depends on temperature and purity. The maximum occurs at about 110°C or 120°C. Many materials, mostly non-metals added to the melt accelerate nucleation, while a few inhibit crystallization; notably phosphorus. Moreover, two types of polycrystalline structures in selenium could be distinguished, namely the colony and equiaxed metallic structures. On crystallization, the crystallites grow in radial clusters from the nucleation centres until the entire mass is crystallized.

At a temperature above 150°C, there is recrystallization of the equiaxed structure. The region of contact of different radial colonies undergoes transition to a very fine equiaxed structure in the first stage. After this, recrystallization proceeds towards the nuclei of the colonies. On further heating, the grains grow with time.

The crystallization temperature influences the conductivity of selenium. Plessner[2] pointed out that when the first crystallization of amorphous selenium is carried out at 175°C instead of at 110°C, the conductivity was reduced by a factor of 10. These results were attributed to reduction in both mobility and current carrier concentration. In addition, it was found that crystallization temperature affects the amount of porosity, since the density was found to be equal to 4.16 and 4.43 g/cm² for selenium at the two above mentioned temperatures of crystallization. Also, at higher crystallization temperatures, the crystal was larger in size. The crystal size for samples crystallized at 175°C was three times larger than those crystallized at 110°C. Besides, the smaller the size of the crystallites, the greater was the number of the charge carriers, so that the single crystal which has the maximum size contains the minimum number of charge carriers. The rate of decrease of the number of charge carriers with increasing temperature is greater for samples crystallized at lower temperatures. Besides, the mobility of the samples crystallized at higher temperature is lower.

The current voltage characteristics of amorphous selenium as investigated by Lanyon and Spear[3,4] con-

—

sist of three regions which are: (i) the ohmic region, (ii) space-charge limited region and (iii) the region where there is an abrupt rise in current with any further increase in potential. They attributed their results to the excess carrier density and the injection of these carriers into insulator and the position of the Fermi level with respect to the valence band and the level of trapping, which is quite in agreement with the basis of Rose and Lampert's[5,6] theory when an idealized ohmic contact was considered.

The space-charge limited current in the case of selenium monocrystal was studied by Stuke[7] on the assumption that the single crystal is non-homogeneous but consists of a large number of thin zones with considerable higher resistivity and homogeneously distributed in the crystal. These zones are of the same thickness (d) and with concentration (n) per unit length. In addition, the traps are homogeneously distributed in the high resistive zones (H-traps per unit volume) and all have the same dissociation energy. On these conditions, Stuke found the following expression for the space-charge limited current density when the applied voltage over the crystal of length L is V.

$$i = \frac{9}{8} k \, \epsilon_0 \, \mu \, \frac{K}{K+H} \frac{1}{n^2 \, d^3} \frac{V^2}{L^2}$$

where k is the dielectric constant, K the mass-action constant for the dissociation reaction of traps, ϵ_0 the permittivity of empty space and μ the mobility.

The V^2 and $1/L^2$ dependence of the space charge limited current was obtained experimentally also by Stuke and Wondt[8] and Graeffe and Heleskivi.[9]

In addition Henisch[10] pointed out that the log σ-1000/T relation of the microcrystalline selenium is not linear, except in the case of fully crystallized samples. Moreover, the conductivity-temperature dependence of microcrystalline selenium according to the Meilkhov[11] model is formulated as follows

$$\sigma = \frac{e \, \mu_a \, P_a}{x} \exp(-\Delta E/kT)$$

where μ_a, P_a and x are all related to the amorphous thin layer between the crystallites.

These previous studies thus indicate the need for a deeper understanding of the physical properties of selenium. Further, because of the importance of selenium in every day life applications, it was decided to study the effect of sintering and annealing processes on the current-voltage characteristics, electric conductivity, activation energy and switching properties of selenium powder compacts. In addition, X-ray investigations were carried out to interpret beyond doubt the results obtained.

2. Experimental Procedure

Selenium samples in tablet form were prepared using cold pressing technique. Green compacts with near X-ray density of selenium could be prepared even if the working pressure did not exceed 100 kg/cm^2, which shows that the compactibility of selenium is high. For homogeneity, the thickness to cross-sectional area ratio of a certain compact must be limited. This could be performed by prelimitation of the forming pressure and the initial weight of the powder. The homogeneity of the compacts could be examined microscopically in addition to some preliminary tests which show that the bulk density and resistivity (when the applied voltage is extremely low to avoid field effect) of a certain green compact are thickness independent.

One of the requirements of conductivity measurements is that the compact surfaces be optically flat. For green compacts, this requirement could be verified easily since the opposed surfaces of the upper and the lower rams of the used die were optically flat. Heat treatments may be associated with surface contaminations even if heating is carried out under moderate vacuum. To get rid of the contaminant films, polishing and then washing processes were carried out. Polishing was carried out electrolytically while washing was carried out using condenser extractor technique with acetone as solvent.

The problems of contact and contact electrodes and the solubility of electrode atoms in selenium, especially at elevated temperatures, may contribute to impurity. The electrodes were made from pure graphite since it proved to be the only one inert to selenium attack among the three most inactive elements; gold, platinum and graphite.

X-ray examination was carried out for different specimens in powder form with average particle size about 94 μm using Seivert type X-ray diffractometer. The bulk specimens received different heat treatments and were ground using agate mortar. A CuK_a monochromatic source of X-ray with wavelength 1·542 Å was used.

3. Results and Discussion

The current-voltage characteristics of selenium powder compacts is nonlinear, as shown in Fig. 1 for a compact with green density 3·83 g/cm^3, average particle size 94 μm and sintered at 128°C for 210 min. When the compact was annealed for different periods of time at 100°C, the characteristics remained nonlinear except that they get shifted towards the current axis with an increase in the annealing time as shown in Fig. 1. To avoid any additional sintering taking place, the annealing temperature was

selected to be 100°C which is relatively lower than the onset temperature of sintering, which always lies at half the melting point of selenium.

The current-voltage characteristics shown in Fig. 2 belong to different selenium powder compacts with the same green density 3·83 g/cm³, average particle size 94 μm, and thickness = 3·15 ± 0·04 mm and formed under the same conditions but sintered at different temperatures. Fig. 2 reveals that the general feature of the I-V characteristics are independent of the sintering temperature.

The deduced double logarithmic relation of any of the current-voltage characteristics indicates the curve to be a kinked linear one. The characteristic relation consists of two main logarithmic terms and a third one where the current suffers a continuous increase with time when the voltage reaches or exceeds a certain value. The first region corresponds generally to low applied voltages. The variation is always linear with an average slope equal to 1·3. This shows that the conduction within this region is mainly ohmic. The slight deviation of the value for the slope from unity may be caused by a negligible injection of excess carriers from the electrode material into the specimen.

The second region of the relation is characterized by the field effect, since the value of the exponent of the logarithmic relation is always higher than unity. The exponent has a value around 2 which increases slightly for samples with increased values of the annealing time. This generally corresponds to moderate values of the applied voltage. It can be considered that the injection carrier density from the electrode material through the specimen becomes
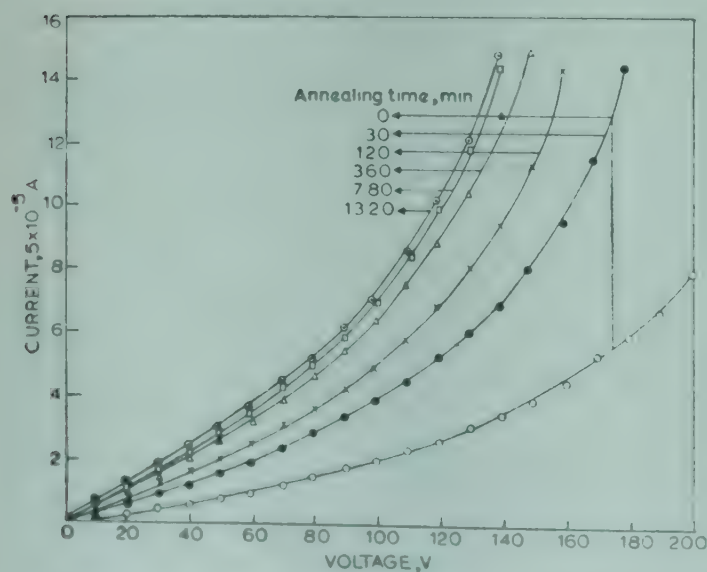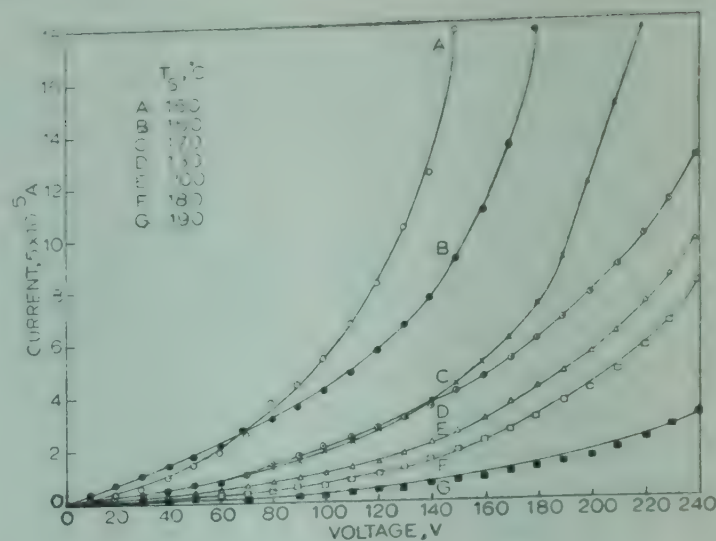
Fig. 2—Effect of sintering temperature (T_s) on the I-V characteristics of selenium powder compacts

comparable to the initially present thermal equilibrium density of the carriers through the sample itself. The current within this region is space-charge limited and remains steady for a given voltage until a certain voltage is reached. The excess carrier density increases in proportion to the applied voltage within this region and the steady state Fermi level moves towards the valence band. However, when the applied voltage exceeds a value, called the trap-filled limit, the traps get completely filled and any further increase in voltage should lead to a sharp rise in current. These results are quite in agreement with the basis of Rose and Lampor's[5,6] theory which was verified also by Lanyon and Spear.[4]

The value 2 for the exponent of the logarithmic relation between current and voltage shows that in the second region of the characteristics, the space-charge is the major factor controlling the conduction. This deduction is in agreement with the theoretical approach found by Stuke[7] and the experimental results reported by him and others.[8,9]

The two main experimental observations indicating that the nonlinearity of the characteristics is due to space-charge limited current are:

(1) The appearance of slow current transients when a change is made in the voltage over the specimen. The transients are caused by interaction of the space-charge limited current with the traps in the selenium samples.

(2) The hysteresis observed in the current-voltage relations. This is due to the characteristics during increasing and decreasing the voltage across the specimen not coinciding.

In addition, the value 2 for the slope of log I-log V relation indicates a complete space-charge limited current. The discrepancy from the value of 2 indicates that the space-charge is not completed.

Fig. 1—Effect of annealing time on the I-V characteristics of selenium powder compacts

The abrupt and continuous increase of current when the applied voltage reaches or exceeds a certain value, illustrates that selenium powder compacts exhibit electrical switching, since this process is a reversible one. This switching-on voltage was found to decrease with an increase in the annealing time while it depends irregularly on sintering temperature as shown in Table 1.

Two main mechanisms which may contribute to the switching phenomenon are:

(a) The existence of low resistance-channelized paths which is represented by the crystalline phase formed due to sintering and/or annealing, and (b) thermal Joule heating effect. Since the compacts have the same green state distribution functions for the grains and same properties, if the thermal Joule heat-

ing is the main responsible mechanism for the switching, the switching-on voltage for all compacts should be the same. But it is not the case. Therefore, one can conclude that crystallization plays the dominant role in switching phenomenon and the effect is maximum at those temperatures where the switching-on voltage is minimum. X-ray investigations justify this conclusion. Also this conclusion is quite in agreement with that of Henkel[1] who has pointed out that above 150°C, the transition to the equiaxed microcrystalline phase takes place. Moreover, the pronounced continuous decrease in the switching-on voltage with an increase in the annealing time, can be explained on the basis that the activation energy decreases with an increase in the annealing time. Also, the amorphous selenium suffers continuous structural change with annealing time so that, as soon as crystallization begins at a certain crystallization temperature, it continues to occur with time even if annealing is carried out after the process at relatively a lower temperature. The X-ray diffraction patterns compared in Fig. 3 justify this deduction. Further, it is observed that compacts sintered at the higher temperatures of 190 and 200°C do not suffer switching even if the annealing time is 22 hr and the applied field equal to 760 V/cm.

The effect of annealing time becomes more pronounced when the current versus annealing time relation under a certain fixed field is considered. When the annealing temperature is equal to 100°C, as shown in Fig. 4, the logarithmic relation consists of two main regions with different slopes equal to 0·2 and 0·13 for the lower and higher regions respectively. During these measurements, precaution

Table 1—Dependence of the Switching-on Voltage on Sintering Temperature (T_s) and Annealing Time (t_a) (The annealing temperature = 100 °C)

T_s, °C :	128	150	160	170	180
t_a (min)					
0	—	180	160	220	—
10	—	160	150	210	—
30	220	160	150	220	—
60	—	160	140	200	—
120	200	140	130	180	—
240	200	130	130	180	230
480	—	130	125	170	230
780	190	130	120	170	215
1320	180	130	120	170	210
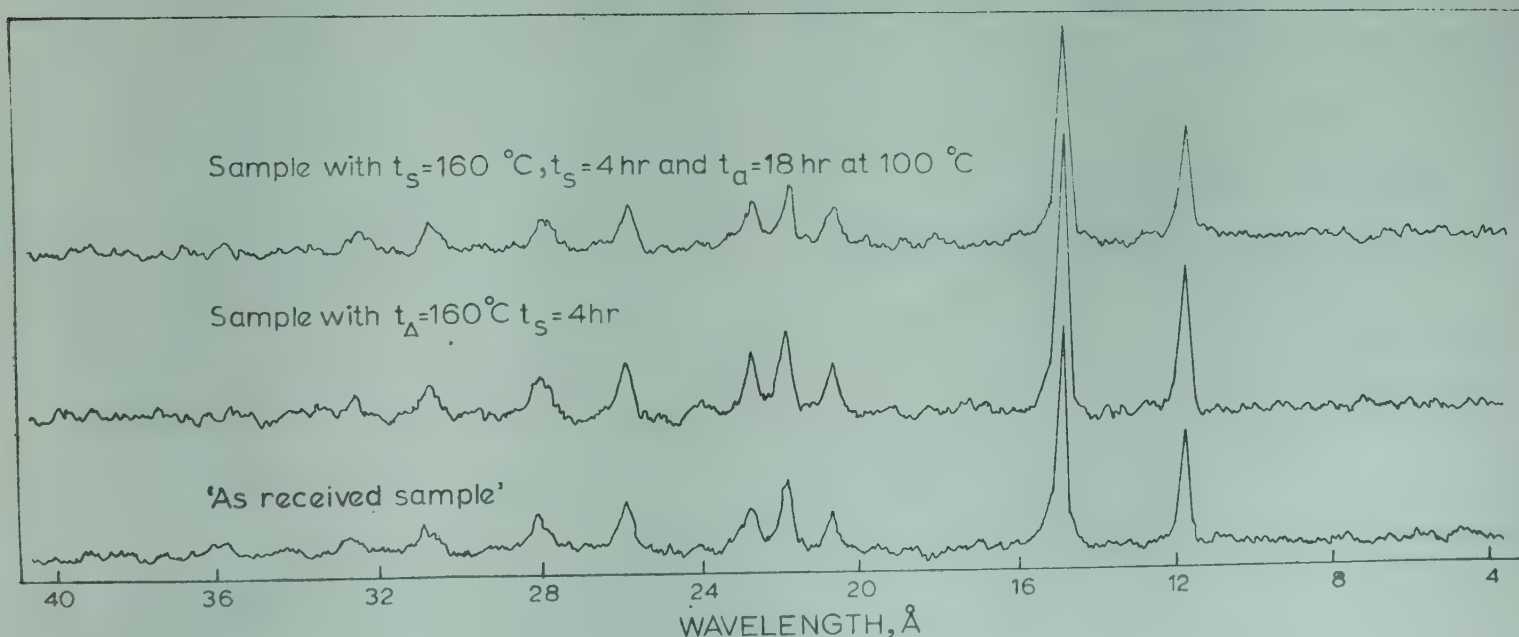
Fig. 3—X-ray diffraction patterns for powder specimens of Se
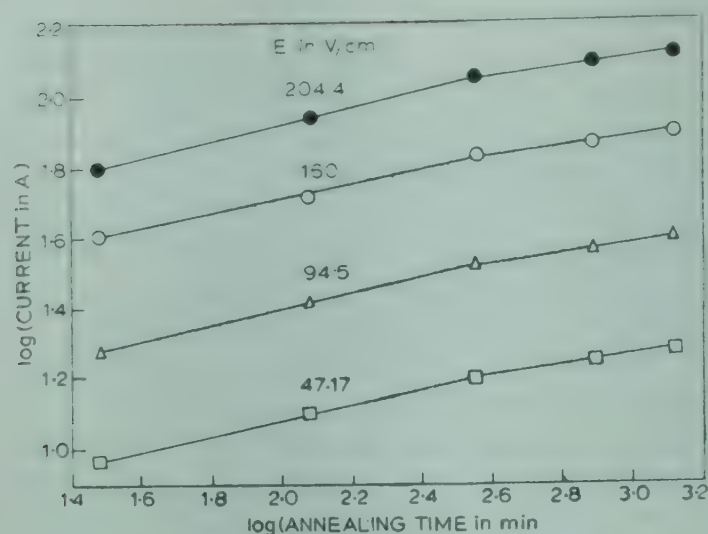
Fig. 4—Plot of log I versus log annealing time

was taken to restrict the applied voltage to a value lower than the switching-on voltage. Both the ohmic and space-charge-limited regions were considered. With higher values of the applied field, the current always shows higher values but the rate of variation of current with annealing time is not affected by change in the fixed applied field. From these results, one can assert that the annealing process is associated with continuous structural changes in the compact constituents. This fact is clear by comparing the X-ray spectra shown in Fig. 3. It is also evident that annealing does not affect the concentration or the mobility of the charge carriers at a low annealing temperature (100°C).

The variations of conductivity (σ) with sintering temperature (T_s) are presented in Figs. 5 and 6 for different values of annealing time and applied field. The conductivity is observed to pass through a maximum at a certain sintering temperature (160°C) and the value corresponding to this maximum increases with increase in both the applied field and the annealing time. The observed increase in the conductivity with an increase in both the applied field and the annealing time is due to the increase in the mobility of the charge carriers, and the continuous structural changes mentioned above respectively. Since the original specimen constituents are with a certain structural phase, the sintering process may initiate a new ordering in the compact which is sintering temperature dependent.

X-ray diffraction studies of the 'as-received' powder and the crushed powder of those eight compacts which are presintered at different temperatures reveal that the former is not completely amorphous and that the selenium used is of n-type. Besides, the amount of crystallization that takes place depends on the sintering temperature. In

addition, the amount of recrystallization is maximum when sintering temperature is 160°C. It is revealing that it is at this temperature, peaks are observed in the conductivity versus sintering temperature curves and that minimum values of the switching-on voltage are obtained.

The semiconducting behaviour of selenium powder compacts is as shown in Fig. 7. Through
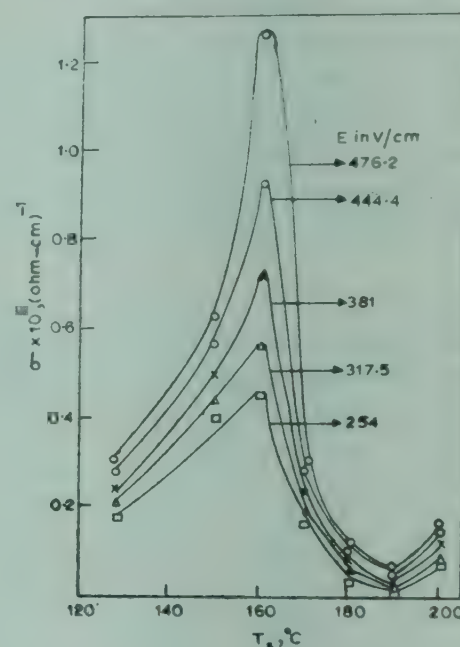
Fig. 5—Variation of conductivity (σ) with sintering temperature (T_s)
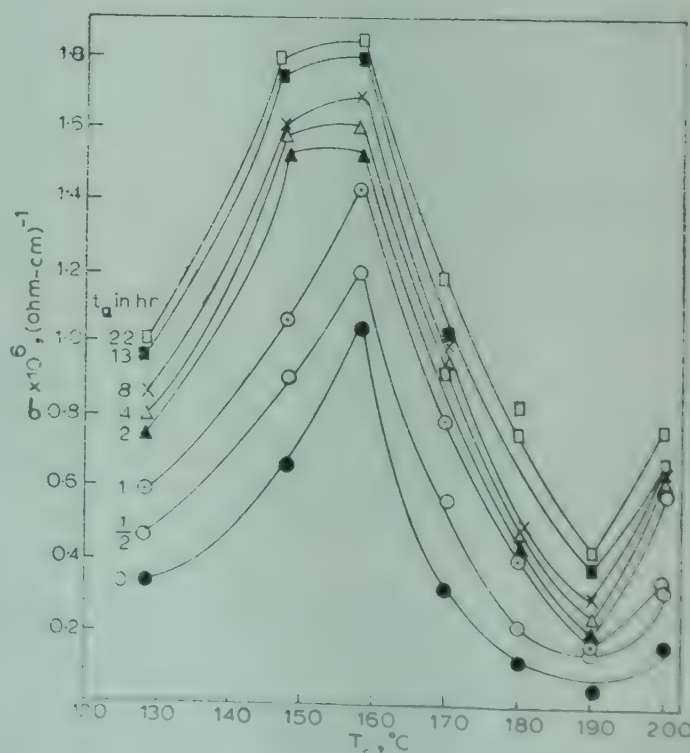
Fig. 6—Variation of conductivity of selenium powder compacts with sintering temperature (T_s) [sintering time = 210 min. Annealing was carried out at 100°C for different periods of time (t_a) as marked on the curves]
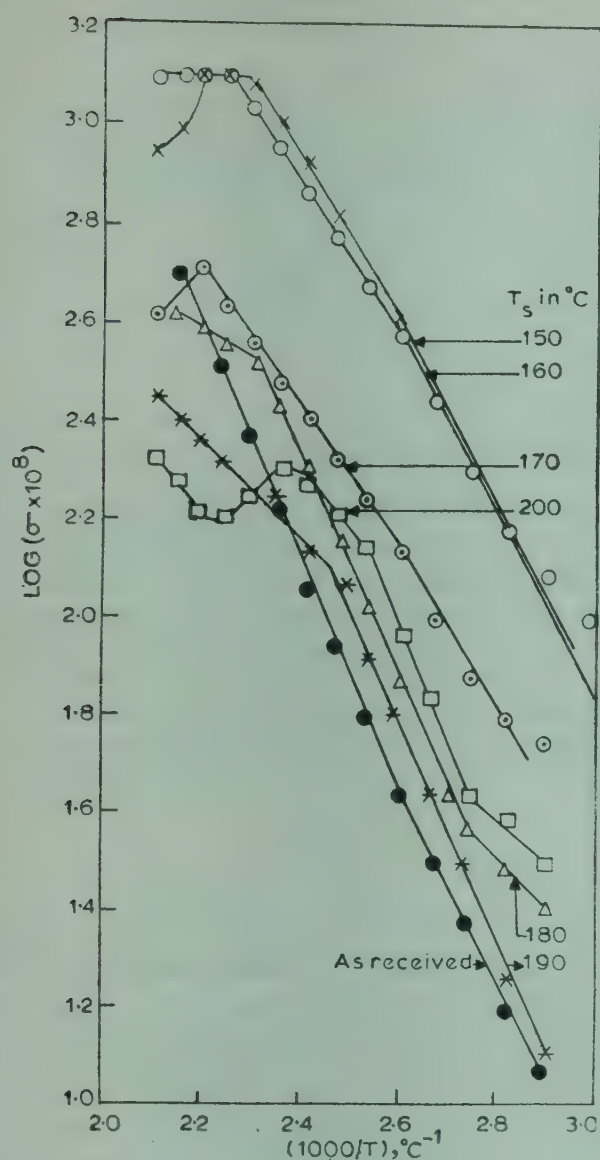
Fig. 7 — Variation of conductivity with the reciprocal of absolute temperature (T)

Table 2—Effect of Sintering Temperature (T_s) on ΔE_1 and ΔE_2, the Activation Energies of the Extrinsic and Intrinsic Regions respectively

T_s :	148	158	170	180	190	200	'as-received'
ΔE_1	0·7527	0·6825	0·6045	0·421	0·881	0·351	0 741
ΔE_2	0·585	1·287	0·9555	0·819	0·429	0·897	0·936

vation energy vary much more with sintering temperature as shown in Table 2.

Results reported in Table 2 indicate that within the extrinsic region, the activation energy suffers a continuous decrease with increasing sintering temperature, while within the intrinsic region, it passes through maximum when the sintering temperature is 160°C. In both regions of conduction, the 'as-received' compact exhibits higher values of the activation energy. This shows that sintering process narrows the gap width of conduction.

For most of the compacts, the transition temperature between the extrinsic and intrinsic regions lies at 110°C. For those presintered at 190 and 200°C, it lies at 140 and 120°C respectively in addition to a lower transition at 90°C. The transition temperature of 110°C agrees with the temperature where maximum crystallization of selenium is reported to take place.[2]

most of the temperature ranges, the temperature co-efficient of conductivity is positive. In addition, most of the selenium powder compacts which were presintered at different temperatures and then annealed at 100°C for 22 hr exhibit metal-like conduction at higher ranges of temperatures, while the 'as-received' does not show such a metal-like behaviour. The effect of sintering temperature on the conduction is pronounced because both the temperature coefficient of conductivity and the acti-

References

1. Henkels H W, J. appl. Phys., 22 (1951), 916.
2. Plessner K W, Proc. phys. Soc. Lond., B64 (1951), 671.
3. Lanyon H P D, Recent advances in selenium Physics, (ESTC), 1965.
4. Spear W E, Proc. phys. Soc. Lond., B70 (1961), 669.
5. Rose A, Phys. Rev., 97 (1955), 538.
6. Lampert M A, Phys. Rev., 103 (1956), 1648.
7. Stuke J, Recent advances in selenium Physics (ESTC), 1965.
8. Stuke J & Wendt K, Phys. Status. Solidi, 8 (1964), 533.
9. Graeffe R & Heleskivi J, Acta Polytech. scand., (1966).
10. Henisch H, Rectifying semi-conductor contacts, (Clarendon press, Oxford), 1957.
11. Meilkhov E Z, Soviet Phys. Solid St., 7 (1965).

A New Approximation under the Perturbation Theory for Microwave Line-width Calculation & the Quadrupole Moment of Benzene[*]

G K Johri & R P Rishishwar

Physics Department, D A V College, Kanpur 208 001

A new approximation under the second order perturbation theory for line-width calculations at microwave frequencies has been proposed and the elastic and inelastic collisions have been included. This approximation gives the Lorentzian line shape and explains the observed width within the experimental bars. In OCS-Ar collisions, first- and second-order induction and dispersion interactions have been considered in the calculations. Only long-range collisions are the main contributors to the line-width and almost similar results are obtained whether the repulsive forces are included or neglected. The quadrupole moment of benzene has been evaluated from OCS-C_6H_6 and $CH_3{}^{81}Br$-C_6H_6 collisions. Dipole-quadrupole, quadrupole-quadrupole and dispersion interactions have been considered in the calculations. The average value of the quadrupole moment from OCS-C_6H_6 and $CH_3{}^{81}Br$-C_6H_6 collisions using mean collision velocity is 8.07 ± 3.15 D Å and using Maxwellian distribution of velocities is 7.40 ± 3.03 D Å

1. Introduction

The study of molecular collisions and microwave line-width gives valuable information about the nature of the intermolecular forces, molecular behaviour in collision and the transfer of the rotational energy between gas molecules. However, the perturbative theories used for line-width calculations[1-6] are based on the following assumptions: (i) Duration of collision is negligible in comparison to the time between the collisions (i.e. impact approximation), (ii) Bimolecular collision approximation in which the effects of collision involving more than two molecules are negligible, (iii) The classical path approximation without any interaction potentials is adequate and (iv) The perturbation expansions for calculations are sufficient. Comprehensive reviews[7-10] on the rotational energy transfer are available in literature.

Recently, Johri[11] made a comparative study of different perturbative approaches. This study revealed that the collision function formulated by Johri and Srivastava under Anderson's theory, collision function under Murphy and Boggs[5] (MB) theory and that under Mehrotra and Boggs[6] (MEB) theory seem to have the correct form as they smoothly couple the regions of weak and strong collisions. In the collision interruption function (CIF) used by Johri and Srivastava,[4] the contribution of elastic collisions comes also from $J'_i = J_i$, $J'_f = J_f$ transitions

and interference term called $S_2(b)_{mid}$. Johri and Srivastava[4] obtained line-width parameters comparable with the MB theory. Recently, Mehrotra and Boggs[6] considered the effect of phase shift and have formulated CIF for the line-width and line shift calculations which recovers the CIF used by Johri and Srivastava[4] under the approximation of the MB theory.[5] Hence it can be concluded that they have shown the importance of considering the effect of phase shift in the line shift calculations and treated the CIF as complex for the first time in this field.

For strong dipole-dipole interactions, the discrepancies sometimes become too large to be accounted by any known theory. Srivastava and Kumar[12] have shown that the discrepancy of higher widths in strong dipole-dipole interaction depends on the product of the square of the dipole moments and the reduced mass of the molecules involved in the interactions. Even accounting for large errors in measurements, one can safely conclude that the discrepancies in the experimental and theoretical results still remain and may be due to the strong and intermediate collisions which cannot be treated by perturbative theory. Perhaps a non-perturbative approach[13,14] is unavoidable for resolving these discrepancies. However, very large computer time forbids the attempt to use any of the non-perturbative techniques. Recently Johri and Mehrotra[15] have used a new interpolation scheme under the perturbative approach suggested by Mehrotra and Boggs[16] for strong collisions. The observed line shift[17] showed that even for

rotational transitions at microwave frequencies, the effect of phase shift is important.

In this paper, a new approximation including elastic and inelastic collisions using the second order perturbation theory has been proposed. The calculations have been done for OCS-Ar, OCS-C_6H_6 and $CH_3^{81}Br$-C_6H_6 collisions and the quadrupole moment of benzene has been evaluated using mean collision velocity and Maxwellian distribution of velocities.

2. Theory

Anderson's theory[1] assumes that each collision is associated with both phase and amplitude changes in the oscillations and thereby both the adiabatic and non-adiabatic effects have been taken into account in the theory. The expression for the average energy absorbed in a dipolar transition $J_i \rightarrow J_f$ is

$$W_{J_i J_f} = 2\gamma \frac{\rho_{J_i J_f}}{(2J_i + 1)} \sum_{m_i, m_f} | J_i m_i | \mu_z | J_f m_f |^2$$

$$\times \frac{nv \sigma_r}{(\omega - \omega_{fi} + nv \sigma_i)^2 + (nv\sigma_r)^2} \quad ...(1)$$

in which

$$\gamma = \frac{2\pi \omega}{\hbar C} \quad ...(2)$$

and

$$\rho_{JJ} = \frac{(2J + 1) \exp(-E_J/kT)}{\sum_n (2J_n + 1) \exp\left[-\frac{E_n}{kT}\right]} \quad ..(3)$$

is the population density of the Jth state, k is the Boltzmann's constant and T the absolute temperature. The line shape is Lorentzian with half-width at half power given by

$$\Delta\nu = \frac{nv}{2\pi} \cdot \sigma_r \text{ (Hz)} \quad ...(4)$$

and line shift[17]

$$\Delta\nu_s = -\frac{nv}{2\pi} \sigma_i \quad ...(5)$$

σ_r and σ_i are the real and imaginary parts of the collision cross-section

$$\sigma = \sigma_r + i\sigma_i = \int_0^\infty 2\pi b \, db \, [P_i(b) + P_f(b)] \quad ..(6)$$

and n is the number of colliding molecules per unit volume. If the Maxwellian distribution of velocities is considered and the collisions are averaged over all the directions, the line-width parameter of a microwave transition from initial state i to final state f is given as

$$\Delta\nu = N \sum_{J_2} \rho_{J_2} \int_0^\infty b \, db \int_0^\infty dv \, v \, F(v)$$

$$\times \left[P_i(b, v) + P_f(b, v) \right] \quad ...(7)$$

where b is the impact parameter, v is the relative velocity, $F(v)$ the Maxwell-Boltzmann distribution function, ρ_{J_2} is fraction of the colliding molecules in state J_2, N is the total number of the colliding molecules, and P_a $(a = i, f)$ is the transition probability of leaving the initial state a. Under Anderson's theory,[1,2] transition probability is as follows

$$P_a^A(b, v) = 1/2 \sum_{m_a, m_2} \frac{\langle J_a m_a J_2 m_2 | p^2 | J_a m_a J_2 m_2 \rangle}{(2J_a + 1)(2J_2 + 1)} \quad ..(8)$$

The cross term vanishes for the interaction involving dipole moment of the absorber. $J_2 m_2$ are quantum numbers of the various states of the perturber. $< i | p | f >$ is the matrix element of the unperturbed Hamiltonian between the eigen states i and f of the absorber perturber system.

The values of $P(b, v)$ at large impact parameters can be calculated with reasonable accuracy by perturbative approaches. In the literature many approximations have been used to calculate $P(b, v)$. Anderson[1] suggested three approximations to compute $P(b, v)$ at small impact parameters.

$$P^{(1)}(b, v) = 1 - \cos\left[P_i^A + P_f^A \right]^{1/2} \quad ...(9)$$

$$P^{(2)}(b, v) = 1 \quad\quad\quad b \leqslant b_0$$

$$P^{(2)}(b, v) = 1/2 \left(P_i^A + P_f^A \right), \quad b > b_0 \quad ...(10)$$

$$P^{(3)}(b, v) = 1 - \exp\left[-P_i^A - P_f^A \right] \quad ..(11)$$

where P_a^A $(a = i, f)$ are the values calculated from the second order perturbation theory. In $P^{(k)}(b, v)$, k represents the kth approximation and in P_a^A, A indicates Anderson's theory.

Johri and Srivastava[4] formulated the following collision function under Anderson's theory:[1]

$$P^{(4)}(b, v) = 1 - \exp\left[-P_i^A/2 - P_f^A/2 \right] \quad ...(12)$$

where $P_a^A(b, v)$ is given by Eq. (8). Murphy and Boggs[5] assume that the effect of the phase shift on line-width is negligible and ignore the probability of each molecule making the transition back to the

249

original level once it left. The collision function under the MB theory is

$$P^{(5)}(b, v) = 1/2 \left[1 - \exp\left(- P_i^{MB} \right) \right.$$

$$\left. + 1 - \exp\left(- P_f^{MB} \right) \right] \quad ...(13)$$

where P_a^{MB} represents transition probability in MB theory. MEB theory[6] formulated the following CIF

$$P^{(6)}(b, v) = 1 - \exp\left[- P_i^{MEB}/2 - P_f^{MEB}/2 \right]$$

$$\times \cos\left(S_{if}^{MEB} \right) \quad ...(14)$$

where

$$S_{if}^{MEB} = 1/\hbar \int_{-\infty}^{\infty} (V_i - V_f)\, dt - (\phi_i - \phi_f)$$

$$...(15)$$

is due to elastic collisions. The term $\frac{1}{\hbar} \int_{-\infty}^{\infty} (V_i - V_f)dt$ is zero for microwave transitions, but has significant contribution for infrared transitions.

Johri and Mehrotra[15] have applied, for the first time, the following approximation as suggested by Mehrotra and Boggs.[16] Let $P^{(2)}(b, v)$ be the transition probability of finding the system in a state using second-order perturbation theory. Then,

$$P^{(2)}(b, v) = N_0 + x \quad ...(16)$$

where N_0 is an integer and $0 \leqslant x < 1$, $P(b, v)$ can be approximated[16] as

$$P^{(7)}(b,v) = 1 - x \qquad \text{if } N_0 \text{ is odd} \quad ..(17)$$
$$P^{(7)}(b,v) = x \qquad \text{if } N_0 \text{ is even} \quad ..(18)$$

In the present treatment of the pressure broadening, we assume that in the molecular collision, both the amplitude due to inelastic collisions and the phase shift due to elastic collisions are changed and the line-width parameter is the sum of the line-width contributions of the individual levels. The Lorentzian line shape occurs when the mechanism affects the energy levels[5,18] between which the transition takes place, whereas the Gaussian line shape occurs when the mechanism affects the emitted or the absorbed photon. In the collision broadening phenomenon, spectral lines are Lorentzian in shape[19] except for a small correction of Gaussian shape due to Doppler effect. This correction is normally carried in obtaining the experimental line width parameters due to pressure broadening.

Using the perturbation theory if we are studying the $J_i \rightarrow J_f$ line in the ground vibrational state, the

radiation is completely interrupted when molecule leaves either J_i or J_f state. This perturbation theory is different from the Anderson's theory in respect of the following boundary condition:

For $P_a^A(b,v) < 1$ use $P_a^A(b, v) = 1$ ...(19)

$P_a^A(b, v)$ physically represents the transition probability that the molecule leaves the state i or f and it cannot be > 1. In Anderson's approximation No. 2, the transition probability function, $\left(P_i^A + P_f^A \right)$ is equated to unity for getting b_0 but here $P_i(b, v)$ and $P_f(b,v)$ should be solved separately for the values of $b_{0,i}$ and $b_{0,f}$ respectively. From $b_{0,i}$ and $b_{0,f}$ one can then obtain the $\sigma_{J_i J_2}$ and $\sigma_{J_f J_2}$ by the usual method.[20] The collision cross-section for small impact parameter can then be approximated as

$$\sigma_{J_2}^{(8)} = 1/2 \left(\sigma_{J_i J_2} + \sigma_{J_f J_2} \right) \quad ...(20)$$

and the half-width at the half power, $\Delta\nu$ is, therefore, calculated from the following equation:

$$\Delta\nu = \frac{n\nu}{2\pi} \left[\sum_{J_2=0}^{J_{2max}} \rho_{J_2} \sigma_{J_2} \right.$$

$$\left. + \left(1 - \sum_{J_2=0}^{J_{2max}} \rho_{J_2} \right)\left(\sigma_{J_2} \right)_{const} \right] \quad ..(21)$$

3. Results and Discussion

3.1 OCS-Ar Collisions

The molecular parameters used in the present calculations are given in Table 1. The line-width parameter has been calculated using mean collision velocity and Maxwellian distribution of velocities and has been compared with the measured value. The calculations have been done considering the first order (dipole induced and dipole) and second order (quadrupole-dipole induced dipole + dipole-quadrupole induced dipole) induction interactions, dispersion interactions and the exchange forces. The results are given in Table 2. In the OCS-Ar collisions,[21] long-range collisions are the main contributors to the line-width and almost similar results are obtained whether the repulsive forces are included or neglected. The use of the Maxwellian distribution of velocities instead of the mean collision velocity, increases the line-width by about 7%. The present approximation is quite good for the treatment of OCS-Ar collisions.

3.2 OCS-C₆H₆ Collisions

In OCS-C_6H_6 collision, the line-width parameter has been calculated by the new boundary condition

in the second order perturbation theory. The calculated values are given in Table 3. The molecular parameters used are given in Table 1. In this collision, the quadrupolar forces seem to be quite important[22] since the calculated width is lower than the measured value, when only dispersion and induction forces are considered. The interactions considered in these collisions are the dipole-quadrupole, quadrupole-quadrupole and dispersion forces. Using $\Theta_{C_6H_6} = 11.2$ DÅ the line-width parameter of $J=1\rightarrow2$ of OCS in OCS-C_6H_6 collision is 6.60 ± 0.33 MHz/torr for mean collision velocity and 6.83 ± 0.33 MHz/torr for Maxwellian distribution of velocities. The former value is closer to the experimental line-width parameter, viz. 5.14 ± 0.13 MHz/torr, reported by Krishnaji et al.[23] The calculated widths are more

by about 28% when mean collision velocity is used and by about 33% when Maxwellian distribution of velocities is used. The contribution of the dipole-quadrupole interactions is about 90% at $J_2 < 15$ and

Table 1—Values of the Molecular Parameters[a] in Line-width Calculations ($T=300$ K, $p=1$ torr)

	OCS-Ar	OCS-C_6H_6	$CH_3{}^{81}Br$-C_6H_6
M	23.99	33.96	42.8111
$v(10^4$ cm/sec)	5.1451	4.3247	3.8517
$\mu_1(D)^b$	0.7152	0.7152	1.8100
$\theta_1(D\text{Å})^c$	2.0	2.0	
$\alpha_1(\text{Å}^3)^d$	5.57	5.57	—
$\alpha_1^* - \alpha_1'$ (Å$^3)^d$	4.70	4.70	2.00
$\alpha_2(\text{Å}^3)^c$	1.64	10.32	10.32
$\dfrac{\epsilon_1\epsilon_2}{\epsilon_1+\epsilon_2}$ (10^{-12} ergs)^e	10.8763	8.5333	7.8120
$A^{10}_{\mu_1 \alpha_2\mu_1}$ (10^{-74})	0.0037	—	—
A^{10}_{dis2} (10^{-74})	4.8332	166.7446	31.8996
$A^{12}_{\mu_1 \theta_1\alpha_2}$ (10^{-89})	0.8461	—	—
$A^{6}_{\mu_1\theta_2}$ (10^{-42})	—	2.1864*	2.2145**
$A^{8}_{\theta_1\theta_2}$ (10^{-60})	—	76.9386†	30.4185‡
$k/b \, \Delta E(\text{Å}^{-1}$ K GHz^{-1})	0.0363	1.4529	1.6313
$nv/2$ (10^{20})	8.3007	6.9772	6.2142
$a(\text{Å})$	0.37	—	—
$d(\text{Å})$	3.56	—	—

*$\Theta_{C_6 H_6} = 10$ D Å   †$\Theta_{C_6 H_6} = 10$ D Å; $\Theta_{OCS} = 2$ D Å

**$\Theta_{C_6 H_6} = 11.2$ D Å   ‡$\Theta_{C_6 H_6} = 11.2$ D Å;

$$\Theta_{CH_3{}^{81}Br} = 1 \text{ D Å}$$

a Pandey P C, Kirty K K, Srivastava S L, *J. Phys.*, **B4** (1971), 786.

b Muenter J S, *J. chem. Phys.*, 48 (1968), 4544.

c Krishnaji & Srivastava S L, *J. chem. Phys.*, 47 (1967), 1885.

d Hirschfelder J C, Curtiss C F & Bird R B, *Molecular theory of gases and liquids* (John Wiley, New York), 1954.

e Kaiser D W, Tables of the Ionization Potentials Kansas State University *Handbook of Physics and Chemistry*, edited by C D Hodgman *et al.* (Chemical Rubber Publishing Co., Cleveland, Ohio), 1959, 41st Edn, p.2549.

Table 2—Line-width Parameters ($\Delta\nu/p$) of OCS $J=1\rightarrow2$ Broadened by Ar and Obtained by Various Methods (Values of $\Delta\nu/p$ in MHz/torr)

Source	$a_2=0.00$ $b_2=0.28$	$a_2=0.28$ $b_2=0.28$
Theoretical study		
Present study	2.39*	
	2.55†	
Johri and Srivastava[a]	2.30*	
	2.63†	
Murphy and Boggs[b]	2.12*	
Krishnaji and Srivastava[c]	2.48*	
Mehrotra and Boggs[d]	3.27	3.17
Fits and Marcus[e]	3.87	3.32
Mehrotra et al.[21]	3.39	3.32
Cady[f]	3.91, 4.01	3.54, 3.43
Experimental study		
Krishnaji and Srivastava[c]	2.40 ± 0.1	
Smith[g]	3.29	

*Velocity distribution is not taken into account.

†Velocity distribution is taken into account.

London dispersion forces used:

[a]Johri G K & Srivastava S L, *Indian J. pure appl. Phys.*, 11 (1973), 789.

[b]Murphy J S & Boggs J E, *J. chem. Phys.*, **49** (1968), 3333.

[c]Krishnaji & Srivastava S L, *J. chem. Phys.*, 47 (1967), 1885.

[d]Parameters have been taken from e

[e]Fitz' D E & Marcus R A, *J. chem. Phys.*, 62 (1975), 3788.

[f]Cady W A, *J chem. Phys.*, 60 (1974), 3318.

[g]Smith W V, *J. chem. Phys.*, 25 (1956), 510.

Table 3—Calculated and Experimental Values of Line-width Parameter ($\Delta\nu/p$ in MHz/torr) Considering Dipole-Quadrupole, Quadrupole-Quadrupole and Dispersion Interactions

[$\Theta_{C_6 H_6} = 11.2$ D Å, $\Theta_{OCS}=2$ D Å and $\Theta_{CH_3{}^{81}Br}=0.0$ D Å]

Collision	Rotational line	Experimental	Calculated	
			Vel. distribution not accounted	Vel. distribution accounted
OCS-C_6H_6	$J=1\rightarrow2$	5.14 ± 0.13^a	6.60 ± 0.33	6.83 ± 0.33
$CH_3{}^{81}Br$-C_6H_6	$JK=0,0\rightarrow1,0$	8.77 ± 0.13^b	9.05 ± 0.23	9.35 ± 0.23

[a]Pandey P C, Kirty K K & Srivastava S L, *J. Phys.*, **B4** (1971), 786.

[b]Pandey P C & Srivastava S L, *J. Phys.*, **B 5** (1972), 2074.
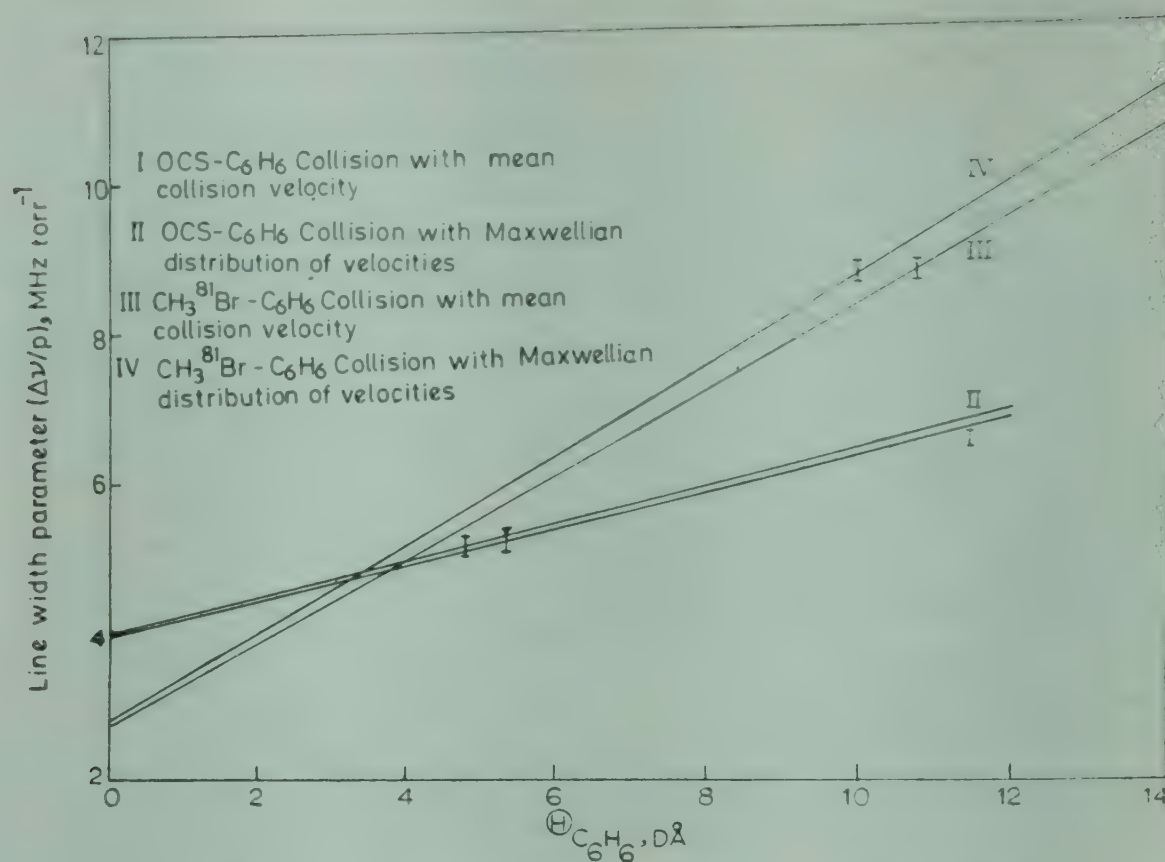
Fig. 1—Plot of line-width parameter versus quadrupole moment of benzene

drops to about 60% at $J_2 = 60$, whereas the contribution of the dipersion forces, is about 5% at $J_2 < 15$ and rises to about 50% at $J_2 = 60$. To evaluate the quadrupole moment of benzene from the OCS-C_6H_6 collision, the line-width parameters have been calculated for $\Theta_{C_6H_6} = 0, 5, 10$ and 15 D Å with mean collision velocity and with Maxwellian distribution of velocities. From the plot of $(\Delta\nu/p)$ versus $\Theta_{C_6H_6}$, the quadrupole moment of benzene has been determined by fitting the calculated $(\Delta\nu/p)$ to the experimental $(\Delta\nu/p)$ as shown in Fig. 1. In Table 4, the values of the molecular quadrupole moment of benzene are compared with the other values.

3.3 CH$_3$ ^{81}Br-C$_6$H$_6$ Collisions

In these collisions, dipole-quadrupole and dispersion interactions have been considered in the calculation of the line-width parameter by the second order perturbation theory with a new boundary condition. In CH$_3$^{81}Br-C$_6$H$_6$ collisions the molecular quadrupole moment of methyl bromide has been assumed to be zero and thus the interactions considered are the dipole-quadrupole and the dispersion forces. The dispersion forces contribute negligibly small (less than 0.5%). Thus from CH$_3$^{81}Br-C$_6$H$_6$ molecular collisions, an upper limiting value of the molecular quadrupole moment of benzene will be obtained.

Using mean collision velocity and $\Theta_{C_6H_6} = 11.2$ D Å, the calculated line-width parameter is 9.05 ± 0.23 MHz/torr, and using Maxwellian distribution of velocity it is 9.35 ± 0.23 MHz/torr; the former value

Table 4—Molecular Quadrupole Moment of Benzene Obtained from Various Methods

Source	Quadrupole moment, D Å
Zeeman effect[24]	11.2
Theoretical calculations[25]	− 18.4
Second virial data[26]	24.0 to 34.0
Microwave line broadening[27]	7.2
ATC 0.2[28,29]	3.55 ± 0.50
MB Theory[28,29]	5.50 ± 0.50
Johri and Srivastava[22]	5.05 ± 0.50
ATC 2[28,29]	9.05 ± 0.30
MB Theory[28,29]	11.10 ± 0.30
Johri and Srivastava[22]	11.00 ± 0.30
Present study	
OCS-C$_6$H$_6$ collisions using mean collision velocity	5.35 ± 0.50
CH$_3$^{81}Br-C$_6$H$_6$ collisions using mean collision velocity	10.80 ± 0.35
Average $\Theta_{C_6H_6}$ = 8.07 ± 3.15	
OCS-C$_6$H$_6$ collisions using Maxwellian distribution of velocities	4.80 ± 0.50
CH$_3$^{81}Br-C$_6$H$_6$ collisions using Maxwellian distribution of velocities	10.00 ± 0.35
Average $\Theta_{C_6H_6}$ = 7.40 ± 3.03	

is about 3% more and the latter value is about 7% more than the experimental value, viz. 8.77 ± 0.13 MHz/torr, reported by Krishnaji et al.[23] To evaluate the quadrupole moment of benzene from $CH_3{}^{81}Br\text{-}C_6H_6$ collision the line-width parameters have been calculated for $\Theta_{C_6H_6} = 0, 11.2$ and 15 D Å and from a plot of $(\Delta v/p)$ versus $\Theta_{C_6H_6}$ the quadrupole moment of benzene has been obtained by fitting the calculated line-width parameters $(\Delta v/p)$ to the experimental line-width parameter as shown in Fig. 1. The values of the quadrupole moment of benzene using Maxwellian distribution of velocities and the mean collision velocities are given in Table 4. The molecular parameters used in the calculation are already given in Table 1.

4. Conclusion

It is observed that Anderson's theory and MB theory yield almost the same width; therefore, the MB theory in respect of giving smaller widths does not seem to be superior over Anderson's theory. However, the importance of the MB theory lies in the fundamental assumption that the line-width parameter is the sum of the line-width contributions of the individual levels. Further, the larger widths (than those obtained from MB theory) obtained by the Anderson-Tsao-Curnutte (ATC) theory[2] are not due to an inadequate model inasmuch as considering total CIF of initial and final states to be unity. The second order perturbation theory used here with a new boundary condition gives a nearly Lorentzian line-shape; simpler in calculation than by the MB theory and explains the observed width within the experimental bars. Further, the quadrupole moment of benzene is 8.07 ± 3.15 D Å using mean collision velocity and 7.40 ± 3.03 D Å using Maxwellian distribution of velocities when average of quadrupole moments obtained in $OCS\text{-}C_6H_6$ and $CH_3{}^{81}Br\text{-}C_6H_6$ collisions is taken. These values of quadrupole moment of benzene are 30-40% less than the value reported by Shoemaker and Flygare.[24] It is to be noted that in OCS-Ar collisions long range forces only are important.

References

1. Anderson P W, *Phys. Rev.*, 76 (1949), 647.
2. Tsao C J & Curnutte B, *J. quant. Spectrosc. radiat. Transfer*, 2 (1962), 41.
3. Krishnaji & Srivastava S L, *J. chem. Phys.*, 41 (1964), 2266; 42 (1965), 1546; 43 (1965), 1345.
4. Johri G K & Srivastava S L, *Chem. Phys. Lett.*, 39 (1976), 579; 45 (1977), 364.
5. Murphy J S & Boggs J E, *J. chem. Phys.*, 43 (1967), 691.
6. Mehrotra S C & Boggs J E, *J. chem. Phys.*, 66 (1977), 5306.
7. Birnbaum G, *Adv. chem. Phys.* 12 (1967), 487.
8. Krishnaji, *J. scient. ind. Res.*, 32 (1973), 168.
9. Rabitz H, *Ann. Rev. Phys. Chem.*, 25 (1974), 155.
10. Krishnaji & Prakash V, *Rev. Chem. Soc.*, 7 (1978), 219.
11. Johri G K, *Molecular collisions and microwave line width*, D Phil thesis, Allahabad University, Allahabad, 1977.
12. Srivastava G P & Kumar A, *J. Phys.*, B7 (1974), 2578; *J. chem. Phys.*, 65 (1976), 293.
13. Mehrotra S C & Boggs J E, *J. chem. Phys.*, 62 (1975), 1453.
14. Smith E W, Giraud M & Cooper J, *J. chem. Phys.*, 65 (1976), 1257.
15. Johri G K & Mehrotra S C, *Can. J. Phys.*, 57 (1979), 69.
16. Mehrotra S C & Boggs J E, *J. chem. Phys.*, 64 (1976), 2796.
17. Story I C, Metchnik V I & Parsons R W, *J. Phys.*, B4 (1971), 593.
18. Murphy J S & Boggs J E, *J. chem. Phys.*, 47 (1967), 4152; 49 (1968), 3333; 50 (1969), 3320; 54 (1971), 2443.
19. Netterfield R P, Parsons R W & Roberts J A, *J. Phys.*, B 5 (1972), 146.
20. Krishnaji & Srivastava S L, *Res. Rep.*, No. 3, (Microwave Laboratory, Physics Department, Allahabad University, Allahabad), 1964.
21. Mehrotra S C, Johri G K & Srivastava S L, *Indian J. pure appl. Phys.*, 16 (1978), 747.
22. Johri G K & Srivastava S L, *Indian J. pure appl. Phys.*, 14 (1976), 917.
23. Krishnaji, Srivastava S L & Pandey P C, *Chem. Phys. Lett.*, 13 (1972), 372.
24. Shoemaker R L & Flygare W H, *J. chem. Phys.*, 51 (1969), 2988.
25. Schweig A, *Molec. Phys.*, 14 (1968), 533.
26. Spurling T H & De A G Rocco, *J. chem. Phys*, 49 (1968), 2867.
27. Hill R M & Smith W V, *Phys. Rev.*, 82 (1951), 451.
28. Pandey P C, Johri G K & Srivastava S L, Paper presented to the National Academy of Sciences Symposium, held at Allahabad, 1972.
29. Johri G K, Prakash V & Srivastava S L, *Indian J. pure appl. Phys.*, 14 (1976), 417.

Molecular Interaction & Thermodynamic Properties of Ternary Liquid Mixtures*

S Singh, N Prasad, R M Kushwaha, K Sivanarayana & S Prakash[†]

Department of Chemistry, University of Allahabad, Allahabad

Isentropic compressibility, intermolecular free-length, available volume and their excess values at 34 C have been computed with the measurement of ultrasound velocity and density in two ternary liquid-liquid systems with toluene as the common component. The systems studied are: 1, acetone-toluene-carbon tetrachloride and 2, acetonitrile-toluene-benzene. Excess compressibility and free-length are negative in both the cases but available volume is positive in 1 and negative in 2. The nature and extent of interaction has been explained in terms of excess properties.

1. Introduction

The intermolecular interactions influence the structural arrangement along with the shape of the molecules. Lagemann[1] was the first to point out the sound velocity approach for qualitative determination of the degree of association in liquids. According to Rao,[2] the molar sound velocity R is a temperature-independent constant for non-associated liquids but when applied to the associated systems, e.g. water, dioxan and methanol, R is found to be temperature-dependent and Weissler[3] applied this quantity to determine the temperature dependence of molecular association for water and methanol. Attempts have been made by Fort and Moore,[4] Kaulgud[5] and Prakash et al.,[6,7] to study the behaviour of binary liquid mixtures by measuring the sound velocity and computing related properties. A few ternary liquid mixtures[8–10] have also been tried. In this paper, we are reporting the results of the study of ternary systems, (1) acetone-toluene-carbon tetrachloride and (2) acetonitrile-toluene-benzene.

2. Experimental Details

The instrument and the method for the measurement of sound velocity has been described previously.[6] The frequency used was 5 MHz and the temperature was maintained at $34 \pm 0.1°C$. AR grade BDH liquids were further purified by standard methods. The liquid mixtures of different compositions were prepared. The mixtures were kept for 2 hr for stabilization and then transferred to the

ultrasonic cell for velocity measurement. The densities were measured pyknometrically. The probable error in the measurement of sound velocity was 0.20% and of density 1 in 10^4.

3. Calculations

According to Newton and Laplace, the isentropic compressibility (β_s) of a homogeneous liquid mixture is given by the expression.

$$v = (\rho \, \beta_s)^{-1/2} \qquad ...(1)$$

where v, is the sound velocity and ρ the density of the system.

Jacobson[11] introduced the concept of intermolecular free-length, i.e. the distance covered by sound wave between the surfaces of molecules to explain ultrasonic velocity in liquids and solutions. The free-length is defined as $L_f = V_a/2Y$, where V_a is available volume per mole and Y the surface area per mole. Jacobson established the relation between ultrasonic velocity, density and intermolecular free-length (L_f) as follows

$$L_f = K \, \beta_s^{1/2} \qquad ...(2)$$

where K is a temperature-dependent constant. By combining the equations of Jacobson[11] and Schaffs,[12] the available volume (V_a) of the liquid mixture is expressed as

$$V_a = V \left(1 - \frac{v}{v_\infty} \right) \qquad ...(3)$$

where V is the molar volume at T K and $v_\infty = 1600$ m/sec. The excess values, A^E have been obtained from the expression

$$A^E = (A)_{mix} - (X_1 A_1^0 + X_2 A_2^0 + X_3 A_3^0) \quad ..(4)$$

where A represents a parameter such as isentropic

---

compressibility, intermolecular free-length or available volume and X_1, X_2 and X_3 are the mole fractions of the components whose parameters are A_1^0, A_2^0 and A_3^0 in the pure state.

4. Results and Discussion

The values of various parameters for the pure liquids are presented in Table 1 and those of the mixtures are given in Tables 2 and 3.

In the two systems that we have studied, we have used liquids of different nature. Acetone is polar and so is acetonitrile. Though acetonitrile does not form hydrogen bond, its large dipole moment may lead to large electrostatic forces. Benzene and toluene are highly polarizable and weakly polar molecules. Carbon tetrachloride is non-polar but it does not always behave as an inert solvent.[13] Arrawatia and coworkers[14] observed increased values of relaxation time for some substituted benzenes in carbon tetrachloride. They explained this difference as due to the presence of weakly polar CCl_4 molecules. Adgaokar *et al.*[15] have explained the greater association of *m*-toluidine in CCl_4 due to the small positive charge on carbon of carbon tetrachloride. Thus the mixtures attempted here consist of polar and weakly polar liquids.

Table 1—Ultrasound Velocity and other Parameters in Pure Liquids at 34°C

Liquid	Ultrasound velocity (m/sec)	Density (g/ml)	Isentropic compressibility $\times 10^{12}$ (cm²/dyne)	Intermolecular free-length (Å)	Molar volume (ml/mole)	Available volume (ml/mole)
Benzene	1256	0·8748	72·40	0·5403	89·29	19·20
Toluene	1263	0·8576	73·61	0·5448	108·06	22·78
Acetone	1127	0·7748	101·62	0·6401	74·96	22·16
Acetonitrile	1244	0·7665	84·30	0·5830	53·56	11·92
Carbon tetrachloride	891	1·5683	80·32	0·5691	98·10	43·47

Table 2—Ultrasound Velocity and other Parameters in Ternary Liquid Mixtures at 34°C

X_1^*	X_2^*	Ultrasound velocity (m/sec)	Density (g/ml)	Isentropic compressibility $\times 10^{12}$ (cm²/dyne)	Intermolecular free-length (Å)	Molar volume (ml/mole)	Available volume (ml/mole)
			1. Acetone-toluene-carbon tetrachloride				
0·60	0·00	1222	0·8297	80·71	0·5705	94·62	22·35
0·50	0·10	1167	0·9060	81·04	0·5716	93·47	25·29
0·40	0·20	1113	0·9850	81·95	0·5748	92·23	28·07
0·30	0·30	1065	1·0636	82·89	0·5781	91·22	32·50
0·20	0·40	1021	1·1463	83·68	0·5809	90·02	·32·58
0·10	0·50	979	1·2326	84·65	0·5842	88·73	34·44
0·00	0·60	941	1·3162	85·80	0·5882	87·78	36·15
0·50	0·50	1146	1·2032	63·28	0·5051	102·21	29·00
			2. Acetonitrile-toluene-benzene				
0·00	0·60	1253	0·8190	77·77	0·5560	68·21	14·80
0·10	0·50	1256	0·8276	76·59	0·5557	73·68	15·84
0·20	0·40	1259	0·8361	75·45	0·5516	79·05	16·85
0·30	0·30	1266	0·8432	73·99	0·5462	84·44	17·63
0·40	0·20	1264	0·8490	73·72	0·5452	89·88	18·87
0·50	0·10	1264	0·8534	73·34	0·5438	95·40	20·03
0·60	0·00	1264	0·8589	72·96	0·5424	100·85	21·18
0·50	0·50	1258	0·8271	76·40	0·5550	80·51	17·21

Table 3—Excess Properties in Ternary Liquid Mixtures at 34°C

X_1^*	X_2^*	Excess density (g/ml)	Excess isentropic compressibility $\times 10^{12}$ (cm²/dyne)	Excess intermolecular free-length (Å)	Excess molar volume (ml/mole)	Excess available volume (ml/mole)
			1. Acetone-toluene-carbon tetrachloride			
0·60	0·00	+0·0082	−4·10	−0·0124	−0·20	−0·18
0·50	0·10	+0·0131	−4·44	−0·0137	−0·37	+0·90
0·40	0·20	+0·0208	−4·21	−0·0130	−0·62	+1·40
0·30	0·30	+0·0280	−3·94	−0·0121	−0·65	+3·76
0·20	0·40	+0·0393	−3·82	−0·0117	−0·67	+1·77
0·10	0·50	+0·0543	−3·52	−0·0109	−1·17	+1·56
0·00	0·60	+0·0665	−3·04	−0·0093	−1·14	+1·20
0·50	0·50	−0·0062	−13·78	−0·0518	−0·93	−4·12
			2. Acetonitrile-toluene-benzene			
0·00	0·60	+0·0121	−2·13	−0·0112	+0·07	−0·14
0·10	0·50	+0·0121	−2·20	−0·0075	+0·08	−0·16
0·20	0·40	+0·0120	−2·23	−0·0076	0·00	−0·22
0·30	0·30	+0·0105	−2·57	−0·0091	−0·06	−0·50
0·40	0·20	+0·0077	−1·37	−0·0061	−0·07	−0·33
0·50	0·10	+0·0034	−1·00	−0·0035	−0·02	−0·23
0·60	0·00	+0·0003	−0·27	−0·0009	−0·00	−0·14
0·50	0·50	+0·0178	−2·34	−0·0081	−0·30	−0·03

*X_1 is the mole fraction of toluene and X_2 that of CCl_4 in 1 and acetonitrile in 2.

When the mole fraction of acetone in 1 and that of benzene in 2 is kept constant at 0·4 and those of other two components of mixtures are varied, ultrasound velocity increases in both the cases and isentropic compressibility and free-length decrease with the increasing mole fraction of toluene as shown in Table 2. The excess values of isentropic compressibilities and free-length are negative in both the cases. On the basis of mode of sound propagation given by Eyring and Kincaid,[16] the increased free-length in the solution due to the process of mixing, results in the lowering of sound velocity. This indicates that the intermolecular free-length is the predominant factor in determining the nature of variation of sound velocity in the mixtures.

Fort and Moore[4] found that the increasing negative value of excess compressibility indicates greater interaction between the components of the mixtures. In system 1, β_s^E is found to be negative. The increasing negative value of excess compressibility might also be due to weakly polar CCl_4 molecules.[14,15]

This leads to stronger interaction in the case 1 than in case of 2 in which β_s^E is negative but its magnitude is less than that in 1.

Table 3 shows that while the value of excess molar volume is found to be negative in system 1, it changes sign from positive to negative in system 2. This change from positive to increasingly negative value (of excess molar volume) is interpreted in terms of closer approach of unlike molecules leading to the reduction in the compressibility and volume. Dispersion forces which are always operative, make a positive contribution to the excess values, while dipole-dipole, dipole-induced dipole, charge transfer interactions and hydrogen bonding between unlike components make a negative contribution.[4]

References

1. Lagemann R T & Dunbar W S, *J. phys. Chem.*, 49 (1945), 428.
2. Rao M R, *J. chem. Phys.*, 9 (1941), 682.
3. Weissler A, *J. Am. chem. Soc.*, 71 (1949), 1272.
4. Fort R J & Moore W H, *Trans. Faraday Soc.*, 61 (1965), 2102.
5. Kaulgud M V, *Acustica*, 10 (1960), 316.
6. Prasad N, Singh R, Prakash O & Prakash S, *Indian J. pure appl. Phys.*, 14 (1976), 676.
7. Prakash S, Singh R & Prasad N, *Acta Chim. (Budapest)*, 88 (1976), 371.
8. Chaturvedi C V & Prakash S, *Acustica*, 27 (1972), 248.
9. Prasad N, Prakash O, Singh S & Prakash S, *Ultrasonics*, 16 (1978), 77.
10. Prasad N & Prakash S, *J. chem. Engng Data*, 22 (1977), 49.
11. Jacobson B, *Acta chem. scand.*, 6 (1952), 1485.
12. Schaafs W, *Z. Phys*, 114 (1939), 110; 115 (1940), 69.
13. Joesten M D & Schaad L J, *Hydrogen bonding* (Marcel Dekker, New York), pp. 162, 170.
14. Arrawatia M L, Gupta P C, & Sisodia M L, *Indian J. pure appl. Phys.*, 15 (1977), 770.
15. Adgaokar C S & Kher V G, *Indian. J. pure appl. Phys.*, 11 (1973), 535.
16. Eyring H & Kincaid J F, *J. chem. Phys.*, 6 (1938), 620.

Molecular Orbital Energies & X-ray K-Absorption Spectra of Copper in Metal & Its Oxides

U C Srivastava

Chemistry Department, C M P College, Allahabad

The molecular orbital (MO) method has been employed to calculate energy separations in the K-absorption spectra of copper (up to 30 eV from the main edge) in Cu metal, Cu_2O and CuO. The results are found to agree reasonably well with the experimental data reported earlier.

1. Introduction

Molecular orbital (MO) theory has, in recent years, been successfully applied to interpret X-ray K-absorption spectra of metals in compounds.[1] According to the MO approach, the K-absorption process is associated with the excitation of a 1s electron to successive unoccupied MOs of appropriate symmetry, and energy separations between the X-ray lines are equivalent to energy differences between MO ionization potentials.[2] For the first transition series metals, qualitative estimates of the involvement of metal 4p orbitals in unoccupied MOs form the basis of interpretations.[3] However, the quantitative aspects necessary for a valid MO model do not seem to have been completely worked out so far. The problem seems to be a tractable one at least for simple molecules. Agarwal et al.[4] have recently reported the K-absorption fine structure spectra of copper metal, Cu_2O and CuO. An attempt has, therefore, been made in the present work to calculate approximate MO energies in case of copper metal, Cu_2O and CuO and to compare the results with the reported energy separations in their spectra.

2. MO Energy Calculations

2.1 Model

As a first approximation, the molecular orbitals have been regarded as linear combinations of atomic orbitals (LCAO-MO) and interactions only between orbitals on adjacent atoms have been considered (Hückel approximation). The calculations of energies of MOs in terms of atomic parameters and the use of symmetry and molecular orbital-group theory to simplify calculations are extensively dealt with in the literature.[5,6] In the present treatment, the combination of atomic orbitals has been effected in successive steps combining two orbitals at a time. Accordingly, the secular determinant used is of the form:

$$\begin{vmatrix} H_{ii} - E & H_{ij} - SE \\ H_{ij} - SE & H_{jj} - E \end{vmatrix} = 0 \qquad ...(1)$$

According to the extended Hückel theory (EHT), the most commonly used values of the diagonal matrix elements H_{ii}, H_{jj} etc. are equated to the negative of valence state ionization potentials (in au) of the respective atomic orbitals whose values are available from the spectroscopic data. The values for copper and oxygen are noted below.

Copper	Oxygen (Ref. 7)
4s : 7·6 eV (Ist ionization potential)	2s : 28·4 eV
3d : 20·4 eV (2nd ionization potential)	2p : 13·6 eV
4p : 3·6 eV (4s-4p separation being 4 eV)	

The off-diagonal elements have been evaluated using the expression

$$H_{ij} = 0.5 \ K \ (H_{ii} + H_{jj}) \ S_{ij} \qquad ...(2)$$

where the value of K giving best results has been found to be 2 (Ref. 6). The overlap integral S_{ij} has been taken to be equal to 0·5 for copper metal. For the oxides, its value has been calculated according to the equation[6] :

$$S (R) = e^{-R} (1 + R + R^2/3) \qquad ...(3)$$

where R is the Cu—O bond distance. The values were found to be 0·483 for Cu_2O (R=1·85Å) (Ref. 8) and 0·4785 for CuO ($R_{(average)}$ = 1·92 Å) (Ref. 9). The MO energies were computed by solving the determinant for its roots (E). It may be added that in order to render the MO treatment particularly useful for interpreting K-absorption spectra of copper, the involvement of metal 4p orbitals has been purposely developed in the LCAO-MOs (Ref. 3).

2.2 Copper Metal

In copper metal, the $K\beta_5$ emission spectra are known to be due to a $3d \rightarrow 1s$ quadrupole transition made possible by the overlap of the $3d$ with the $4p$ band (Refs. 2, 3). In MO theory, this would basically amount to the formation of molecular orbitals as a result of interactions between $3d$ and $4p$ atomic orbitals on adjacent copper atoms. As mentioned above, in a simplified MO approach directed to study the K-absorption spectra, it may be expedient to examine the involvement of metal $4p$ orbitals in MOs using only a sample number of typical combinations of metal $3d$, $4s$ and $4p$ orbitals as shown in Table 1.

2.3 Cuprous Oxide

In Cu$_2$O the oxygen atom is flanked by two copper atoms in a linear geometry. The basis orbitals for the oxygen atom are $2s$, $2p_x$, $2p_y$, $2p_z$. For the two copper atoms, one $4s$ orbital from each is directed towards the central oxygen. However, as outlined above, combinations of two sets of metal $3d$ and $4p$ orbitals of appropriate orientation have also been included. For the sake of convenience the z-axis is taken to be the molecular axis. The symmetry point group of Cu$_2$O is $D_{\infty h}$. Operations within this group lead to the following irreducible representations for sigma orbitals:

$$\Gamma_\sigma = \Sigma_g^+ + \Sigma_u^+ \qquad .. (4)$$

The oxygen valence shall orbitals may be classified as

$$\Sigma_g^+ : 2s; \quad \Sigma_u^+ : 2p_z; \quad \pi_u : 2p_x\, 2p_y$$

Accordingly, the interacting combinations of atomic orbitals and the calculated MO energies are listed in Table 2.

It may be noted from Table 2 that after forming all appropriate combinations of metal and oxygen orbitals, one set of metal $4p_\pi$ orbitals is left over with no corresponding orbitals on oxygen. These have been mixed with two $3d_{x^2-y^2}$ orbitals of the metal itself; this would also be necessary to account for the $K\beta_5$ emission spectra (Ref. 2, 3). Further it is known that in Cu$_2$O solid, copper atoms of two adjacent Cu$_2$O units fall close together at 3.1 Å which is about the sum of neutral radii (Ref. 8).

2.4 Cupric Oxide

The CuO molecule belongs to $C_{\infty v}$ symmetry in which the group theoretical representations for sigma and pi orbitals are Σ^+ and π respectively. The basis orbitals are $4s$, $4p_z$, $4p_\pi$ and $3d_{z^2}$ for copper and $2s$, $2p_z$ and $2p_\pi$ for oxygen. MO details for CuO similar to Tables 1 and 2 are given in Table 3.

Table 1—Interacting Orbitals and MO Energies in Copper Metal

	Interacting orbitals	MO energies (eV)	
		Bonding	Anti-bonding
Ψ_1	$4s$-$4s$	0.0	$10.12*$
Ψ_2	$4s$-$4p$	-0.667 (1)	8.13
Ψ_3	$3d$-$4p$	-4.5 (2)	20.5
Ψ_4	$4p$-Ψ_1^a	-1.3 (2)	10.5

a, anti-bonding; numbers in parentheses indicate distribution of 5 electrons : 2 from $3d$ and 1 each from $4s$;
*Eliminated in being mixed with $4p$ giving Ψ_4.

Table 2—Interacting Orbitals and MO Energies in Cu$_2$O

	Interacting orbitals	MO energies (eV)	
		Bonding	Anti-bonding
$\Sigma_{g_1}^+$	$4s$-$2s$	-3.88 (2)	28.5 *
$\Sigma_{g_2}^+$	$4p_z$ - $\Sigma_{g_1}^{+a}$	-6.2 (2)	28.9
$\Sigma_{u_1}^+$	$4s$ - $2p_z$	0.2	$15.25*$
$\Sigma_{u_2}^+$	$4p_z$ - $\Sigma_{u_1}^{+a}$	-2.3	15.4
π_{u_1}	$4p_\pi$ - $2p_\pi$	-2.6 (4)	15.3
π_{u_2}	$4p_x$ - $3d_{x^2-y^2}$		
	$4p_y$ - $3d_{x^2-y^2}$	-4.5 (4)	20.5

*Eliminated in being combined with metal $4p_z$ to give $\Sigma_{g_2}^+$ and $\Sigma_{u_2}^+$; numbers in parentheses indicate distribution of the 12 electrons : 6 from copper $[2 \times (3d_{x^2-y^2}, 4s^1)]$ and 6 from oxygen ($2s^2\, 2p^4$).

3. Discussion

The complete array of molecular orbitals and the distribution of electrons for copper metal, Cu$_2$O and CuO are shown in Fig. 1 together with the atomic orbitals of copper and oxygen. The energies (in eV) are plotted to scale.

3.1 Copper Metal

Inspection of Table 1 and Fig. 1 reveals that as electrons are filled into bonding MOs in the increasing order of energy, the first vacancy available for the transition of $1s$ electron lies in the bonding MO Ψ_2 which, in the present sample study, is singly occupied. This transition ($1s \rightarrow \Psi_2^b$) would accordingly correspond to the onset of photoionization represented by K_1 in the K-absorption spectra of the metal.[4] Conventionally, therefore, the energy of this MO (-0.667 eV) may be reckoned as zero of energy for describing other energy features of the spectra of the metal as well as of Cu$_2$O and CuO. It may be noted

here that the nature of this MO ($4s$-$4p$) is cons'stent with the earlier observation that the initial rise K_1 in copper metal corresponds to the transition to unoccupied states having admixed $4s$-$4p$ symmetry.[4]

At higher energy (0·0 eV, Table 1) we find an empty bonding MO Ψ_1^b having s-character. Since $1s \rightarrow 4s$ is a forbidden transition, the consequent decrease in absorption seems to be reflected in the

Table 3—Interacting Orbitals and MO Energies in CuO

	Interacting orbitals	MO energies (eV)	
		Bonding	Anti-bonding
Σ_1^+	$4s$-$2s$	−3·6 (2)	28·9*
Σ_2^+	$4p_z$ - Σ_1^{+a}	−6·1 (2)	29·01
Σ_3^+	$3d_z{}^2$-$2p_z$	+0·95 (1)	24·3
π	$4p_\pi$-$2p_\pi$	−2·5 (4)	15·98

*Eliminated in the formation of Σ_2^+; numbers in parentheses indicate distribution of 9 electrons together from copper $(3d^2{}_{z^2}\,4s^1)$ and oxygen $(2s^2\,2p^4)$.

Fig. 1—Molecular orbital energy level diagram showing the atomic and molecular orbitals for copper metal, Cu_2O and CuO

appearance of a kink just above K_1 on the spectra. It may be added that earlier[4] too, this kink has been attributed to the presence of levels having predominance of s-character. Beyond Ψ_1^b we have an anti-bonding MO Ψ_2^o at 8·797 eV (here and henceforth, the energies are with respect to K_1 in metal: −0·667 eV), which is seen to be mixed with p-character. A transition to this would, therefore, result in a rise in absorption intensity above the kink as observed on the spectra.

Again, the absorption maximum A (16·02 eV) interestingly appears to resemble a kink type absorption in which the dip in intensity leads to α at 19·41 eV. On considerations of intensity based on the nature of interactions involved in the MOs Ψ_4^a and Ψ_3^a, it seems likely to attribute the features, A and α to the transitions $1s \rightarrow \Psi_4^a$ and $1s \rightarrow \Psi_3^a$ respectively. So far as α is concerned, it will be subsequently seen that similar MO's are responsible for this feature in case of Cu_2O and CuO as well. However, while the agreement in energy between the MO Ψ_3^a (21·1 eV) and α (19·41 eV) appears to be satisfactory, that between Ψ_4^a (11·167 eV) and A (16·02 eV) is poor.

3.2 Cuprous Oxide

In Cu_2O, the MO description (Table 2, Fig. 1) shows that the lowest energy (unoccupied) MO available for initial K-absorption is Σ_2^{+b} at −1·63 eV (−2·3 eV, Table 2) which may, therefore, be predicted as the shift of the K_1 edge in Cu_2O with respect to that in metal. It is interesting to note that this compares reasonably well with the reported experimental edge-shift (−2·17 eV) (Ref. 4). Further, as compared to Σ_u^{+b}, the MO $\Sigma_{u_1}^{+b}$ seems to involve more s- and less p- character as suggested by their respective modes of formation. Since this may lead to a relative decrease in absorption, the kink observed on the edge in case of Cu_2O may possibly be related to the transition $1s \rightarrow \Sigma_{u_1}^{+b}$. This is supported by the fact that the energy of the MO $\Sigma_{u_1}^{+b}$ (0·867 eV) is about the same as that of the kink on the spectra. In a likewise manner, the spectral features A, α and B may also be interpreted, both qualitatively and quantitatively, in terms of transitions specified in Table 4. It is seen that the maximum difference between estimated and observed energies is less than 2 eV.

A comparison of the spectra of copper metal and Cu_2O would show that the intensity of the principal absorption maximum A is markedly greater in case of Cu_2O. This may be explained satisfactorily in
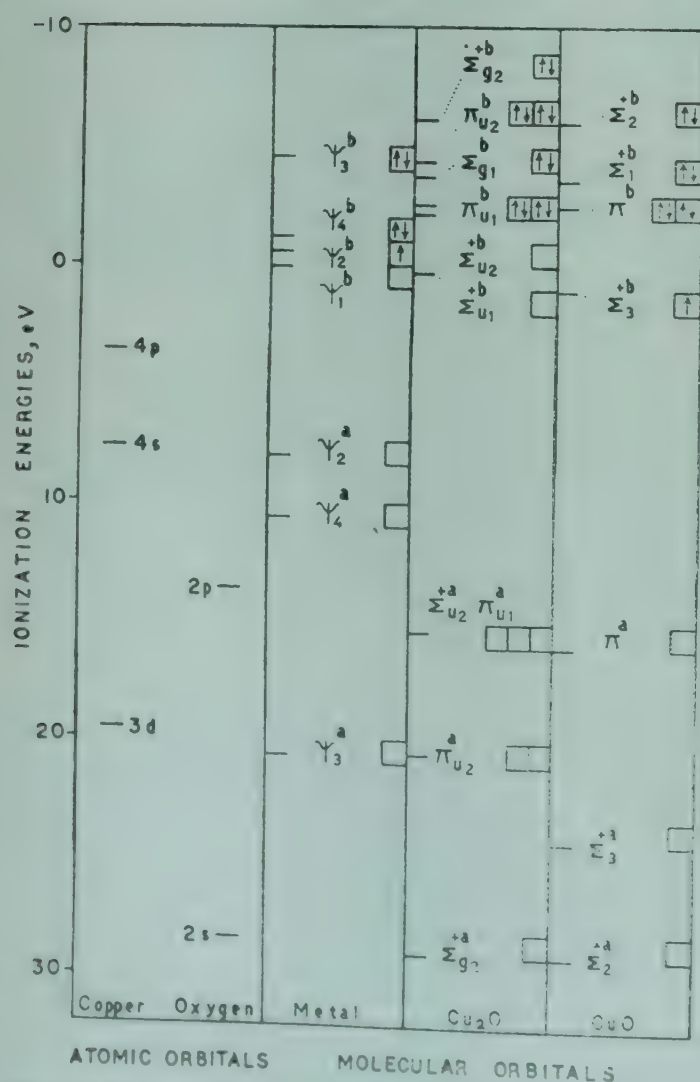
terms of the enhanced p-character in the corresponding MO for Cu_2O as may be clear from a comparative study of the respective MO pictures. On the other hand, the nearly equal intensity of α observed in case of copper metal and Cu_2O may probably be attributed to the fact that the corresponding MOs arise out of metal $3d$-$4p$ interactions in both.

3.3 Cupric Oxide

The distribution of electrons in the bonding orbitals for CuO (Table 3) clearly suggests that the initial K-absorption in it would correspond to the transition $1s \rightarrow \Sigma_3^{+b}$. The chemical shift of K_1 in CuO relative to that in metal would, therefore, be 1.617 eV according to the MO calculation as against the measured value of 0.67 eV. The transition assignments for the features A, α and B as suggested by the MO picture are as listed in Table 5. It is interesting to see that the difference between calculated and observed energies here is less than 1 eV except for α (> 2 eV).

A look at the spectra for CuO shows that there is intense absorption at the maximum A as compared to that in the case of Cu_2O. This can be explained as follows. The MO π^a corresponding to the principal absorption maximum A in case of CuO is of pure p-type, (Table 3), whereas one of the corresponding MOs for Cu_2O $(\Sigma_{u_2}^{+a})$ is of the mixed s-p type (Table 2), $\Sigma_{u_2}^{+}$ resulting from $4p_z - \Sigma_{u_1}^{+a}$ and $\Sigma_{u_1}^{+a}$ in turn, resulting from $2p_z$ and $4s$. It is well known that the intensity for the transition $1s \rightarrow$ pure p would be expected to be greater than for $1s \rightarrow sp$ (mixed). Further, the amount of p-character in these MOs may be expected to be greater (and hence greater intensity) in the case of CuO possibly for another reason: these MOs involve predominance of oxygen $2p$ orbitals and the stoichiometric oxygen-to-metal ratio is greater in CuO (1/1) than in Cu_2O (1/2). A similar explanation may hold true for the marked decrease in the intensity of B in the spectra of CuO since the corresponding MOs Σ_2^{+a} (CuO) and $\Sigma_{g_2}^{+a}$ (Cu_2O) in both involve the symmetry forbidden $2s$ orbitals of oxygen, and are virtually localized on the same.

Table 4—Transition Assignments and MO Energies in Cuprous Oxide

Transition		Estimated energy(eV)	Observed energy (eV)
K_1	$1s \rightarrow \Sigma_{u_2}^{+b}$	-1.633	-2.17
A	$\begin{cases} 1s \rightarrow \Sigma_{u_2}^{+a} \\ 1s \rightarrow \pi_{u_1}^a \end{cases}$	16.067 15.967	14.25
α	$1s \rightarrow \pi_{u_2}^a$	21.167	19.82
B	$1s \rightarrow \Sigma_{g_2}^{+a}$	29.567	30.00

Table 5—Transition Assignments and MO Energies in Cupric Oxide

Transition		Estimated energy (eV)	Observed energy (eV)
K_1	$1s \rightarrow \Sigma_3^{+b}$	1.617	0.67
A	$1s \rightarrow \pi^a$	16.647	15.75
α	$1s \rightarrow \Sigma_3^{+a}$	24.967	27.29
B	$1s \rightarrow \Sigma_2^{+a}$	29.677	29.73

Finally, it may be concluded on the basis of the foregoing discussion that a specialized treatment of the MO theory may be satisfactorily used to explain, not only in a qualitative but also a quantitative way, the Kossel fine structure of the K-absorption spectra which is the main region of interest to chemists.

References

1. Srivastava U C & Nigam H L, *Coord. chem. Rev.*, **9** (1973), 275.
2. Best P E, *J. chem. Phys.*, **49** (1968), 2797.
3. Best P E, *J. chem. Phys.*, **44** (1966), 3248.
4. Agarwal B K, Bhargava C B, Vishnoi A N & Seth V P, *J. Phys. Chem. Solids*, **37** (1976), 725.
5. Cotton F A, *Chemical applications of group theory* (Wiley-Interscience, New York), 1971.
6. Chandra A K, *Introductory quantum chemistry* (Tata McGraw-Hill, New Delhi), 1974.
7. Urch D S, *J. Phys.*, C9 (1970), 1275.
8. Niggli P, *Z. Krist.*, **57** (1922), 253.
9. Tunell G, Posjnak E & Ksanda C, *Z. Krist.*, **90** (1935), 120.

EPR Study of Molecular Order in p-n-Octyloxy Benzylidene-p-Toluidine Using VAAC Probe

A S N Rao & C R K Murthy

Department of Physics, Nagarjuna University, Nagarjuna Nagar

and

Kusum Sahu & T Rs Reddy

Solid State Physics Laboratory, Delhi 110 006

The molecular ordering with temperature in both nematic and smectic-A phases of the liquid crystal (p-n-octyloxy benzylidene)-p-toluidene (OBT) has been studied, with the help of EPR technique using VAAC as the probe. The order increased with the lowering of temperature through the nematic phase. But there was a sudden fall when smectic-A phase was obtained by cooling the nematic phase in a magnetic field of 3300 gauss. Real smectic order was obtained when the sample was cooled from nematic phase in a magnetic field of 9800 gauss. The orientation studies indicated that the molecules of the liquid crystal retained their alignment even upon rotation of the sample in the magnetic field.

1. Introduction

For the past several years, it has been established that the molecular order and the motion in liquid crystal can be conveniently studied by monitoring the changes in the EPR spectra, the hyperfine structure in particular, as the liquid crystal sample is taken through its different phases. Liquid crystals being diamagnetic, it is necessary to dope the sample with a small amount of a paramagnetic 'probe' whose structure is such that the probe molecules follow the ordering of the liquid crystal to a great extent. Vanadyl acetyl acetonate (VAAC) with its planar structure has been established as one of the most convenient probe for this purpose. The eight-line hyperfine structure with a spread of about 750 gauss in the isotropic phase shows remarkable changes as the liquid crystal goes through the various phases.

(p-n-Octyloxy benzylidene)-p-toluidine (OBT) is a smectic liquid crystal exhibiting the following phases : isotropic liquid, nematic, smectic-A and solid. In smectic-A mesophase, the molecules are orthogonal to the layers. We report in this communication, the EPR study of the molecular order in liquid crystal OBT using VAAC as the probe. The variation of the order with temperature was studied. In smectic phase, the angular variation of the average hyperfine splitting of VAAC was studied after cooling the sample through the nematic to smectic-A phase in a magnetic field of 9800 gauss.

2. Experimental Procedure

OBT was obtained commercially from E Merck (FRG) in pure form and recrystallized for further purification. The transition temperatures of the purified sample are found to be :

$$\text{Solid} \underset{67^\circ C}{\rightleftharpoons} \text{Smectic A} \underset{69 \cdot 8' C}{\rightleftharpoons} \text{Nematic} \underset{77 \cdot 8^\circ C}{\rightleftharpoons} \text{Isotropic}$$
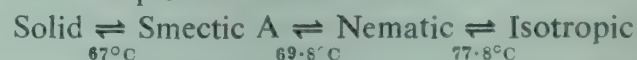
The spin probe VAAC was prepared in our laboratory using the standard procedure.[1]

The samples for the EPR study were prepared in 4mm quartz tubes. A small speck of VAAC was mixed with the powder of OBT taking care that its mole fraction does not exceed 10^{-3} and the mixture was dropped in the tube. The mixture was then heated with hot air blower with frequent shaking until VAAC homogeneously mixed with the solvent OBT.

The EPR spectra were obtained with Varian E-12 X-band EPR spectrometer. The temperature of the sample was controlled using Varian E-257 variable temperature accessory. To avoid possible errors in the temperature recordings due to the thermal gradients from the heating system to the sample, the temperature of the sample was measured with a copper-constantan thermocouple.

The sample was taken to its isotropic phase and the EPR spectra were recorded at a series of descending temperatures throughout the nematic and smectic phases. Sufficient time had been given at each temperature for the sample to attain thermal equilibrium.

especially when there is a phase transition either from isotropic to nematic or nematic to smectic-A phases. The smectic phase was obtained by cooling the nematic phase in a high magnetic field of 9800 gauss. In the smectic phase, the sample was rotated with respect to the magnetic field direction and the spectra were recorded at various angles.

3. Theory

The EPR spectrum of VAAC with $S = \frac{1}{2}$ and $I = \frac{7}{2}$ consists of eight well resolved hyperfine lines around $g = 2$. When VAAC is aligned in a nematic host matric and can freely tumble, the spin-Hamiltonian can be written as[3]

$$\mathscr{H} = \beta \, g \, H_z \, S_z + a \, \mathbf{I} \cdot \mathbf{S} + \tfrac{1}{3} (\Delta g \, \beta \, H_z + b \, I_z) \left\langle 3 \cos^2 \theta - 1 \right\rangle S_z$$

where the magnetic field H_z is taken along the z direction. S_z and I_z are the components of electronic and nuclear spins S and I respectively along the magnetic field direction, a is the average hyperfine splitting equal to $\frac{1}{3} (A_{\parallel} + 2 A_{\perp})$ and $b = (A_{\parallel} - A_{\perp})$, $A_{\parallel}$ and $A_{\perp}$ being parallel and perpendicular components of hyperfine coupling constants. The separation between two hyperfine lines corresponding to $\pm m_I$, $2 \left\langle a \right\rangle m_I$, is given by

$$2 \left\langle a \right\rangle m_I = 2 \, a \, m_I + 2 \, (1/3 b) \left\langle 3 \cos^2 \theta - 1 \right\rangle m_I,$$

or

$$\left\langle 3 \cos^2 \theta - 1 \right\rangle = \left(\left\langle a \right\rangle - a \right) \Big/ \tfrac{1}{3} b$$

where $\left\langle a \right\rangle$ is the effective vanadium hyperfine coupling constant obtained from the experimental spectra in the nematic phase. Using the previous definitions for a and b, the order parameter (σ) can be written as

$$\sigma = \frac{1}{2} \left\langle 3 \cos^2 \theta - 1 \right\rangle = \frac{1}{2} \left(\left\langle a \right\rangle - a \right) \Big/ \left(a - A_{\perp} \right) \qquad \ldots (1)$$

The liquid crystal tends to align the plane of the VAAC molecules parallel to the plane of the liquid crystal molecules. The complete ordering of the liquid crystal molecules in the magnetic field would then correspond to a σ value of -0.5. The above formula for the order parameter holds good in the smectic phase also unless it is highly viscous. The angular variation of the average hyperfine splitting in the smectic phase is given by[3]

$$\left\langle a \right\rangle = a + \frac{b}{3} \, \sigma \, (3 \cos^2 \alpha - 1) \qquad \ldots (2)$$

4. Results and Discussion

Typical EPR spectra of VAAC in OBT obtained in nematic and smectic phases are shown in Fig. 1. The onset of the isotropic to the nematic phase transition was clearly evident from the sudden contraction of the hyperfine structure at the transition temperature. An increase in the degree of order on lowering the temperature in the nematic phase was indicated by the reduction in the hyperfine separation. The degree of order was calculated from Eq. (1) and the results are plotted in Fig. 2. The value of -0.2 for the order parameter just at the beginning of the nematic phase is typical for the nematic phase of liquid crystals. The order increases in magnitude further up to -0.27 at 70°C. This increase represents the long range ordering of the domains in the liquid crystal.

When smectic-A phase was achieved at 69°C under the normal magnetic field of 3300 gauss, there is an increase of hyperfine splitting from 85 to 94 gauss. Further decreases of temperature resulted in a decrease of hyperfine splitting. This indicates that the interaction of the normal 3300 gauss magnetic field with the molecules of the sample is not strong enough to achieve smectic phase order. The liquid crystal may form into various domain structures which have preferred directions slightly different from the field direction. The variation is such that the order parameter has fallen down from 0.27 to 0.16 in magnitude. The further increase of order with decrease of temperature is in agreement with the results of Francis and Luckhurst.[4]

Using a high magnetic field of 9800 gauss during nematic to smectic-A transition, a small decrease of hyperfine splitting was observed. Further decrease of temperature in the lower field of 3300 gauss led
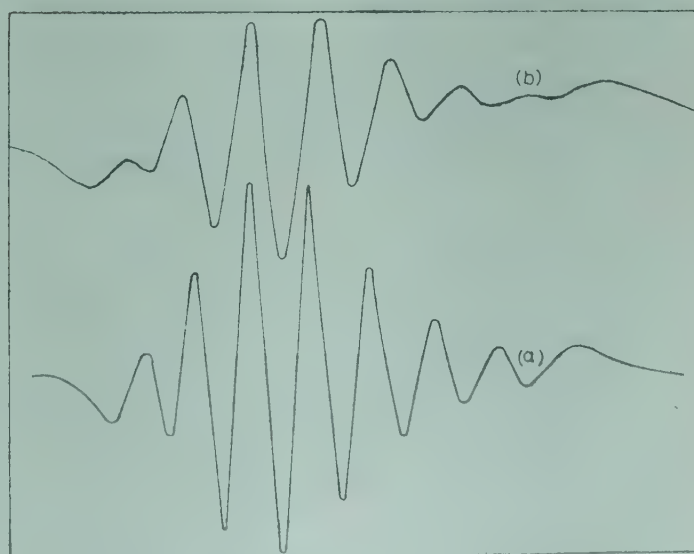
Fig. 1—X-band EPR spectra of VAAC in OBT (a) in nematic phase, $T = 72°C$ and (b) in smectic-A phase, $T = 69°C$
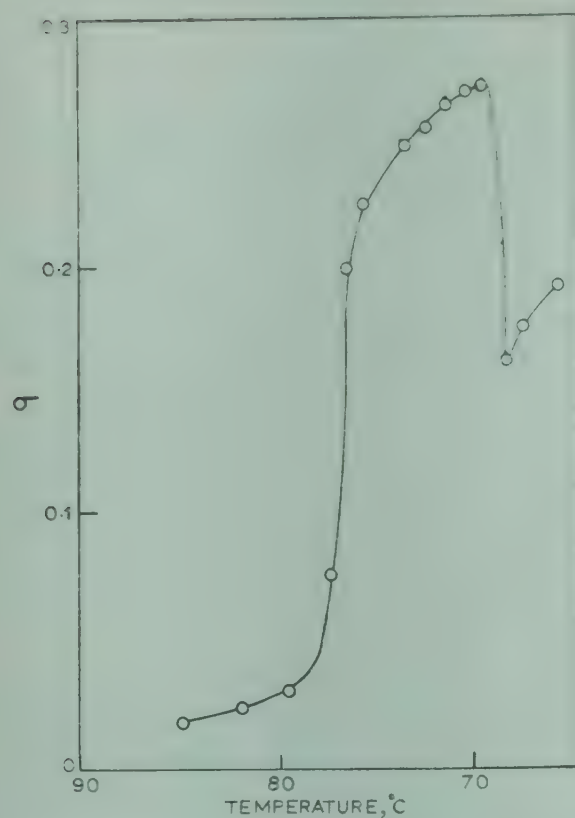
Fig. 2—The variation of order parameter (σ) with temperature in OBT in a magnetic field of 3300 gauss

Fig. 3—Angular variation of average hyperfine splitting of VAAC in OBT in smectic-A phase, after the nematic to the smectic-A phase transition in a magnetic field of 9800 gauss

to a further decrease of hyperfine splitting indicative of an increase in the order. In this high field treatment, the interaction between the molecules of the liquid crystal and the magnetic field is high enough to retain the order achieved in the nematic phase. The small increase of the order in the smectic phase may be due to strong lateral attractions between the molecules of the liquid crystal that are extended in the smectic-A phase.

In the smectic-A phase at 69°C, the sample is rotated in the magnetic field from 0 to 180°, and the EPR spectra were recorded at intervals of 10°. The angular variation of the hyperfine separation is shown in Fig. 3, which is symmetric about 90° as expected. The angular variation of the hyperfine structure with respect to the direction of the magnetic field shows that the molecules of the liquid crystal maintained their original alignment. The

solid curve in Fig. 3 represents the function
$$-107 + 10 \cdot 1 \, (3 \cos^2 \alpha - 1)$$
taking the value of the order parameter σ at 0° orientation as equal to $-0 \cdot 28$. The discrepancy between the calculated and the observed angular variation in the region of 70° to 120° where the observed values fall below the calculated values, may result from the restriction on the tumbling of the VAAC molecules in the liquid crystal. This shows that the smectic layers are not fluid.

The authors thank the Director, Solid State Physics Laboratory, Delhi, for giving permission to carry out this work at the Laboratory. The authors are also thankful to Mr M Gopal Rao and Dr H P Bhattacharya for their keen interest and encouragement.

References

1. Byrant P E & Fenelius W C, *Inorganic Synthesis*, **5** (1957), 115.
2. Fryburg G C & Gelerinter E, *J. chem. Phys.*, **52** (1970), 3378.
3. Fryburg G C, Gelerinter E & Fishel D L, *Molec. crystals liqd crystals*, 16 (1972), 39.
4. Francis P D & Luckhurst G R, *Chem. Phys. Lett.*, **3** (1969), 213.

Applications of the Coulomb-Glauber-Ochkur Approximation to $n=2$ & $n=3$ Electron-Impact Excitation of He$^+$

R Kwong * & W Williamson (Jr)

Department of Physics & Astronomy, The University of Toledo, Toledo, OH 43606

The Coulomb-Glauber-Ochkur analytic exchange amplitude is combined with the direct Coulomb-Glauber amplitude, derived by Thomas and Franco, to calculate the exchange-corrected cross-sections for the e + He$^+$ (1s) excitation processes ($n = 2$ and $n = 3$ levels). The results are compared with other theoretical predictions and with available experimental data.

1. Introduction

Electron-ion direct collision processes have continued to be of great interest to both theorists and experimentalists. The theoretical or experimental direct cross-sections are essential to the understanding of many astronomical and plasma phenomena.[1] More recently, theoretical work has been done to include electron exchange within the Coulomb-Born-Oppenheimer context[2,3] and using the Distorted-Wave-Polarized-Orbital Method.[4-6] In this paper, we report the inclusion of electron exchange in the Glauber context.

During the past decade, the Glauber approximation[7] has been extensively applied to the study of elastic and inelastic scattering of structureless charged particles by neutral atoms.[8,9] In particular, this theory has been proved to be reliable in the intermediate and high energy inelastic processes.[8,10,11] Its success within the last few years prompted a few authors to extend its application to the inelastic scattering of charged particles from hydrogen-like ions. Two groups have independently reduced the direct Coulomb-Glauber (CG) amplitude down to a one-dimensional integral, and have calculated the excitation cross-sections for the process e + He$^+$ (1s)→ e + He$^+$ (2s and 2p).[12,13] However, Thomas and Franco[10] were able to reduce the CG amplitude to an analytic form which is a simple sum of Meijer G functions. Thomas[14] has recently applied this to the $n=2$ and $n=3$ excitation of hydrogen-like ions by incident electrons for various values of the target-ion nuclear charge z. His results were in good agreement with the results mentioned above. On the whole, when these results are compared with available experimental data,[15,16] they agree very well

at higher energies but are consistently lower than the experimental results at energies above and near the inelastic threshold ($\sim$ 45→ 150 eV).[12-14] Although the CG approximation is expected to fail very close to threshold, one would hope to have better agreement between theory and experiment than has been found in the intermediate energy region. Williamson, et al.[17] investigated the effects of exchange for charged particle scattering from hydrogen-like ions. They derived a simple closed-form expression for the exchange amplitude, in the Coulomb-Glauber-Ochkur (CGO) context, which was then combined with the direct CG amplitude of Thomas and Franco, to calculate the exchange-corrected (symmetrized) cross-section for the process e$^-$ + He$^+$ (1s) → e$^-$ + He$^+$ (2s).[17] This symmetrized cross-section showed improvement over the direct Coulomb-Glauber one, when compared with the experimental results of Dolder and Peart.[15]

We have calculated the symmetrized differential and total cross-sections for the process e$^-$ − He$^+$ (1s → $n = 2, n = 3$). The direct amplitudes were calculated using the analytic expressions given by Thomas and Franco.[10] The numerical accuracy of our direct amplitudes was established by determining direct total cross-sections and comparing them with Thomas' results.[14] They were found to be in excellent agreement. The exchange amplitudes were calculated using the analytic expression given by Williamson, et al.[17] The direct and exchange amplitudes were appropriately combined to yield symmetrized post and prior differential and total cross-sections. Section 2 briefly summarizes the application of the Coulomb-Glauber-Ochkur method, and Section 3 is devoted to the presentation of our numerical results, and pertinent discussion. Section 4 sums up the usefulness of the CGO approximation for computing

*Present address : Department of Physics & Astronomy, The University of New Mexico, Abbuquerque, NM 87131

the excitation cross-sections in the light of the results of the present study.

2. Applications to e^- - He^+ Excitation Processes

Consider the scattering of electrons from a hydrogen-like ion which has z protons within the nucleus and z' bound electrons, and $z_0 = z - z'$ excess charge. Williamson et al. have shown that the CGO exchange amplitude can be reduced to a simple analytic form:[17]

$$g^\pm = \frac{-8\pi z'}{k^2} 2^{-i(\eta_{\pm z} + \eta_{\mp z_0})} \Gamma(1 - i\eta_{\pm} z)$$
$$\Gamma(1 - i\eta_{\mp} z_0)$$

$$\times \eta_+^{i\eta + z_0} \eta_-^{i\eta - z_0} C_{if} \, D_{\mu\gamma}^{\rightarrow}$$

$$\times \left\{ [\mu \pm i (\vec{q} - \vec{\gamma}) \cdot \hat{z}]^{-i\eta \mp z_0} [\mu \mp i (\vec{q} - \vec{\gamma}) \cdot \hat{z}]^{-i\eta \pm z} \right.$$

$$\times [\mu^2 + |\vec{q} - \vec{\gamma}|^2]^{i(\eta_{\pm z} + \eta_{\mp z_0}) - 1} \, {}_2F_1 \left(i\eta_{\mp} z_0, i\eta_{\mp} z; 1; \right.$$

$$\left. \left. \frac{-|(\vec{q} - \vec{\gamma}) \times \hat{z}|^2}{\mu^2 + [(\vec{q} - \vec{\gamma}) \cdot \hat{z}]^2} \right) \right\} \qquad \ldots(1)$$

where k_i (k_f) is the incoming (outgoing) electron's momentum, $\eta_+ = 1/k_i$, $\eta_- = 1/k_f$

$$\vec{q} = \vec{k}_i - \vec{k}_f$$

${}_2F_1$ is the hypergeometric function and g^+ and g^- are the post and prior exchange amplitudes respectively.

Writing the product of any two different hydrogen-like wavefunctions as

$$\phi_f^*(\vec{r}) \, \phi_i(\vec{r}) = C_{if} \left\{ D_{\mu\gamma}^{\rightarrow} \left[\frac{1}{r} e^{-\mu r - i\vec{\gamma} \cdot \vec{r}} \right] \right\}_{\vec{\gamma} = 0} \qquad \ldots(2)$$

the appropriate constant C_{if} and differential operator $D_{\mu\gamma}^{\rightarrow}$ for any electron impact excitation on a hydrogen-like ion can be found. Consequently, the exchange amplitude for that particular process can be easily obtained. The exchange amplitude for $1s \rightarrow 2s$ excitation is given in a previous paper.[17] Eq. (1) may be used to write down the exchange amplitudes for the $n=2$ and $n=3$ excitations for He^+. The particular amplitudes of interest are found to be:

$$g^{(\pm)}(1s \rightarrow 2p0) = (\mp) \sqrt{2} \, Y (a-b) \frac{M^{a-b-2}}{\mu^{a+b+2}}$$
$$\times \{ (a+b-3) \, MF(1)$$
$$+ 2q^2 (1-a)(1-b) \, F(2) \} \qquad \ldots(3a)$$

$$g^{(\pm)}(1s \rightarrow 2p\pm 1) = \mp 2i \, Y (1-a)(1-b) \, q \, e^{\mp i\phi}$$

$$\times \frac{M^{a+b-3}}{\mu^{a+b+1}} \left\{ (a+b-4) \, MF(2) \right.$$
$$\left. + q^2 (2-a)(2-b) \, F(3) \right\} \qquad \ldots(3b)$$

$$g^{(\pm)}(1s \rightarrow 3s) = \frac{1}{27\sqrt{3}z} \, Y \cdot \frac{M^{a+b-4}}{\mu^{a+b+1}} \times$$

$$\left\{ 3(a+b+5)(a+b)(a+b-2) \, M^3 \, F(1) \right.$$
$$+ 18q^2 [(a+b)^2 - 4](1-a)$$
$$(1-b) M^2 F(2)$$
$$+ 18q^4 (a+b-1)(1-a)(1-b)$$
$$(2-a)(2-b) \, M \, F(3)$$
$$+ 4q^6 (1-a)(1-b)(2-a)(2-b)$$
$$\left. (3-a)(3-b) \, F(4) \right\} \qquad \ldots(3c)$$

$$g^{(\pm)}(1s \rightarrow 3p0) = (\mp) \frac{2\sqrt{2}}{27} \, Y (a-b) \frac{M^{a+b-3}}{\mu^{a+b+2}}$$

$$\times \left\{ (a+b+4)(a+b-3) \, M^2 \, F(1) \right.$$
$$+ 2q^2 (2a+2b-1)(1-a)(1-b) \, MF(2)$$
$$\left. + 2q^4 (1-a)(1-b)(2-a)(2-b) \, F(3) \right\} \qquad \ldots(3d)$$

$$g^{(\pm)}(1s \rightarrow 3p\pm 1) = \mp \frac{4i}{81} \, Y q \, e^{\mp i\phi}(1-a)(1-b)$$

$$\frac{M^{a+b-4}}{\mu^{a+b+1}}$$

$$\times \left\{ 3(a+b-4)(a+b-3) \, M^2 \, F(2) \right.$$
$$+ 3q^2 (2a+2b-3)(2-a)$$
$$(2-b) \, M \, F(3)$$
$$\left. + 2q^4 (2-a)(2-b)(3-a)(3-b) \, F(4) \right\} \qquad \ldots(3e)$$

$$g^{(\pm)}(1s \rightarrow 3d0) = - \frac{16z}{243\sqrt{6}} \, Y \frac{M^{a+b-4}}{\mu^{a+b+3}}$$

$$\times \left\{ 3(4ab - a^2 - b^2 - a - b) \right.$$
$$(a+b-4) \, M^3 \, F(1)$$
$$+ 18q^2 (2ab - 3a - 3b + 4)$$
$$(1-a)(1-b) \, M^2 \, F(2)$$
$$+ 9q^4 (1-a)(1-b)(2-a)(2-b)$$
$$(a+b-4) \, M \, F(3)$$
$$+ 2q^6 (1-a)(1-b)(2-a)(2-b)$$
$$\left. (3-a)(3-b) \, F(4) \right\} \qquad \ldots(3f)$$

$$g^{(\pm)}(1s \rightarrow 3d\pm 1) = \mp \frac{16iz}{81} \, Y q \, (\mp) \, e^{\mp i\phi}$$
$$(a-b)(1-a)(1-b)$$

$$\times \; \frac{M^{a+b-3}}{\mu^{a+b+2}} \left\{ (a+b-5) \; M \; F \,(2) \right.$$

$$\left. + q^2 \,(2-a)\,(2-b)\,F\,(3) \right\} \qquad ...(3g)$$

$$g^{(\pm)} \,(1s \rightarrow 3d \pm 2) = -\frac{8z}{243} \; Y \; q^2 \; e^{\mp 2i\phi}$$

$$(1-a)\,(1-b)\,(2-a)\,(2-b)$$

$$\times \; \frac{M^{a+b-4}}{\mu^{a+b+1}} \left\{ 3\,(a+b-6)\;M\;F\,(3) \right.$$

$$\left. + 2q^2 \,(3-a)\,(3-b)\,F\,(4) \right\} \qquad ...(3h)$$

In the above equations,

$$F\,(N) = {}_2F_1 \left(a, b, N, -\frac{q^2}{\mu^2} \right) \text{ for } N=1,2,3 \text{ or } 4.$$

$$Y = \frac{z^4 z'}{k_i^2} \; \frac{\Gamma\,(1-a)\,\Gamma\,(1-b)}{2^{a+b}} \; \eta_+{}^{i\eta+z_0} \; \eta_-{}^{i\eta-z_0}$$

$$a = i\eta_{(\mp)} \; z_0; \; b = i\eta_{(\pm)} \; z; \; M = \mu^2 + q^2$$

$$\mu = \frac{3}{2} \; z; \text{ for } n=1 \text{ to } n=2$$

$$\mu = \frac{4}{3} \; z; \text{ for } n=1 \text{ to } n=3$$

The signs written inside brackets denoted as $(\pm)$ or $(\mp)$ are related to the post and prior exchange amplitude. These signs when not inside a bracket are related to the azimuthal quantum number of the excited state. In the above equations, the quantization axis has been chosen such that $\vec{q} \cdot \hat{z} = 0$. For He+, $z=2$, $z_0=1$ and $z'=1$.

These exchange amplitudes were numerically evaluated and combined with the CG amplitude of Thomas and France,[10] to find the exchange-corrected differential cross-section using the familiar formula:

$$\frac{d\sigma}{d\Omega} = \frac{k_f}{k_i} \left[\frac{1}{4} \left| f + g \right|^2 - \frac{3}{4} \left| f - g \right|^2 \right] \qquad ...(4)$$

The symmetrized exchange-corrected total cross-section for each process can be found by numerically integrating the differential cross-section over all solid angles, as

$$\sigma_T = \int_0^{2\pi} \frac{d\sigma}{d\Omega} \; 2\pi \sin\theta \; d\theta \qquad ...(5)$$

3. Results and Discussion

We have computed the direct amplitudes, the direct differential and total cross-sections via the formulae of Thomas and Franco.[10] Also, the exchange amplitudes in formula (3), the symmetrized differential cross-sections in (4) and the total cross-sections in (5) for the excitation of helium ions by electrons, were calculated. The excitations considered

were He ($n=1 \rightarrow 2pm, 3lm$). We will not present the numerical values for the differential cross-sections in this paper because there are no available experimental results for comparison.

3.1 $e^- - He^+$ ($1s \rightarrow 2s$) Process

In a previous paper,[17] we evaluated the CGO exchange-corrected total cross-section for the process $e^- + He^+ (1s) \rightarrow e^- + He^+ (2s)$ and compared the calculated results with the experimental absolute total cross-section. In this paper, we include the effects of cascade contributions from higher levels. Ordinarily, the observed cross-section for the aforementioned process, including cascade effects, is written as:

$$\sigma_{obs} \,(1s \rightarrow 2s) = \sigma \,(1s \rightarrow 2s) + \gamma \sigma \,(1s \rightarrow 3p)$$

where the second term on the right is the estimated theoretical cascade contributions, and γ is the cascade coefficient. Different authors[1,4,18] have used different values for γ. We shall employ the most widely used one of Hummer and Seaton[18] for our CGO computations (i.e. $\gamma = 0.23$).

Our computed CG and CGO results for $\sigma_{obs} = \sigma(1s \rightarrow 2s) + 0.23 \; \sigma \,(1s \rightarrow 3p)$, together with the experimental data of Dolder and Peart,[15] are given in Table 1. The post-prior discrepancy is prominent for low energies and becomes negligible above approximately 150 eV. At high energies, the exchange contributions to the direct cross-section become insignificant.

In Fig. 1 the CG, the CGO computed values and the experimental data are plotted as a function of the incident electron energy. Also included in the figure are the results of the distorted wave polarized orbital (DWPO II) approximation by McDowell et al.[5,6] It is seen that all three theoretical curves agree well at high energies (above 300 eV) with the measured data, which is normalized to the Born approximation at high energies. However, at intermediate and low energies above threshold, the CGO curve is in better agreement with the experimental data than the other two. It is apparent that the inclusion of exchange in the Coulomb-Glauber approximation is an improvement.

Since $\sigma \,(1s \rightarrow 3p)$ is also included in our calculation as the major cascade contribution to the $\sigma_{obs} \,(1s \rightarrow 2s)$, we can tentatively say that Fig. 1 reflects the reliability of the CGO approximation for the $e^- - He^+ (1s \rightarrow 3p)$ excitation process.

3.2 $e^- - He^+$ ($1s \rightarrow 2p$) Process

In Table 2 we present the CG and CGO results. They are shown in Fig. 2, which also shows the experimental results of Dashchenko et al.[16] The

267

Table 1—Experimental and Computed Values of σ_{obs} for the $e^- + He^+$ $(1s) \rightarrow e^- + He^+$ $(2s)$ Process Including Cascade Contributions for Various Incident Electron Energies [$\sigma_{obs} = \sigma(1s \rightarrow 2s) + 0.23\sigma(1s \rightarrow 3p)$ in Units of $10^{-3}\pi a_0^2$]

| Incident electron energy (eV)	Direct Coulomb-Glauber (CG)	Coulomb-Glauber-Ochkur (CGO)		Experimental (Dolder and Peart[15])
		Post	Prior	
53.6	6.79	11.02	9.32	12.6
58.5	7.94	11.39	10.64	12.1
78.5	10.10	10.94	11.13	10.2
100	10.56	10.28	10.42	9.1
130	10.15	9.45	9.50	8.3
200	8.40	7.77	7.77	7.1
300	6.47	6.08	6.08	5.9
400	5.23	4.98	4.98	5.3
450	4.77	4.57	4.57	5.0
500	4.39	4.22	4.22	4.6
600	3.79	3.67	3.67	3.8
680	3.42	3.32	3.32	3.5
750	3.15	3.06	3.06	3.0
850	2.83	2.76	2.76	2.8
1000	2.46	2.41	2.41	2.4
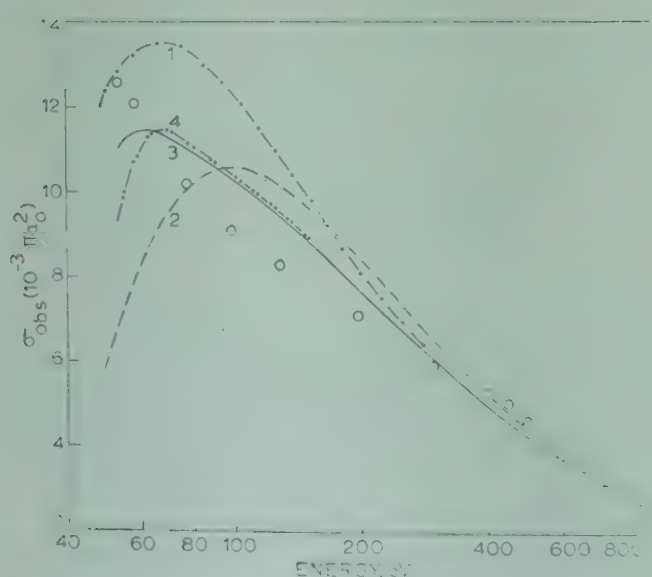
Fig. 1—Total cross-section for the $e^- + He^+$ $(1s) \rightarrow e^- + He^+$ $(2s)$ process, including cascade contributions using the formula $\sigma_{obs} = \sigma(1s \rightarrow 2s) + 0.23\sigma(1s \rightarrow 3p)$, versus incident electron energy [Curves: 1, the DWPO II approximation of Ref. 4 and 5; 2, the CG approximation evaluated using the formulas in Ref. 10; 3, the post-symmetrized CGO results of this paper; 4, the prior-symmetrized CGO results of this paper; and O, experimental points of Ref. 15.]

Coulomb-Born (CB) and the Coulomb-Born-Oppenheimer (CBO) theoretical results of Mitra and Sil are also shown.[3] Dashchenko's experimental points have been normalized to the CG results of Burgess et al.[19] at an electron energy of 217 eV and the error bars reflect 90% confidence limits on the relative measurements for energies of 100 eV or higher. Both the CBO and the CGO approximations tend to lower the value of the total cross-section calculated from CB and CG respectively at all energies. It is also seen that all four theoretical curves agree well with experiments at energies above 100 eV. Below 100 eV, none of the curves seems to agree with the measured data. Both the CG and the CGO curves go to zero at threshold because asymptotic Coulomb waves have been used in the derivation. On the contrary, the CB and CBO cross-sections are finite and non-zero at threshold because full Coulomb waves have been used.

3.3 $e^- - He^+$ $(1s \rightarrow 3s, 3p, 3d)$

In Table 3 we give the total cross-sections in both the CGO and the CG approximations at various incident electron energies for the processes $e^- + He^+$ $(1s) \rightarrow e^- + He^+$ $(3s, 3p, 3d)$. In all three excitations, it is seen that the departures of the CGO results from the CG results are more prominent at lower energies and intermediate energies. For

Table 2—Absolute Total Cross-sections (in Units of $10^{-2}\pi a_0^2$) for the $e^- + He^+$ $(1s) \rightarrow e^- + He^+$ $(2p)$ Process for Various Incident Electron Energies

Energy (eV)	Direct Coulomb-Glauber	Coulomb-Glauber-Ochkur	
		Post	Prior
54.4	6.32	5.71	6.11
61.2	7.10	6.67	6.95
68	7.57	7.19	7.40
81.6	7.94	7.61	7.75
95.2	8.07	7.70	7.78
108.8	7.99	7.63	7.68
163.2	7.20	6.95	6.96
217.6	6.43	6.22	6.22
326.4	5.23	5.12	5.12
408	4.61	4.54	4.54
544	3.88	3.83	3.83
680	3.36	3.33	3.33
979.2	2.63	2.61	2.61
1224	2.44	2.42	2.42
1632	1.76	1.76	1.76

example, at 68 eV for $1s \rightarrow 3s$ process, the post CGO result and the CG cross-section has a difference of 16·9%, at 95·2 eV a difference of 7·6% and at 680 eV only a difference of 3·8%. The overall differences between the exchange-corrected results and the direct results for the $1s \rightarrow n=3$ excitation are not
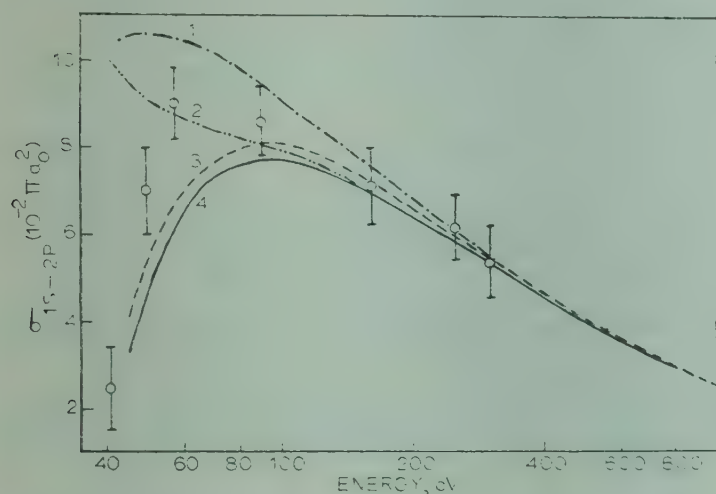
as significant as the $1s \rightarrow n=2$ excitation. A qualitative comparison of other existing theoretical results with the Coulomb-Glauber version for $1s \rightarrow n=3$ excitation can be found in a recent paper by Thomas.[14] The post and prior CGO inclusion of exchange tends to lower the CG direct cross-sections at all energies as shown in Table 3.

Fig. 2—Absolute total cross-section versus incident-energy for the $e^- + He^+ (1s) \rightarrow e^- + He^+ (2p)$ process [Curves: 1, the CB approximation of Ref. 3; 2, the CBO approximation of Ref. 3; 3, the CG approximation evaluated using the formulas in Ref. 10; and 4, the post-symmetrized CGO results of the present study and O, the experimental data points of Ref. 16.]

4. Conclusion

We have shown that the Coulomb-Glauber-Ochkur approximation provides a useful extension of the Coulomb-Glauber method for electron impact excitation on hydrogen-like ions. For the $1s \rightarrow 2s$ excitation it agrees reasonably well with the measured total cross-sections at all energies and, in particular, it shows improvement over the CG approximation relative to the experimental results in the intermediate energy region. However, for the $1s \rightarrow 2p$ transition, it seems that both the CG and the CGO methods produce good results only at energies higher than twice threshold. For the $1s \rightarrow n=3$ transition, there is at present no experimental data available for comparison.

One very interesting feature displayed by Tables 1 and 2 is that the departures of our exchange-corrected total cross-sections from the direct results

Table 3—Total Cross-sections (in Units of πa_0^2) for the $e^- + He^+ (1s) \rightarrow e^- + He^+ (n=3)$ Process for Various Incident Electron Energies

Energy	$1s \rightarrow 3s$			$1s \rightarrow 3p$			$1s \rightarrow 3d$		
(eV)	CG	CGO (PR)	CGO (PO)	CG	CGO (PR)	CGO (PO)	CG	CGO (PR)	CGO (PO)
68	0·987(−3)	0·820(−3)	0·899(−3)	0·113(−1)	0·108(−1)	0·104(−1)	0·111(−2)	0·101(−2)	0·986(−3)
81·6	0·120(−2)	0·106(−2)	0·116(−2)	0·128(−1)	0·123(−1)	0·120(−1)	0·120(−2)	0·114(−2)	0·109(−2)
95·2	0·131(−2)	0·121(−2)	0·129(−2)	0·133(−1)	0·127(−1)	0·125(−1)	0·121(−2)	0·116(−2)	0·110(−2)
108·8	0·135(−2)	0·127(−2)	0·133(−2)	0·133(−1)	0·127(−1)	0·126(−1)	0·117(−2)	0·111(−2)	0·108(−2)
136	0·132(−2)	0·125(−2)	0·128(−2)	0·130(−1)	0·123(−1)	0·123(−1)	0·109(−2)	0·102(−2)	0·101(−2)
163·2	0·124(−2)	0·117(−2)	0·119(−2)	0·123(−1)	0·117(−1)	0·117(−1)	0·983(−3)	0·923(−3)	0·923(−3)
190·4	0·115(−2)	0·109(−2)	0·110(−2)	0·116(−1)	0·111(−1)	0·111(−1)	0·899(−3)	0·848(−3)	0·846(−3)
217·6	0·107(−2)	0·100(−2)	0·101(−2)	0·110(−1)	0·106(−1)	0·105(−1)	0·818(−3)	0·776(−3)	0·778(−3)
244·8	0·987(−3)	0·927(−3)	0·932(−3)	0·104(−1)	0·100(−1)	0·100(−1)	0·754(−3)	0·718(−3)	0·717(−3)
326·4	0·794(−3)	0·751(−3)	0·753(−3)	0·892(−2)	0·868(−2)	0·868(−2)	0·603(−3)	0·580(−3)	0·579(−3)
435·2	0·627(−3)	0·595(−3)	0·596(−3)	0·754(−2)	0·739(−2)	0·739(−2)	0·472(−3)	0·458(−3)	0·458(−3)
544	0·515(−3)	0·492(−3)	0·492(−3)	0·656(−2)	0·646(−2)	0·646(−2)	0·386(−3)	0·376(−3)	0·376(−3)
612	0·463(−3)	0·444(−3)	0·494(−3)	0·608(−2)	0·600(−2)	0·600(−2)	0·346(−3)	0·338(−3)	0·338(−3)
680	0·420(−3)	0·404(−3)	0·404(−3)	0·568(−2)	0·561(−2)	0·561(−2)	0·314(−3)	0·307(−3)	0·307(−3)
816	0·354(−3)	0·342(−3)	0·342(−3)	0·502(−2)	0·497(−2)	0·497(−2)	0·263(−3)	0·259(−3)	0·259(−3)
1088	0·268(−3)	0·261(−3)	0·261(−3)	0·410(−2)	0·407(−2)	0·407(−2)	0·199(−3)	0·196(−3)	0·196(−3)
1224	0·238(−3)	0·233(−3)	0·233(−3)	0·376(−2)	0·373(−2)	0·373(−2)	0·177(−3)	0·175(−3)	0·175(−3)
1632	0·178(−3)	0·175(−3)	0·175(−3)	0·300(−2)	0·299(−2)	0·299(−2)	0·135(−3)	0·133(−3)	0·133(−3)

at most energies are far more significant for the $1s\rightarrow2s$ transition than for the $1s\rightarrow2p$ transition. This has the natural explanation that for weak transitions indirect coupling via exchange is comparatively important compared with direct coupling, while for strong optically allowed transitions, only the direct coupling is of importance. This behaviour is also seen to hold true for the $1s\rightarrow n=3$ transition, although to a lesser extent. From Table 3 we can see that the exchange contributions for both the $1s\rightarrow3s$ and $1s\rightarrow3d$ transitions are a little more significant than those for the $1s\rightarrow3p$ process.

Although some of the results in this paper indicate that the Coulomb-Glauber-Ochkur approximation is a reliable method for computing $e^- - He^+$ cross-sections, further applications of this method on other electron-hydrogen-like ion excitation processes are required before any definite conclusions should be drawn. So far, the comparisons of experimental and theoretical total cross-sections is encouraging, but comparisons of differential cross-sections would be a more rigorous test of the theory. We believe the CG and the CGO approximations are among the easiest for electron-ion cross-section computations, since both have been reduced to closed form. It is our hope that the present work will spur experimental efforts for measuring differential cross-sections for the $e^- - He^+$ excitation processes.

References

1. Seaton M J, in *Advances in atomic and molecular physics*, Vol. II, edited by Bates D R & Bederson B (Academic Press, New York), 1975, 83.
2. Das A K, Maiti N & Sil N C, *Indian J. Phys.*, B52 (1978), 83.
3. Mitra C & Sil N C, *Phys. Rev.*, A18 (1978), 1758.
4. McDowell M R C, Morgan L A & Meyerscough V P, *J. Phys.*, B6 (1973), 1435.
5. McDowell M R C, Morgan L A & Meyerscough V P, *J. Phys.*, B7 (1974), L 195.
6. McDowell M R C, Morgan L A & Meyerscough V P, *J. Phys.*, B8 (1975), 1053.
7. Glauber R J, in *Lectures in theoretical Physics*, Vol. I, edited by Brittin W E *et al.* (Interscience, New York), 1959, 315.
8. Gerjuoy E & Thomas B K, *Rep. Prog. Phys.*, 37 (1974). 1345.
9. Mohan M & Vidhani T, *Indian J. pure appl. Phys.*, 15 (1977), 662.
10. Thomas B K & Franco V, *Phys. Rev.*, A13 (1976), 2004.
11. Chan F T, Lieber M, Foster G & Williamson W (Jr), in *Advances in electronics and electron physics*, (1979) (in Press).
12. Narumi H & Tsuji A, *Prog. theor. Phys.*, 53 (1975), 671.
13. Ishihara T & Chen J C Y, *J. Phys. B* 8 (1975), L 417.
14. Thomas B K, *Phys. Rev.*, A18 (1978), 452.
15. Dolder K T & Peart B, *J. Phys.*, B 6 (1973), 2415.
16. Dashchenko A I, Zapesochnyi I P, Imre A I, Bukstick V S, Danck F F & Kel'man V A, *Soviet Phys. JETP*, 40 (1975), 249.
17. Williamson (Jr) W, Foster G & Kwong R, *Phys. Rev.*, A17 (1978), 1823.
18. Hummer D G & Seaton M J, *Phys. Rev. Lett.*, 6 (1961), 471.
19. Burgess A, Hummer D G & Tully J A, *Phil. Trans. R. Soc.*, A266 (1970), 225.

Study of Parameters of Argon Plasma by Microwave Scanning Technique

G K Sarkar, D Majumdar & D C Sarkar

Department of Physics, University of Kalyani, Kalyani 741 235

The growth and decay of argon plasma excited by modulated rf field are studied by applying phase-shift method using delayed microwave scanning technique. Microwave pulses of known width are sent through the plasma at different instants relative to rise and fall of electron density. Equations for rate of growth and decay of electron density are solved in terms of recombination coefficient, rate of generation of electrons and attachment coefficient. From observed values of ionization and deionization times, recombination coefficient and rate of generation are calculated. The rf breakdown potentials are measured in $0.1-1.0$ torr range of pressure with pure argon as also argon seeded with 10% ethyl alcohol at different frequencies (5-9 MHz).

1. Introduction

The study of radio frequency (rf) plasma has received considerable attention by many scientists.[1-3] The study enables the measurement of many important parameters of plasma. The measurement of these parameters itself has many possible applications, e.g. in radio communication over long distances, communicating through rocket exhaust and re-entry plasma sheaths during blackout.[4]

The present paper describes the measurement of rf breakdown potential of pure and seeded argon gas, electron density, ionization and deionization times, the rate of generation of electrons per unit volume of the gas and the recombination coefficient of an rf excited argon plasma. The method of measurement of electron density in the plasma is based on the measurement of phase-shift suffered by the microwave probing signal passing through the plasma. Microwave pulses of known width sent through the plasma at different instants relative to rise and fall of electron density undergo different amounts of phase-shift which in turn describe the temporal development inside the discharge tube.

2. Theory

When plasma is generated by an external electric field, the rate of growth of electron density may be represented by the following equation

$$\frac{dn}{dt} = q - \alpha n^2 - \beta n \qquad \ldots(1)$$

where α is the coefficient of electron-ion recombination; β is the attachment coefficient, q is the rate of generation of electrons per unit volume and n is the number of electrons per cc at the instant t. In Eq. (1)

we have not considered electron loss term due to diffusion. Since the electron density, in the rf excited electrodeless plasma, is of the order of 10^{10} cc^{-1} only, the diffusion factor is not predominant.

In the case of pure argon plasma, the attachment term can be neglected as inert argon has got a closed electronic shell structure.[5] Hence Eq. (1) is written in the following reduced form

$$\frac{dn}{dt} = q - \alpha n^2 \qquad \ldots(2)$$

Solutions of Eqs. (1) and (2) can be written respectively as follows

$$n = \frac{2q \tanh (\alpha q + \beta^2/4)^{1/2} (t - t_0)}{(4q\alpha + \beta^2)^{1/2} + \tanh (\alpha q + \beta^2/4)^{1/2} (t - t_0)} \cdot (3)$$

and

$$n = (q/\alpha)^{1/2} \tanh (\alpha q)^{1/2} (t - t_0) \qquad \ldots(4)$$

The modulated rf exciting field is switched on at the instant $t = t_0$. When the plama is fully developed and the electron density has attained its saturation value $[(q/\alpha)^{1/2}]$, the exciting field is switched off at instant $t = t_1$ to allow the plasma to decay. The decay of electron density is expressed as

$$\frac{dn}{dt} = -\alpha n^2 - \beta n \qquad \ldots(5)$$

In case of pure gas, this reduces to

$$\frac{dn}{dt} = -\alpha n^2 \qquad \ldots(6)$$

Solutions of Eqs. (5) and (6) may be written respectively as follows

$$n = \frac{\beta/\alpha}{[1 + \beta/(\alpha q)^{1/2}] \exp [\beta (t - t_1) - 1]} \qquad \ldots(7)$$

$$n = \frac{(q/\alpha)^{1.2}}{1 + (\alpha\, q)^{1/2}\, (t - t_1)} \qquad \ldots(8)$$

At this stage we define the ionization time as the time required by the electron density in the plasma to develop 98% of its saturation value in analogy with the charging of a condenser. Similarly the deionization time is the time required by the electron density in the plasma to decay to 2% of its saturation value. In the next section we describe an experimental method to determine the ionization and deionization times. From the knowledge of the saturation electron density and from ionization or deionization times the rate of production of electrons per unit volume and the recombination coefficient can be determined.

3. Experimental Details

3.1 Apparatus

The apparatus used is essentially a microwave interferometer[6] and a delayed microwave scanning circuit[7] as shown in the block diagram (Fig. 1). A cylindrical pyrex glass tube of dimension 25×12 cm is kept between two parallel copper plates, connected in parallel with the tank circuit of a high power negative resistance push-pull oscillator[8] so that the copper plates act as a condenser in parallel with the tank circuit. The rf oscillator of power about 500 W and having a frequency range 5-14 MHz, used for

exciting the plasma, is shown in Fig. 2. The plasma tube is filled with pure argon gas at the pressure of a few millimetres of mercury. To ensure purity of the gas, spec pure argon gas supplied by Indian Oxygen Ltd [UHP variety which may contain maximum impurities of O_2, moisture, CO_2, CO, oxides of N_2, H_2, N_2, hydrocarbons up to 4, 5, 0'5, 0'5, 0 5, 2, 10, and 0'5 ppm respectively] is used and the cylinder is flushed several times with the gas after evacuating it up to 10^{-5} mm of mercury with the help of a diffusion pump. The rf voltage is amplitude modulated by square pulse having a repetition
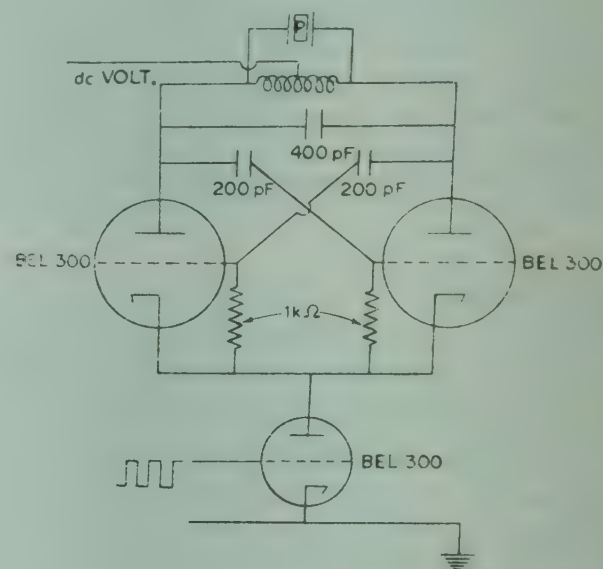

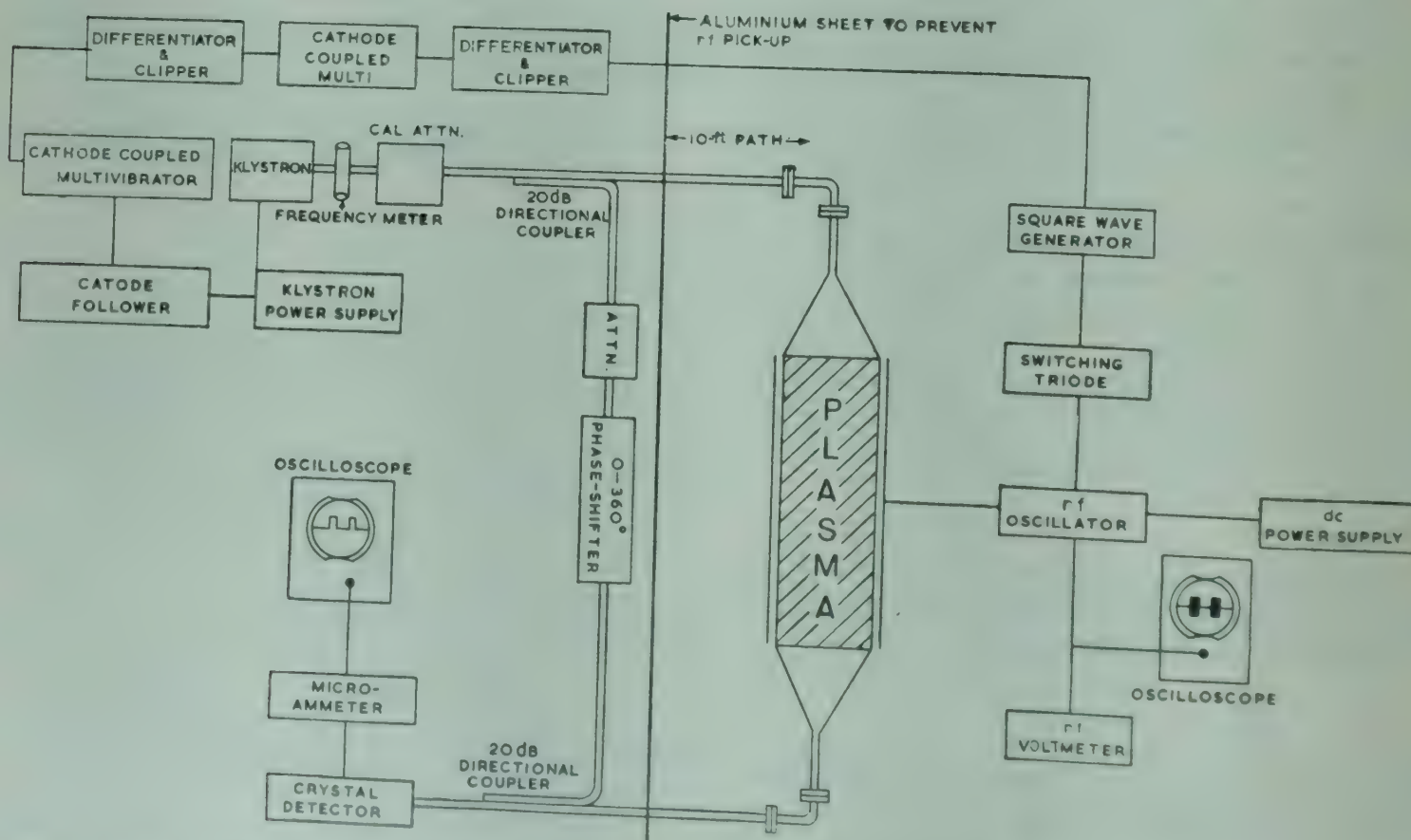Fig. 2—The rf oscillator with the switching triode

Fig. 1—Block diagram of the experimental set-up for the measurement of ionization and deionization times of rf plasma

rate of 95 Hz. The modulation is done by switching method. The arrangement is such that the oscillator remains off during the negative pulse and starts oscillation exciting the gas when there is a positive pulse. The time period of the modulating square pulse is so chosen that it is far greater than the ionization or deionization times of gases in the plasma. In this case, the time period is of the order of 10 msec whereas the ionization and deionization times are of the order of 100 μ sec.

The square pulse which modulates the oscillation is simultaneously applied to a differentiating and a clipping circuit to get sharp positive pulses having the same frequency. The pulses are then used to trigger a univibrator to get square pulses whose gate width can be adjusted to a desired value by varying the R-C combination. The square pulses are then again differentiated and clipped to get sharp negative pulses. These pulses are thus delayed by an amount equal to the gate width of the square pulse produced by the univibrator. These negative pulses are then used to trigger another univibrator the output of which is a sharp, delayed square pulse. The pulse width is measured by standard low frequency oscilloscope. The amount of the delay produced can be varied from 10 μsec to 500 μsec. This whole arrangement acts so as to produce sharp square pulses at the modulating frequency of the rf exciting field at different times. Waveforms at various points of this system are shown in Fig. 3.

The delayed pulses are then used to modulate the microwave signal from the klystron which now appears only during the period of the pulse and is passed through the plasma as a microwave probe. The rest of the microwave set-up is the usual arrangement, i e. consists of ferrite isolator, frequency meter, directional couplers, attenuators, horns, phase-shifter, etc. The main signal is passed through the plasma while a fraction of the microwave signal is passed through a phase-shifter by a 20 dB directional coupler. The signals from these two branches are then combined and detected.

In the experiments with high power rf field, one of the serious problems is the rf disturbance created in the nearby instruments. To avoid this disturbance an aluminium chamber of $1\frac{1}{2} \times 1\frac{1}{2} \times 2$ m size is made with thick aluminium sheets. All the measuring instruments together with the microwave generating units are kept inside this chamber. Only two waveguides are allowed to pass through the sheets for outgoing and incoming microwaves. Further, rf chokes at suitable places are used and all the connections are made with co-axial cables.
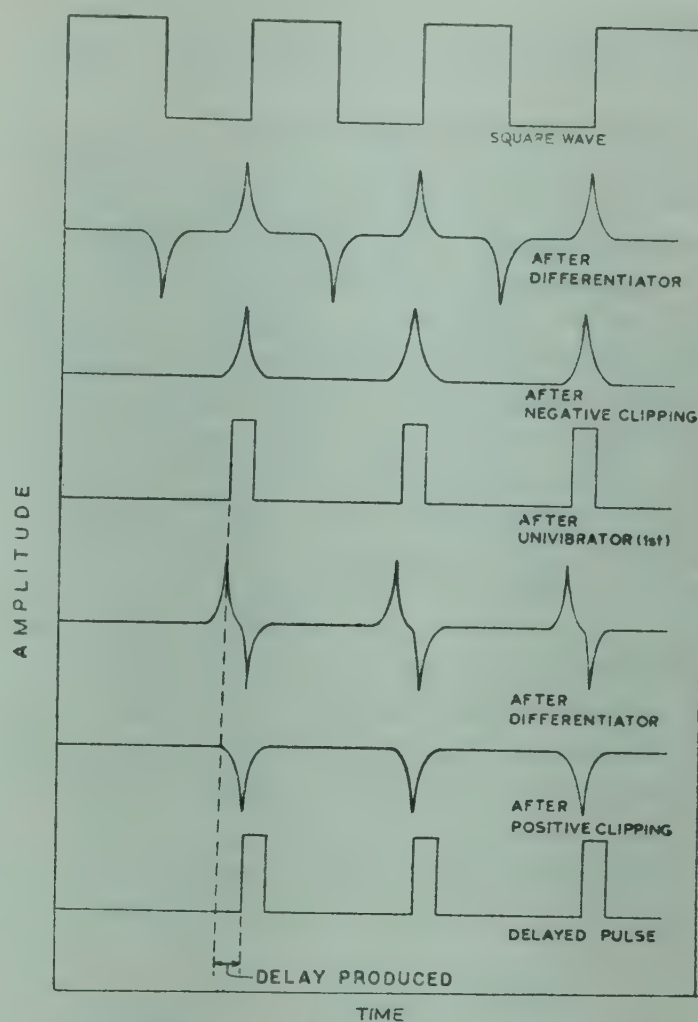
Fig. 3—Waveforms at various stages in the delayed scanning set-up

3.2 Measurement of Ionization and Deionization Times

The measurement of ionization and deionization times is virtually the measurement of the phase-shift suffered by the microwave at different instants. The sharp microwave pulses are allowed to pass through the plasma at different instants and the respective phase-shifts are measured each time. Since the phase-shift is the measure of the electron density, only the maximum phase-shift will correspond to maximum electron density and the time to develop maximum electron density (saturation value) is a measure of the ionization time. Similarly, the time of complete decay (here, the time when the phase-shift is negligible), is measured. The only necessary change in measuring the deionization time is to change the phase of the pulse by 180° so that the microwave probing signal appears when the rf oscillator is switched off and the plasma begins to decay.

The relation between the phase-shift and the electron density is given by[6]

$$\Delta\phi = \frac{\omega s}{c}\left[1 - \left(1 - \frac{n}{n_c}\right)^{1/2}\right] \qquad .. (9)$$

where $\Delta\phi$ is the phase-shift created, n_c and n are the cut-off and instantaneous electron densities, s the

273

length of the plasma, $\omega = 2\pi f$, f being frequency of the microwave signal and c the velocity of light.

3.3 Measurement of Breakdown Potential

Pure argon gas is filled in the vessel at different pressures in the range $0.1 - 1.0$ torr. The gas is excited by the rf exciting field (not modulated) and each time the breakdown potential is measured. To measure the rf voltage the rf signal from the two copper plates are connected to the vertical deflection plate of an oscilloscope which has known deflection sensitivity. A similar measurement is done by introducing 10% of ethyl alcohol into the vessel with the help of a needle valve. The percentage of the ethyl alcohol introduced is calculated from partial pressures exerted by both the argon gas and ethyl alcohol vapour. The variation of the breakdown potential with pressure in both the cases, viz. for pure and seeded argon, is shown in Fig. 4. Next the breakdown potential of argon is measured at different frequencies of the rf exciting field. It is observed that the breakdown potential is almost independent of the frequency of the rf field in the range 5-9 MHz, as shown in Fig. 5.

4. Results and Discussion

The measurements of ionization and deionization times are done in a discharge created at 1.0 torr. The phase-shift is measured by a calibrated phase-shifter (Hewlett Packard Model-X885A) and the electron density is calculated using Eq. (9), and is found to be of the order of 10^{10} electrons per cc. Figs. 6 and 7 show the growth and decay respectively of electron density with time. The ionization time comes out to be 60 μsec whereas the deionization time is 335 μsec (extrapolated). Knowing the values of instantaneous and saturation electron density, the value of recombination coefficient and the rate of generation of electrons per unit volume are calculated with the help of Eq. (4) and are shown in Table 1. The high value of recombination coefficient shows the dominant mode of dissociative recombination of Ar_2^+ ions with electrons. The
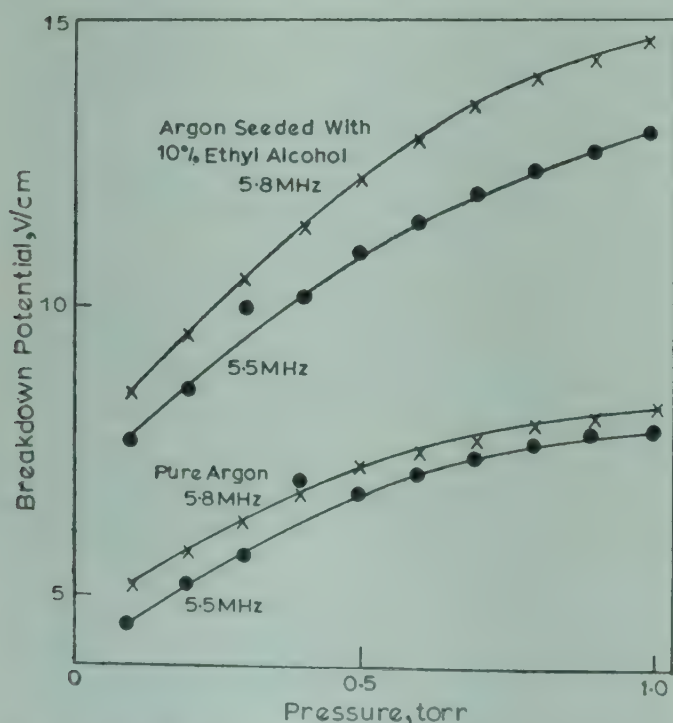
Fig. 4—Variation of breakdown potentials of (a) pure and (b) seeded (10% ethyl alcohol) argon plasma with pressure
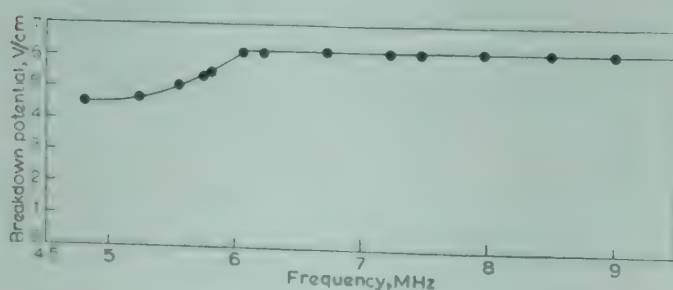
Fig. 5—Variation of breakdown potential of pure argon plasma with frequency of the rf exciting field at constant pressure
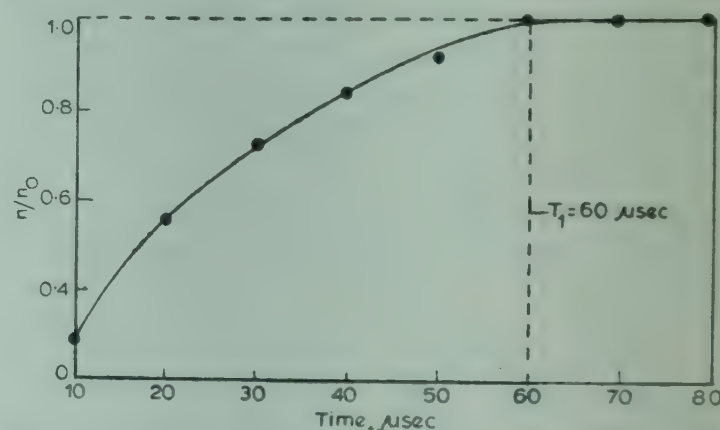
Fig. 6—Variation of ratio of instantaneous and saturated electron density (n/n_0) with time at constant pressure. (when rf exciting field is switched on at $t = t_0$)
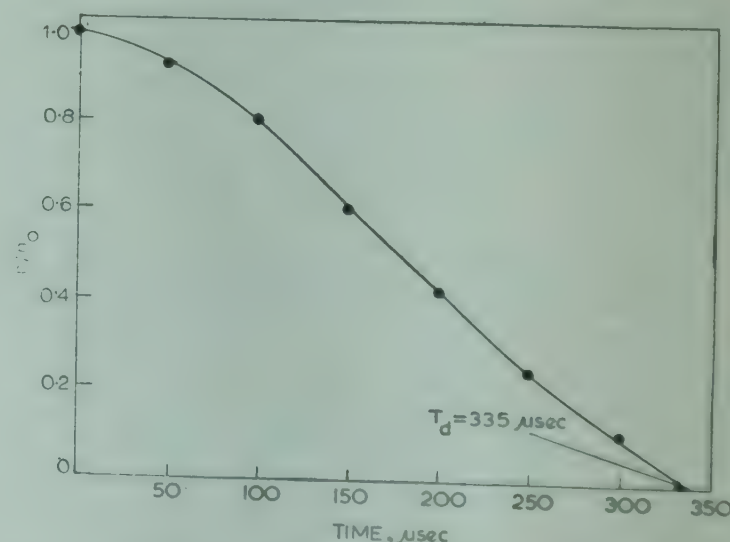
Fig. 7—Variation of ratio of instantaneous and saturated electron density (n/n_0) with time at constant pressure (when rf exciting field is made off at $t = t_0$)

Table 1—Data of Instantaneous Electron Density for Determination of Ionization Time, Deionization Time, Recombination Coefficient and Rate of Generation of Electrons/Unit Volume

Phase shift in deg.	Delay time in μ sec	Electron density (n) 10^{10}/cc	n/n_0*
With Plasma off			
14	0	1·154	1
13	50	1·072	0·926
11·4	100	0·941	0·813
8·5	150	0·702	0·607
6	200	0·496	0·429
3·5	250	0·280	0·242
1·5	300	0·129	0·112
With Plasma on			
4	10	0·330	0·286
7	20	0·646	0·558
10	30	0·825	0·715
11·6	40	0·957	0·829
12·8	50	1·056	0·915
14·0	60	1·154	1·0
14·0	70	1·154	1·0
14·0	80	1·154	1·0

Calculated (av.) value of α [$\times 10^{-6}$ cc/ ion sec; From Eq. (4)] = 2·63

Calculated (av.) value of q [$\times 10^{14}$ from Eq. (4)] = 3·32

* n_0 is the saturated value of electron density
$$= 1·154 \times 10^{10}/cc$$

present results are in good agreement with those obtained by other workers studying recombination coefficients of molecular rare-gas ions using microwave techniques.[9,10]

The variation of breakdown potential with frequency of the applied field is explained on the basis of the existence of a cut-off frequency[11] which gives a distinct limit between two breakdown mechanisms, mobility-controlled and diffusion-controlled. In a uniform electric field between parallel plates separated by a distance d, the cut-off frequency (f_c) is given by

$$f_{c_0} = \frac{k_e E_0}{\pi d}$$

where k_e is the electron mobility and E_0 is the peak value of the applied field. In the present studies, f_{c_0} lies just beyond the upper range of frequencies used here; as such, the breakdown in this case is, by and large, mobility controlled.[12] The increase in the breakdown potential in Fig. 5 ($f < 6$ Mc/s) may be due to the start of the oscillation of electrons between electrodes and onset of the diffusion breakdown mechanism. When some electrons do not reach the anode during the half period in which they are produced they will reduce the effect of the positive-ion space charge in distorting the applied field and increasing the number of ionizing collisions. Thus the applied field must be increased to account for the less effective positive ion space charge.

The increase in the breakdown voltage with seeding of the argon gas with ethyl alcohol may be ascribed to the large cross-section for electron attachment of ethyl alcohol molecules, a fact that leads to an electron loss which may be appreciable. The effect of attachment is reflected in reduction of avalanche size[11] and is believed to be responsible for relatively high breakdown voltage of some heavy electronegative gases showing electron attachment.[13]

References

1. Goldstein L, *Phys. Rev.*, **90** (1951), 151; **100** (1955), 1037.
2. Lam L & Lin S C, *J. appl. Phys.*, **28** (1957), 754.
3. John P I & Sarkar D C, *Radio Sci.*, **5** (1970), 101.
4. Sodha M S & Arora A K, *J. Phys.*, **D2** (1969), 725.
5. Massey H S W, *Negative ions* (Cambridge University Press, Cambridge), 1938, 19.
6. Heald M A & Wharton C B, *Plasma diagnostics with microwaves* (John Wiley, New York) 1965.
7. Chandra A, *Study and measurement of the parameters of a periodically varying plasma medium*, Ph D thesis, Aligarh Muslim University, Aligarh, 1972.
8. Ram V, Chandra A & Sarkar D C, *Indian J. pure appl. Phys.*, 10 (1972), 850.
9. Loeb L B, cited in *Encyclopedia of Physics*, Vol. 21—Gas Discharge 1, edited by S Flugge (Springer Verlag, Berlin), 1956, 491.
10. Oskam, H J & Mittelstadt V R, *Phys. Rev.* 132 (1963), 1445-1454.
11. Nasser E, *Fundamentals of gaseous ionization and plasma electronics* (Wiley Interscience, New York), 1971, 240.
12. Hale D H, *Phys. Rev.*, 73 (1948), 1046.
13. Schreier S, *IEEE Trans. PAS*, 83 (1964), 468.

Emission Spectra of PH⁺ & PD⁺ Molecules

P M R Rao, M N Dixit, T K Balasubramanian & N A Narasimham

Spectroscopy Division, Bhabha Atomic Research Centre, Trombay, Bombay 400 085

The rotational analysis of the $^2\Delta - {}^2\Pi$ system of the PD⁺ molecule is presented. The data on PD⁺ and the earlier data on PH⁺ are fitted to James expressions for doublet states and the molecular parameters are rederived.

1. Introduction

The spectrum of the PH⁺ molecule was reported for the first time by Narasimham[1] in 1957 and that of the isotopic molecule PD⁺ by Narasimham and Dixit[2] in 1967. Three red-degraded bands in the region 3500-4500 Å were analyzed to be the 1-0, 0-0 and 0-1 bands of a system involving a transition $^2\Delta - X^2\Pi$ of these molecules. The details of the vibrational and rotational analysis of the bands of PH⁺ molecule have been published but only a brief note on the spectrum of PD⁺ spectrum has been published. In these studies, the rotational constants were calculated by employing the equations of Hill-van Vleck and of Mulliken and Christy.[3] Since now the Hill-van Vleck expressions have been subjected to modification notably by James,[4] the authors thought it worthwhile to fit the experimental data on the PH⁺ as well as PD⁺ molecule to James equations, and recalculate the constants for these molecules.

The details of the rotational analysis of the 0-0 band of the PD⁺ molecule (hitherto unpublished), and the results of the recalculated constants for PH⁺ and PD⁺ molecule employing James expressions are presented in this paper.

2. Experimental Details

The spectrum of PH⁺ molecule was obtained in a hollow-cathode discharge with helium containing trace amount of phosphorus and hydrogen flowing at 2-3 mm pressure, and recorded at a dispersion of 0·35 Å/mm. The PD⁺ spectrum was excited employing a sealed tube technique, where helium with trace deuterium was sealed at 2-3 mm pressure in a quartz tube containing a small amount of phosphorus. The tube was excited by microwave discharge (2450 MHz). The spectrum was recorded at a dispersion of 0·56 Å/mm. The spectra were measured against iron hollow-cathode lines, and thorium lines as wave-length standards and the vacuum wavenumbers of the lines were computed. The accuracy of the measurement of the unblended lines is $\pm$ 0·04 cm⁻¹.

## 3. Results and Discussion

3.1 Descriptions of the Bands of PH⁺ and PD⁺ Molecules

The bands of PH⁺ and PD⁺ are shaded towards longer wavelength and are quite open structured, a feature typical of all hydrides. The bands are completely resolved and clearly show the branch structure up to first lines. The bands around 3800 Å are the most intense, and the isotopic band shows the minimum shift in this case. Hence these are assigned the vibrational numbering 0-0. The other bands around 3500 Å and 4200 Å show shift in opposite directions, and are assigned as 1-0 and 0-1 bands respectively of the system. The bands show double headedness typical of doublet transitions, and the two sub-bands are separated by 295 cm⁻¹. Each of the sub-bands contains 12 branches which form six close pairs of Λ doublets. For the sub-band on the higher frequency side the Λ doubling is observable from the very first member of the branch whereas in the sub-band on the lower frequency side the branches split only after $J = 13\cdot5$. The presence of the large Λ doubling shows that one of the states involved must be a $^2\Pi$ state, and that the sub-band on the higher frequency side involves the $^2\pi_{1/2}$ state. Two pairs of branches in each sub-band are strong Q branches showing that the transition has $\Delta\Lambda = \pm 1$. The presence of 12 main and satellite branches in each sub-band, and the first lines of the branches lead to assigning the transition as $^2\Delta (b) - {}^2\Pi_r (a)$ without any ambiguity.

Fig. 1 shows the rotational structure of the 0-0 band of PD⁺ molecule. The vacuum wavenumbers of the lines and their J assignments are listed in Table. 1
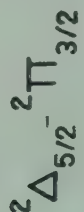
Fig. 1—Rotational Structure of 0-0 band of PD+ molecule

Table 1—Vacuum Wavenumbers of the Lines of the 0-0 Band of PD⁺

$^2\Delta_{3/2} - {}^2\Pi_{1/2}$

J	$^SR_{21}$	R_1	$^RQ_{21}$	Q_1	$^QP_{21}$	P_1
0·5						
1·5				26059·50	26056·98	
2·5		26081·16		59·25	56·53	
				51·26	49·21	
3·5	26114·37	80·23	26078·16	50·78	48·88	
		79·76		41·73	40·08	
4·5	20·02	78·16	76·50	41·12	39·54	
	19·37	77·34	75·89	30·91	29·46	25994·75
5·5	23·70	74·39	72·98	30·33	28·79	
	23·04	73·74	72·31	18·85	17·47	75·41
6·5	26·03	69·49	68·12	18·09	16·75	74·66
	25·26	68·76	67·37	05·44	04·03	54·75
7·5	26·80	63·28	61·88	04·62	03·21	53·98
	26·03	62·48	61·04	25990·73	25989·29	32·90
8·5	25·26	55·64	54·26	89·81	88·46	31·97
		54·77	53·37	25974·66	25973·31	25909·72
9·5	26124·29	26046·70	26045·26	73·66	72·26	08·70
	23·31	45·65	44·22	57·22	55·77	25885·20
10·5	20·87	36·30	34·77	56·15	54·75	84·09
	19·67	35·24	33·69	38·39	36·85	59·32
11·5	15·92	24·48	22·87	37·24	35·71	38·13
		23·32	21·77	18·18		32·16
12·5	09·34	11·17	09·57	16·97		30·98
	08·22	10·02	08·53	25896·49		03·49
13·5		25996·40	25994·74	95·20	25894·97	02·18
		95·07	93·45	73·45	93·64	25773·41
14·5		80·21	78·77	72·11	71·70	72·35
		78·81	77·12	48·79	70·37	41·97
15·5		62·38	60·45	47·25	47·02	40·70
		61·06	59·23	22·73	45·50	09·25
16·5		42·95	41·17	21·33		
		41·62	39·59	25795·13		
17·5		22·09				
		20·71				

$(^2\Delta_{5/2} - {}^2\pi_{3/2})$

J	R_2	$^QR_{12}$	Q_2	$^PQ_{12}$	P_2	$^QP_{12}$
0·5						
1·5						
2·5	25820·17	25792·79		25771·21		
3·5	25·61	90·87	25789·27	61·92		25740·28
4·5	29·41	87·38	85·89	51·17		22·17
5·5	31·61	82·33	80·92	38·88	25737·43	02·65
6·5	32·16	75·68	74·32	25·06	23·63	81·63
7·5	30·98	67·50	66·15	09·67		59·14
8·5	28·26	57·70	56·27	25692·73	25691·33	34·92
9·5	23·86	46·26	44·78	74·23	72·80	09·20
10·5	17·74	33·14	31·74	54·12	52·66	25682·06
11·5	09·91	18·49	16·96	32·34	30·93	53·30
12·5	00·58	02·27	00·65	09·20	07·62	23·04
			00·45			
13·5		25684·42	25682·60	25584·39	25582·78	
		83·97	82·37	84·06		
14·5			62·94	57·91	56·20	
			62·56	57·52	55·86	
15·5			41·52	29·79	28·05	
			41·00	29·24	27·54	
16·5			18·36	25499·96	98·20	
			17·80	99·37	97·56	
17·5			25593·40	68·45	66·64	
			92·82	67·91	65·96	
18·5			66·71			
			66·04			
19·5			38·28			
			37·46			

3.2 Determination of the Rotational Constants

The main theme of the present work relates to fitting the data on PH⁺ and PD⁺ to the improved doublet state term value expressions due to James[4] and Klynning *et al.*[5] We therefore, discuss these refinements over the earlier Hill-van Vleck theory and the background material in some detail. The rotational terms of the levels of a degenerate doublet state with coupling intermediate between Hund's cases (a) and (b) were first worked out in 1928 by Hill-van Vleck and are given by

$$F_1 (J) = B_v \{(J+\tfrac{1}{2})^2 - \Lambda^2\} - \tfrac{1}{2} \{A (A-4 B_v)\Lambda^2$$
$$+ 4 B_v^2 (J+\tfrac{1}{2})^2\}^{1/2} - D_v (J)^4 \quad ...(1)$$

$$F_2 (J) = B_v \{(J+\tfrac{1}{2})^2 - \Lambda^2\} + \tfrac{1}{2} \{A (A-4 B_v) \Lambda^2$$
$$+ 4 B_v^2 (J+\tfrac{1}{2})^2\}^{1/2} - D_v (J+1)^4$$
$$...(2)$$

These expressions ignore the Λ doubling of the J levels but otherwise hold for any degree of spin-uncoupling, the only limitations being:

(a) The centrifugal distortion terms in D_v have been added arbitrarily so as to conform to their correct case (b) limits.

(b) The spin-orbit coupling constant A has been treated as a constant, while owing to centrifugal distortion a slight J-dependence on A is expected.

These limitations first became apparent when the above expressions were applied to doublet states in light molecules, especially the hydrides.

Almy and Horsfall[6] removed limitation (a) by incorporating into the Hill-van Vleck theory, the effect of centrifugal distortion rigorously, following a procedure first adopted by Gilbert[7] for triplet states. Limitation (b) was first pointed out by Ramsay[8]; to remove it, James[4] suggested that the parameter A appearing in Eqs. (1) and (2) and treated as a constant in the original theory, should be replaced by the J-dependent function

$$A = A_v + A_J \left(J + \frac{1}{2}\right)^2 \quad ...(3)$$

The first term A_v in Eq. (3) is the coupling constant for zero rotation while the second term describes the effect of centrifugal distortion on A. These two modifications, discussed in detail by James, proved adequate to describe all the well studied $^2\Pi$ states of many molecules. James, however, treated only the case of $^2\Pi$ states. His procedure was extended to other doublet states by Klynning *et al.*[5] With these modifications the rotational terms of a $^2\Delta$ ($\Lambda \neq 0$) state are given by (neglecting Λ-doubling

$$\left.\begin{array}{c} F_1 (J) \\ F_2 (J) \end{array}\right\} = B_v \{(J+\tfrac{1}{2})^2 - \Lambda^2\} - D_v (J+\tfrac{1}{2})^4 \mp f (J)$$
$$...(4)$$

with

$$f (J) = \tfrac{1}{2} \{\Lambda^2 A_v (A_v - 4 B_v) + 4 \widetilde{B_v}^2 (J+\tfrac{1}{2})^2$$
$$- (16 B_v D_v - \Lambda^2 A_J^2) (J+\tfrac{1}{2})^4\}^{1/2}$$

and

$$4 \widetilde{B_v}^2 = 4 B_v^2 + 2 \Lambda^2 A_J (A_v - 4 B_v) \quad ...(5)$$

These equations have been employed for the calculation of the constants of the states involved.
Determination of B_v and D_v—Procedure for calculation of B_v and D_v remains the same as these have been done by employing $\Delta_1 F (J)$ and $\Delta_2 F (J)$ by choosing suitable combination of branches as indicated by Narasimham.[1] Averages of $\Delta_1 F_1$ and $\Delta_1 F_2$ and also of $\Delta_2 F_1$ and $\Delta_2 F_2$ were used in a standard graphical way to determine the constants.
Determination of the spin orbit coupling constant A_v, A_J, a_J, etc.—From Eqs. (4) and (5) we get

$$\Delta \nu_{21}^2 = \{F_2 (J) - F_2 (J)\}^2 = \Lambda^2 A_v (A_v - 4 B_v)$$
$$+ 4 \widetilde{B}^2 (J+\tfrac{1}{2})^2 - (16 B_v D_v - \Lambda^2 A_J^2)(J+\tfrac{1}{2})^4$$

$\Delta_{\nu 21} = [F_2 (J) - F_1 (J)]$ can be obtained by suitably combining the branches (Narasimham[1]). A_J is usually small and hence the term in A_J^2 occurring in the coefficients of $\left(J+\dfrac{1}{2}\right)^4$ can be neglected. Plotting $\Delta_{\nu 21}^2 + 16 B_v D_v \left(J+\dfrac{1}{2}\right)^4$ against $\left(J+\dfrac{1}{2}\right)^2$ yields a straight line whose slope gives $4 \widetilde{B}^2$ which is connected to A_J by Eq. (5).

The intercept will give $A_v (A_v - 4B_v)$ from which A_v can be solved. Narasimham has earlier proved that both $^2\Delta$ and $^2\Pi$ states are regular. Hence the positive values for A_v have been chosen for the

Table 2—Constants (in cm⁻¹) for the $^2\Delta$ and the $^2\pi$ States of PH⁺ and PD⁺ Molecules

State	v	B_v	$D_v (\times 10^{-5})$	A_v	$A_J (\times 10^{-2})$	$a_J (\times 10^{-5})$
			(a) Molecule: PH⁺			
$^2\Delta$	0	6·983₅	6·28	1·022	6·023	5·112
	1	6·558₈	6·20	1·115	3·572	2·017
$^2\Pi$	0	8·385₁	4·16	295·95	0·720	—
	1	8·145₉	4·0	296·29	0·569	—
		Band origins				
		ν_{1-0}	27206·55			
		ν_{0-0}	25810·78			
		ν_{0-1}	23511·20			
		(b) Molecule: PD⁺				
$^2\Delta$	0	3·635₀	1·71	1·184	3·973	7·564₆
$^2\Pi$	0	4·350₅	1·116	295·83	0·235	—
		Band origin				
		$\nu_{0-0} = 25942·20$				

states, for both PH⁺ and PD⁺ molecules. In the case of the $^2\Delta$ state, the above graph remained straight for the major part, but deviated for higher Js, indicating the necessity of a term $a_J (J+\frac{1}{2})^4$ in Eq. (3). In view of this, we now write

$$A = A_v + A_J (J+\tfrac{1}{2})^2 + a_J (J+\tfrac{1}{2})^4 \qquad \ldots(6)$$

By the usual procedure of computation the term a_J has been determined. For the Π^2 state of the PH⁺ and PD⁺ molecules, a_J was found to be too small to be determined.

Λ-doubling and band origins have been calculated for the PH⁺ and PD⁺ bands following the procedure given by Narasimham.[1]

All these constants are tabulated in Table 2.

4. Pre-dissociation in $^2\Delta$ State

Pre-dissociation of the rotational levels at $N \geqslant 13$ for F_1 levels and $N \geqslant 15$ for F_2 levels of $^2\Delta$ state has been found for PH⁺ molecule and a corresponding sudden change in intensity is observed for rotational levels at $N \geqslant 17$ of $v = 0$ level of $^2\Delta$ state of the PD⁺ molecule. Because of the lack of sufficient data, it has not been possible to conclude anything regarding the nature of the perturbation.

References

1. Narasimham N A, *Can. J. Phys.*, **35** (1957), 901.
2. Narasimham N A & Dixit M N, *Curr. Sci.*, **36** (1967), 1.
3. Mulliken R S & Christy A, *Phys. Rev.*. **38** (1931), 87.
4. James T C, *J. chem. Phys.*, **41** (1964), 631.
5. Klynning L, Lindgreen B & Aslund N, *Ark. Fys.*, **30** (1965), 141.
6. Almy G M & Horsfall R B, *Phys. Rev.*, **51** (1937), 491.
7. Gilbert C, *Phys. Rev.*, **49** (1936), 619.
8. Ramsay D A, *J. phys. Chem.*, **20** (1952), 1920.

Infrared Absorption Spectra of 2-Amino-p-Cresol & 2-Amino-4-Chlorophenol

R K GOEL, (Smt) S SHARMA & K P KANSAL*

Department of Physics, D N College, Meerut 250 002

and

S N SHARMA

Analytical Physics Section, Indian Institute of Petroleum, Dehra Dun 248 005

The infrared absorption spectra of 2-amino-p-cresol and 2-amino-4-chlorophenol have been recorded on Perkin-Elmer spectrophotometer model-521 in the region 250-4000 cm^{-1} in KBr pellet, Nujol mull and in CHCl$_3$ solution. The spectra have been analyzed assuming C_s point group symmetry and a tentative assignment of the observed bands to different fundamental modes has been made. A correlation of the observed fundamentals in different phases has also been made.

1. Introduction

The vibrational spectra of phenol,[1-3] toluene[4,5] and aniline[6,7] have been studied extensively. The vibrational spectra of aminophenol have been studied by Verma and Rai[8] and those of cresols by Green[9] and Jakobsen[10] and that of 6-amino-m-cresol by Goel *et al.*[11] In order to extend this study, the work on the infrared absorption spectra of 2-amino-p-cresol and 2-amino-4-chlorophenol have been undertaken presently. Moreover, in order to check the assignments of C—Cl, C—H, C—OH, stretching frequencies, etc. and looking for any frequency shift, the spectra have also been studied in CHCl$_3$ solution in addition to solid phase (KBr and Nujol mull) spectra.

2. Experimental Details

The chemicals, obtained from M/s Fluka A G, Switzerland, were used as such without further purification. The infrared absorption spectra of 2-amino-p-cresol and 2-amino-4-chlorophenol (hereafter referred as 2-(ApC) and 2,4-ACP respectively) were recorded on Perkin-Elmer spectrophotometer model-521 in the region 250-4000 cm^{-1} in KBr pellet, Nujol mull and in chloroform solution. The frequencies have been calibrated by drawing an error graph.

3. Results and Discussion

The infrared absorption spectra of 2 (ApC) and 2, 4-ACP in solid phase (KBr and Nujol mull) and in CHCl$_3$ solution are shown in Fig. 1. The corrected

*Department of Physics, S S V College, Hapur (UP)

wavenumbers of the observed bands together with their probable assignments are presented in Table 1.

Assuming OH, NH$_2$ and CH$_3$ groups as single mass points, the molecules undertaken at present would belong to C_s point group symmetry. Under reduced symmetry C_s, the 30 normal modes of vibration are distributed into 21 planar and 9 non-planar. In addition to these there would appear additional vibrations also, 18 in the case of 2-ApC and 9 in the case of 2, 4-ACP due to substituents groups referred above. All these vibrations are allowed in both, the infrared and the Raman spectra. The vibrational assignments have been made essentially on the basis of magnitudes and relative intensities of the observed infrared bands and the data available for similar molecules. The infrared absorption spectra of the title compounds are discussed here under two heads: (1) *Skeleton Vibration*, i.e. Vibrations associated with the ring and (2) *Group Vibrations* due to substituent groups.

3.1 Skeleton Vibration

The molecules under investigation are tri-substituted benzenes and thus there are only three hydrogen atoms left around the ring which should give rise to three C—H valence oscillations. These vibrations lie in the region 3000-3100 cm^{-1}.[12] Out of the three, only two at 3094 and 3014 cm^{-1} in 2-ApC and only one at 3104 cm^{-1} in 2, 4-ACP have been observed.

The appearance of a group of four bands between 1650-1400 cm^{-1} in the spectra of substituted benzenes represent the characteristic skeletal stretching modes.[13] The two doubly degenerate vibrations of
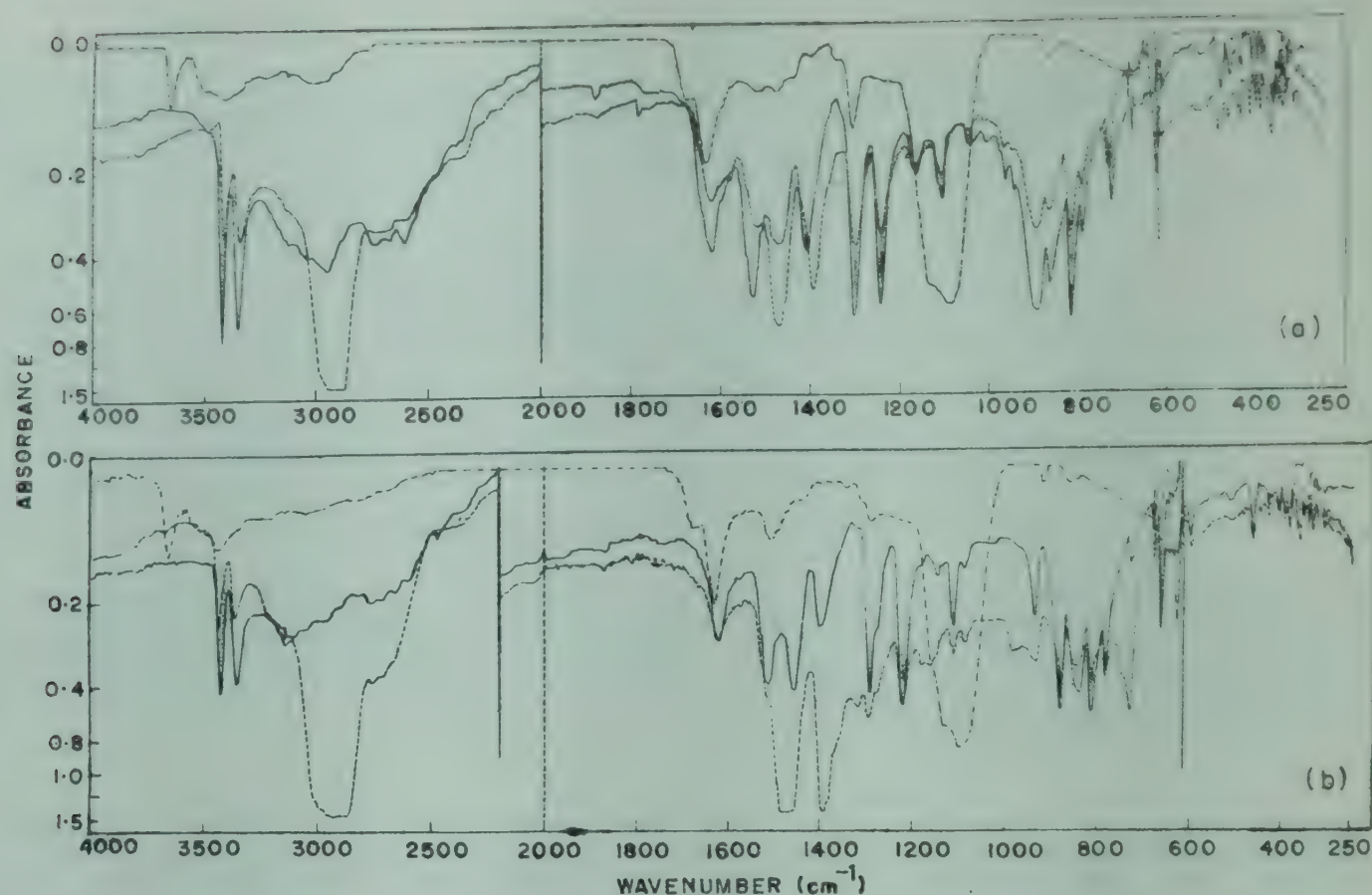
Fig. 1—Infrared absorption spectra of (a) 2-ApC and (b) 2,4-ACP [Recording phase——in KBr;— —in nujol mull; ... in CHCl$_3$]

benzene e_{2g} (1595) and e_{1u} (1485) and two non-degenerate modes b_{2u} (1310) and a_{1g} (995) have been attributed to C—C stretching vibrations. Except for the ring breathing mode of benzene (995), all these remain practically unaffected by substitution. Further under reduced symmetry C_s, the doubly degenerate frequencies split up into two distinct frequencies in substituted benzenes. Thus four bands observed at 1596, 1571, 1501, and 1457 cm^{-1} in 2-ApC and at 1596, 1571, 1491 and 1447 cm^{-1} in 2, 4-ACP have been assigned to correspond to the components of e_{2g} and e_{1u} modes. These assignments are in agreement with the assignments made by earlier workers.[8,11,14] The band observed at 1307 cm^{-1} in 2, 4-ACP corresponds to b_{2u} (1310) mode of benzene.

Under reduced symmetry C_s, the C—C ring breathing a_{1g} (995) and C—C—C trigonal bending b_{1u} (1010) vibrations of benzene give rise to combined modes.[5,14,15] As a result of their interaction, one of the modified modes reduce to about 800 cm^{-1} and the other keeps itself around 1000 cm^{-1} in tri-substituted benzenes.[13] The bands observed at 992, 972 cm^{-1} and at 802, 802 cm^{-1} have thus been assigned to C—C—C trigonal bending and C—C ring breathing vibrations in the two molecules respectively.

For molecules under present study, an appreciable mixing of ν (C—OH), ν (C—NH$_2$) and b_{2u} (1310)

mode of benzene takes place due to near equality of these vibrations. As a result of this the bands observed at 1287 cm^{-1} in 2-ApC and 1279 in 2, 4-ACP have been assigned to these modes. However, in case of 2, 4-ACP, a weak band also appears at 1307 cm^{-1} which may be attributed to b_{2u} (1310) mode in this case. The ν (C—OH) assignments are also in agreement to the assignments made by Pandey and Singh[16] in case of trichlorophenols, while the ν (C—NH$_2$) assignment find support from Tripathi et al.[17] and Sharma and Dwivedi.[18]

The doubly degenerate e_{2g} (608) vibration of benzene corresponds to C—C planar ring deformation mode. Under reduced symmetry, it splits into two components. The pair of bands at 667, 467 cm^{-1} in 2-ApC and at 665, 473 cm^{-1} in 2,4-ACP have been assigned to this mode. Similarly the pair of bands at 447, 417 cm^{-1} and at 452, 417 cm^{-1} in the two molecules respectively have been assigned to e_{2u} (404) mode of benzene. These assignments find support from literature values.[11,16]

The studies on the spectra of toluene and substituted toluenes[5,19] and 6-amino-m-cresol[11] show that there appears a strong band around 1200 cm^{-1} which correspond to C—CH$_3$ valence oscillation. Thus the band observed at 1147 cm^{-1} in 2-ApC has been assigned to this mode.

Table 1—Assignments of Fundamental Vibrational Frequencies of 2-Amino-*p*-Cresol & 2-Amino-4-Chlorophenol*
(All Values in cm⁻¹)

2-ApC in			2,4-ACP in			Assignment
KBr	Nujol mull	CHCl₃	KBr	Nujol mull	CHCl₃	
		3629(vs)			3609(vs)	ν(O—H)
3384(vvs)	3379(vs)	3369(sb)	3389(vvs)	3399(vs)	3399(sb)	ν(N—H) asym.
3314(s)	3304(vs)		3314(vs)	3324(vs)		ν(N—H) sym.
3094(vw)	3104(vw)		3104(m)	3104(vw)		ν(C—H) Aromatic
3014(vw)						ν(C—H) Aromatic
2914(ms)	2914(sb)					ν(C—H) asym. in methyl group
2849(w)	2844(sb)					ν(C—H) sym. in methyl group
1596(vs)	1594(vs)	1614(vs)	1596(vs)	1601(vs)	1614(vs)	ν(C—C), NH₂ scissoring
1571(vw)	1571(vw)		1571(vw)	1566(vvw)		ν(C—C)
1501(vs)	1501(w)	1499(mwb)	1491(s)		1495(sb)	ν(C—C)
1457(sb)	1457(vvs)	1465(mw)				ν(C—C), C—H asym. bending in methyl graup.
			1447(sb)	1457(vsb)		ν(C—C)
1392(vs)	1379(vvs)					(C—H) sym. bending in methyl group.
			1387(vs)	1379(vs)		
			1307(vw)	1307(ms)		
						ν(C—C)
1287(vvs)	1287(vs)	1295(vs)	1279(vvs)	1282(s)	1280(ms)	ν(C—OH), ν(C—NH₂)
1227(vs)	1227(s)		1207(vs)	1207(vs)		β(O—H)
				1167(m)		β(C—H) Aromatic
1147(s)	1147(ms)					ν(C—CH₃)
			1132(mb)	1147(m)		β(C—H)
1092(s)	1087(ms)		1097(s)	1097(ms)		NH₂ twisting
1027(mb)	1027(m)					CH₃ rocking
992(m)	992(m)			972(m)		β(C—C—C) trigonal bending
947(ms)						?
927(ms)	927(w)		922(s)	920(ms)		γ(C—H)
877(s)	877(sb)		867(vs)	867(sb)		γ(C—H)
847(s)	849(ms)	857(ms)	827(sb)	832(sb)	845(mb)	γ(C—H)
802(vs)	801(vs)		802(vs)	802(vs)		ν(C—C) ring breathing
777(s)	777(s)		772(s)	772(ms)		NH₂ wagging
712(vs)	715(s)		715(s)	717(s)		γ(O—H), γ(C—C)
667(s)	667(ms)		665(ms)	667(ms)		β(C—C)
			649(vs)	652(s)	657(sb)	ν(C—Cl)
595(ms)	597(m)		585(ms)	585(m)		β(C—OH)
467(s)	467(ms)		473(vw)	472(w)		β(C—C)
447(ms)	447(ms)	445(w)	452(ms)	452(s)		γ(C—C)
422(w)	427(vw)					β(C—CH₃)
417(vw)	419(m)		417(vw)	417(w)		γ(C—C)
397(m)	397(m)		395(m)	397(m)		β(C—NH₂)
349(s)	351(s)					γ(C—CH₃)
			349(ms)	349(ms)		β(C—Cl)
325(m)	326(w)	325(w)	322(w)	325(m)	325(w)	γ(C—NH₂)
312(vw)	313(w)	315(vw)	312(vw)	312(w)	315(vw)	γ(C—OH)

*Intensities are shown in parentheses against each wavenumber s = strong, vs = very strong vvs = very very strong, b = broad, m = medium, mw = medium weak, ms = medium strong, w = weak, vw = very weak, ν = stretching, β = in-plane bending, γ = out-of-plane bending

Many workers have assigned the C—Cl stretching mode in the region 550-750. The strong band observed at 649 cm^{-1} in 2, 4-ACP has been assigned to C—Cl stretching mode which finds support from earlier studies.[11,16] Attempts were also made to check this assignment by taking the spectra in solution and looking for any frequency shift as has been done by Nabumi Oi and Coetzee.[20] The strong band observed at 657 cm^{-1} in CHCl$_3$ solution in case of 2, 4-ACP and the absence of any band in the 2-ApC in this region supports the C—Cl stretching assignment. However, the evidence is not conclusive for any frequency shift, etc.

3.2 Group Vibrations

The O—H stretching mode lie in the region 3500-3600 cm^{-1}. Tripathi and Ram[21] have assigned this mode between 3540-3590 cm^{-1} in 2,3-; 2,4-; 2,5-; 2,6;- 3,4- and 3,5-dichlorophenols. Dwivedi et al.[22] have also assigned this mode at 3540 and 3530 cm^{-1} in 2,4- and 2,6-dibromophenols respectively. In view of these assignments, the very strong bands observed in chloroform solution spectra at 3629 and 3609 cm^{-1} in 2-ApC and 2,4 ACP respectively have been assigned to this mode.

In most of the primary aromatic amines, there appears two bands[12] in the region 3350-3550 cm^{-1} which are associated with N—H stretching vibrations. The bands observed at 3384 and 3389 cm^{-1} in 2-ApC and 2,4-ACP have been attributed to N—H asymmetric stretching mode while those at 3314 and 3314 cm^{-1} in the two molecules respectively to N—H symmetric stretching mode.

Three C—H stretching frequencies due to CH$_3$ group lie in the region 2962-2872 cm^{-1}.[12] Only two bands observed at 2914 and 2849 cm^{-1} in 2-ApC have been assigned to this mode. In CH$_3$ group, there are three CH$_3$ deformation frequencies, two asymmetric vibrations observed in the region 1430-1470 cm^{-1} and one symmetric vibration observed near 1370 cm^{-1}. This region of the spectrum is fairly complex because of the presence of two components of 1485 cm^{-1} (e_{1u}) C—C stretching vibration of benzene. The bands observed at 1392 and 1457 cm^{-1} in 2-ApC have been assigned to C—H symmetric and asymmetric bending vibrations respectively.

However, the latter band may also correspond to the lower component of e_{1u} (1485) mode of benzene. This finds support from the work of Mooney,[23] and Sharma and Dwivedi.[24]

References

1. Green J H S, J. chem. Soc., (1961), 2236.
2. Evans J C, Spectrochim. Acta, 16 (1960), 1382.
3. Bist H D, Brand J C D & Williams D R, J. molec. Spectrosc., 24 (1967), 402.
4. Pitzer K S & Scott D W, J. Am. Chem. Soc., 65 (1943), 803.
5. Wilmshurst J K & Bernstein H J, Can. J. Chem., 35 (1957), 911.
6. Evans J C, Spectrochim. Acta, 16 (1960), 428.
7. Flett M S T C, Trans. Faraday Soc., 44 (1948), 767.
8. Verma V N & Rai D K, Appl. Spectrosc., 24 (1970), 445.
9. Green J H S, Chem. Ind., (1962), 1975.
10. Jakobsen R J, Spectrochim. Acta, 21 (1965), 433.
11. Goel R K, Kansal K P & Sharma S N, Indian J. pure appl. Phys., 17 (1979), 778.
12. Bellamy L J, The infrared spectra of complex molecules (Chapman & Hall, London), 1975.
13. Randle R R & Whifen D H, Molec. Spectrosc., (Institute of Petroleum, London), 1955, 111.
14. Padhye M R & Viladkar B G, J. scient. ind. Res., 18B (1959), 45.
15. Randle R R & Whiffen D H, Proc. of Symp. on Molec. Spectrosc., (Institute of Petroleum, London) Vol. III, 1954.
16. Pandey S M & Singh S J, Indian J. Phys., 48 (1974), 961.
17. Tripathi G N R, Tewari B N & Verma R M, Indian J. pure appl. Phys., 13 (1975), 608.
18. Sharma S N & Dwivedi C P D, Indian J. pure appl. Phys., 13 (1975), 570.
19. Mooney E F, Spectrochim. Acta, 20 (1964), 1343.
20. Nabumi Oi & Coetzee J F, J. Am. chem. Soc., 91 (1969), 2473.
21. Tripathi G N R & Ram S, Indian J. pure appl. Phys., 12 (1974), 529.
22. Dwivedi B K, Singh I D & Maheshwari R C, Indian J. pure appl. Phys., 12 (1974), 597.
23. Mooney E F, Spectrochim. Acta, 19 (1963), 877.
24. Sharma S N & Dwivedi C P D, Indian J. Phys., 50 (1976), 25.

Realization of Active Bandpass Filters

R S SHARMA & U K DULLU

Department of Physics, University of Kashmir, Srinagar

The general scheme of an amplifier with negative feedback is studied and the active bandpass filters are then derived as particular cases of this general scheme using the single pole mode of operational amplifier.

1. Introduction

An active bandpass filter consists of an operational amplifier as an active element and RC network as passive elements. In the following study, the active element of the network is assumed to possess the ideal attributes : infinite input impedance, zero output impedance and zero feedback transmission. Apart from this, the open loop frequency response of the operational amplifier is represented in the form[1-2]

$$A(s) = -\frac{A_0\,\omega_0}{s+\omega_0} \qquad \ldots(1)$$

where A_0 is the open-loop dc differential gain, ω_0 is the open-loop bandwidth of operational amplifier and s is the complex frequency variable. This property has been utilized in the synthesis of active filters which results in filters that are economical, stable and have an extended range of frequency.[2-6] Active bandpass filters are derived here as a particular case of the general scheme using single negative feedback amplifier circuit with single pole operational amplifier mode. The diagram of this circuit is given in Fig. 1, where each element y_i represents a resistor, a capacitor or a combination of resistor and capacitor. The transfer function of this circuit is given by

$$\frac{V_0}{V_i} = \frac{-A\,y_1\,y_2}{(y_1+y_3)\,(y_2+y_4)+y_2\,y_4+A\,y_2 y_3} \qquad \ldots(2)$$

2. Second Order Filters

Case 1—Let us choose $y_1 = C_1 s$, $y_2 = 1/R_2$, $y_3 = 1/R_3$ and $y_4 = 1/R_4$. The filter circuit is given in Fig. 2 and Eq. (2) reduces to

$$\frac{V_0}{V_i} = \frac{-A\,C_1\,R_3\,R_4\,s}{(R_3\,C_1\,s+1)\,(R_2+R_4)+(R_3+A\,R_4)} \qquad \ldots(3$$

Substituting Eq. (1) in Eq. (3), one obtains

$$\frac{V_0}{V_i} = \frac{-A_0\,\omega_0\,\dfrac{R_4}{R_2+R_4}\,s}{\left[s^2+s\left\{\omega_0+\dfrac{1}{R_3C_1}+\dfrac{1}{C_1(R_2+R_4)}\right\}\right.}$$
$$\left. + \left\{\omega_0\dfrac{(A_0+1)\,R_4+R_2+R_3}{R_3\,C_1\,(R_2+R_4)}\right\}\right] \qquad \ldots(4)$$

This circuit gives a bandpass response with centre frequency ω_c, quality factor Q and the mid band gain H_0 given by

$$\omega_c = \left[\frac{\omega_0\,\{(A_0+1)\,R_4+R_2+R_3\}}{R_3\,C_1\,(R_2+R_4)}\right]^{1/2} \qquad \ldots(5)$$

$$Q = \frac{[\omega_0\,\{(A_0+1)\,R_4+R_3+R_2\}\,R_3C_1\,(R_2+R_4)]^{1/2}}{\omega_0 R_3 C_1\,(R_2+R_4)+R_2+R_3+R_4} \qquad \ldots(6)$$

$$H_0 = \frac{A_0\,\omega_0\,R_3\,R_4\,C_1}{\omega_0 R_3 C_1\,(R_2+R_4)+R_2+R_3+R_4} \qquad \ldots(7)$$
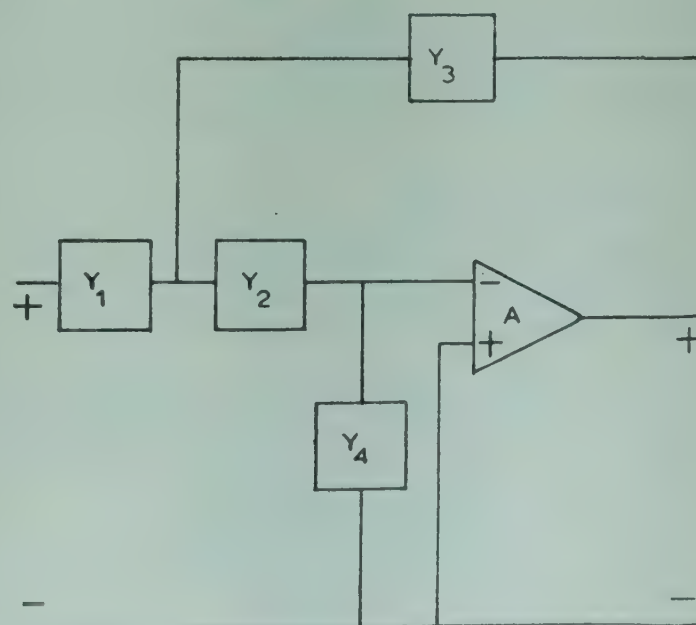

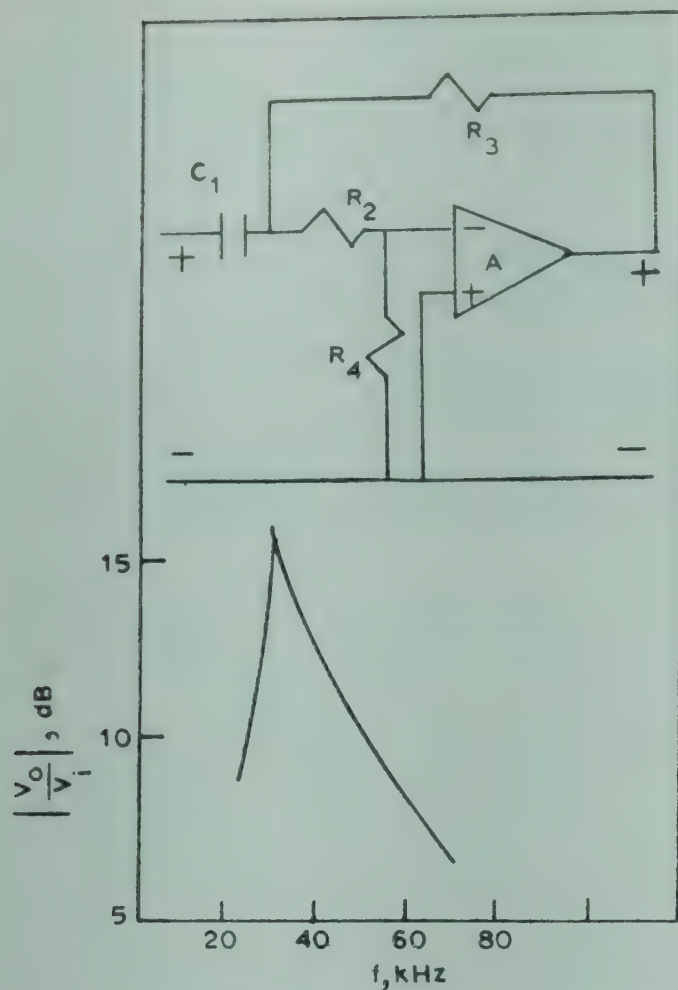Fig. 1—General scheme of an amplifier with feedback

Fig. 2—A second order bandpass network and its response

In the following experimental work, the operational amplifiers used are of the internally compensated operational amplifier 741 CT. The components used are $R_2 = 15$ kΩ, $R_3 = 15\cdot3$ kΩ, $R_4 = 15$ kΩ and $C_1 = 1000$ pF. The response of this circuit is shown in Fig. 2 and its Q is $2\cdot7$

Case 2—If in Fig. 1, y_2 represents a capacitor and rest of the elements are resistors, a bandpass filter circuit can be realized. Yet another bandpass filter results if y_1 and y_3 are taken as capacitors and other elements represent resistors. As both the circuits are of low Q value, these need not be elaborated.

3. Higher Order Filters

Case 1—Let us take $y_1 = C_1 s$, $y_2 = 1/R_2$, $y_3 = 1/R_3$ and $y_4 = (R_4 C_4 s + 1)/R_4$. These values represent the circuit of Fig. 3. The transfer function of this circuit is

$$
\frac{V_0}{V_i} = \left\{ -\frac{A_0\,\omega_0}{R_2\,C_4}\,s \right\} \Bigg/ \Bigg[s^3 + s^2 \left\{ \omega_0 + \frac{K_1}{R_2\,R_3\,R_4\,C_1\,C_4} \right\}
$$
$$
+ s \left\{ \frac{\omega_0\,K_1 + R_2 + R_3 + R_4}{R_2\,R_3\,R_4\,C_1\,C_4} \right\}
$$
$$
+ \frac{\omega_0\,(R_2 + R_3 + R_4 + A_0 R_4)}{R_2\,R_3\,R_4\,C_1\,C_4} \Bigg] \qquad \ldots(8)
$$

where $K_1 = (R_2 + R_4)\,R_3\,C_1 + R_2\,R_4\,C_4 + R_2\,C_4\,R_4$

This circuit gives a response with an additional undesirable pole. The circuit has been found to be suitable for filter application at medium frequencies. Let us choose $C_1 = 100$ pF, $C_4 = 1000$ pF, $R_2 = 151\cdot1$ kΩ, $R_3 = 102$ kΩ and $R_4 = 100$ kΩ. The response of this filter is shown in Fig. 3, Curve 1.

This circuit can be reduced to a second order bandpass filter if either C_4 or R_2 is taken as zero. When C_4 is taken as zero, the circuit reduces to that of Fig. 2. When $R_2 = 0$, the transfer function in Eq. (8) becomes

$$
\frac{V_0}{V_i} = -A_0\,\omega_0\,\frac{C_1}{C_1 + C_4}\,s \Bigg/ \Bigg[s^2
$$
$$
+ s \left\{ \omega_0 + \frac{R_3 + R_4}{R_3\,R_4\,(C_1 + C_4)} \right\} + \frac{\omega_0\,\{R_3 + R_4\,(A_0 + 1)\}}{R_3\,R_4\,(C_1 + C_4)} \Bigg]
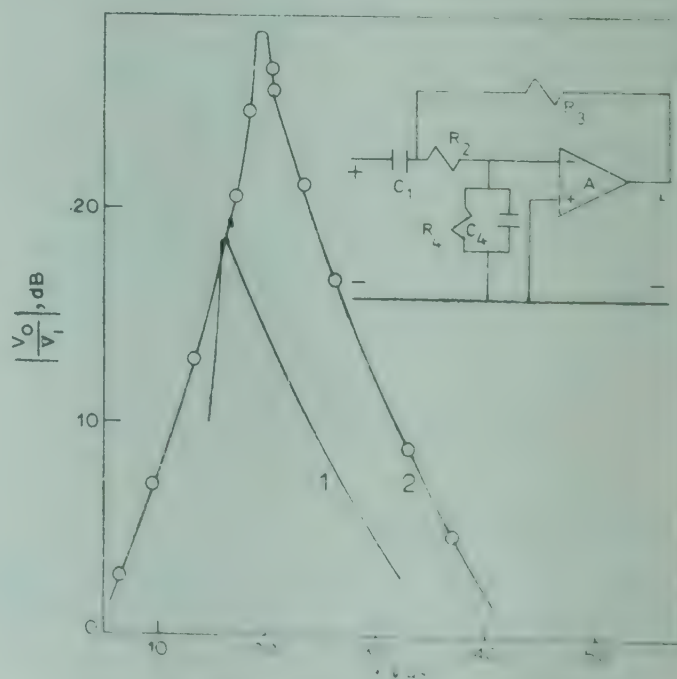$$
$$
\ldots(9)
$$

Then $\omega_c = \left[\frac{\omega_0\,\{R_3 + R_4\,(A_0 + 1)\}}{R_3\,R_4\,(C_1 + C_4)} \right]^{1/2} \qquad \ldots(10)$

$$
Q = \frac{[\omega_0\{R_3 + R_4\,(A_0 + 1)\}\,R_3\,R_4\,(C_1 + C_4)]^{1/2}}{\omega_0\,R_3\,R_4\,(C_1 + C_4) + R_3 + R_4} \qquad \ldots(11)
$$

$$
H_0 = \frac{A_0\,\omega_0\,C_1\,R_3\,R_4}{\omega_0\,R_3\,R_4\,(C_1 + C_4) + R_3 + R_4} \qquad \ldots(12)
$$

The components used are $C_1 = 100$ pF, $C_4 = 100$ pF, $R_3 = 1$ MΩ, $R_4 = 1$ MΩ and the response of this network is as shown in Fig. 3, curve 2. The Q of this circuit is $10\cdot4$.

Case 2—Let $y_1 = C_1 s/(R_1 C_1 s + 1)$, $y_2 = \infty$, $y_4 = 0$ and $y_3 = [(R_3 C_3 s + 1)/R_3]$. The transfer function of this circuit will have the form given in Eq. (13).

Fig. 3—A third order bandpass network and its response with (curve 1) and without R_2 (curve 2)

$$\frac{V_0}{V_i} = \left(-\frac{A_0\,\omega_0}{R_1\,C_3}\,s\right)\bigg/\bigg[s^3 + s^2\{K_2 + \omega_0\,(1 + A_0)\}$$

$$+ s\left\{K_2\,\omega_0 + \frac{1 + A_0\,\omega_0\,(R_1\,C_1 + R_3\,C_3)}{R_1\,C_1\,R_3\,C_3}\right\}$$

$$+ \frac{\omega_0(1 + A_0)}{R_1\,C_1\,R_3C_3}\bigg] \qquad \ldots(13)$$

where $K_2 = \dfrac{R_1C_1 + R_3C_1 + R_3C_3}{R_1C_1R_3C_3}$

The undesirable pole of this bandpass filter can be removed if either $R_1 = 0$ or $C_3 = 0$. When $R_1 = 0$, the transfer function reduces to

$$\frac{V_0}{V_i} =$$

$$\frac{\left(-A_0\,\omega_0\,\dfrac{C_1}{C_1 + C_3}\,s\right)}{\left[s^2 + s\left\{\omega_0 + \dfrac{A_0\,\omega_0\,R_3\,C_3 + 1}{R_3\,(C_1 + C_3)}\right\} + \dfrac{(A_0 + 1)\,\omega_0}{R_3\,(C_1 + C_3)}\right]} \qquad \ldots(14)$$

Here the centre frequency, quality factor and the mid-band gain are given by

$$\omega_c = \left[\frac{(A_0 + 1)\omega_0}{R_3\,(C_1 + C_3)}\right]^{1/2} \qquad \ldots(15)$$

$$Q = \frac{[(A_0 + 1)\,\omega_0 R_3\,(C_1 + C_3)]^{1/2}}{\omega_0 R_3\,(C_1 + C_3) + A_0\omega_0 R_3 C_3 + 1} \qquad \ldots(16)$$

$$H_0 = \frac{A_0\,\omega_0\,R_3\,C_1}{\omega_0\,R_3\,(C_1 + C_3) + A_0\,\omega_0\,R_3\,C_3 + 1} \qquad \ldots(17)$$

The components used are $C_1 = 0.1\ \mu F$, $C_3 = 100pF$, $R_3 = 10^3\ \Omega$ and the response of this network is as shown in Fig. 4, curve 1 (with $Q = 12.1$). When $C_3 = 0$, the transfer function becomes as in Eq. (18).
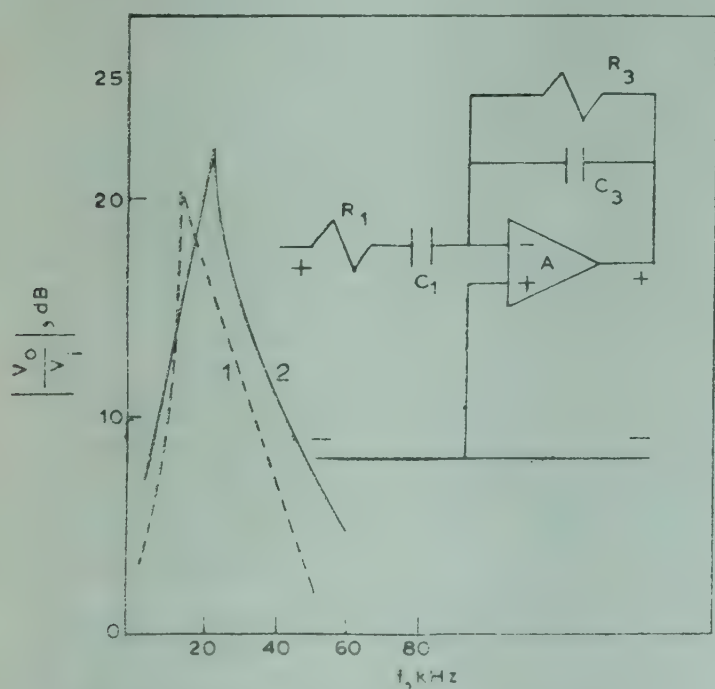

Fig. 4—A third order network and the response of the filters with (curve 1) $R_1 = 0$ and (curve 2) $C_3 = 0$

Table 1—Calculated Values of ω_c and Q Sensitivities of Second Order Circuits

	Fig. 2	Fig. 3 with $R_2 = 0$	Fig. 4 with $R_1 = 0$	Fig. 4 with $C_3 = 0$
ω_c Sensitivities				
$S_{A_0}^{\omega_c}$	0·49	0·49	0·49	0·49
$S_{\omega_0}^{\omega_c}$	$\frac{1}{2}$	$\frac{1}{2}$	0·5	0·50
$S_{C_1}^{\omega_c}$	$-\frac{1}{2}$	$-0·25$	$-0·49$	$-0·5$
$S_{C_3}^{\omega_c}$			$-0·0004$	
$S_{C_4}^{\omega_c}$		$-0·25$		
$S_{R_1}^{\omega_c}$			$-0·00004$	
$S_{R_2}^{\omega_c}$	$-0·2$			
$S_{R_3}^{\omega_c}$	$-0·4$	$-0·5$	$-0·5$	$-0·49$
$S_{R_4}^{\omega_c}$	0·25	$-0·00001$		
Q Sensitivities				
$S_{A_0}^{Q}$	0·49	0·49	0·31	0·47
$S_{\omega_0}^{Q}$	0·49	0·49	0·31	0·44
$S_{C_1}^{Q}$	0·49	0·24	0·48	0·44
$S_{C_3}^{Q}$			$-0·17$	
$S_{C_4}^{Q}$		0·24		
$S_{R_1}^{Q}$				0·02
$S_{R_2}^{Q}$	0·07			
$S_{R_3}^{Q}$	0·16	0·003	0·31	0·49
$S_{R_4}^{Q}$	0·41	0·9		

$$\frac{V_0}{V_i} =$$

$$\frac{-A_0\,\omega_0\,\dfrac{R_3}{R_1 + R_3}\,s}{\left[s^2 + s\left\{\omega_0 + \dfrac{A_0\,\omega_0\,C_1\,R_1 + 1}{C_1\,(R_1 + R_3)}\right\} + \dfrac{\omega_0\,(A_0 + 1)}{C_1\,(R_1 + R_3)}\right]} \qquad \ldots(18)$$

For this circuit

$$\omega_c = \left[\frac{\omega_0\,(A_0 + 1)}{C_1\,(R_1 + R_3)}\right]^{1/2} \qquad \ldots(19)$$

$$Q = \frac{[(A_0 + 1)\,\omega_0 C_1\,(R_1 + R_3)]^{1/2}}{\omega_0\,C_1\,\{R_1\,(A_0 + 1) + R_3\} + 1} \qquad \ldots(20)$$

$$H_0 = \frac{A_0\omega_0 R_3 C_1}{\omega_0 C_1\,\{R_1\,(A_0 + 1) + R_3\} + 1} \qquad \ldots(21)$$

287

The components used are : $C_1 = 100$ pF, $R_1 = 10^2\ \Omega$ and $R_3 = 10^6\ \Omega$. The response of this filter is depicted in Fig. 4, curve 2 (with $Q = 14.5$).

4. Sensitivity Parameters

The ω_e and Q sensitivities have been calculated for the considered circuits using the usual definition of sensitivity, viz.

$$S_X^Q = \frac{X}{Q}\ \frac{dQ}{dX}$$

and the results are presented in Table 1.

5. Conclusion

Circuits of the active bandpass filters have been developed using the single pole representation of the operational amplifier. These circuits have been derived as particular cases of the general scheme of an amplifier with negative feedback. Most of these filter circuits can find practical utility at medium frequencies and have low sensitivities to element variation.

References

1. Budak A & Zeller E R, *IEEE Solid-St. Circuits*, **17** (1972), 308.
2. Gumussoy M & Holt A G J, *Int. J. Electron.*, **43** (1977), 473.
3. Geffe R, *IEEE Spectrum*, **7** (1970), 63.
4. Hribsek M & Newcomb R W, *IEEE Trans. Circuits System*, **23** (1976), 166.
5. Mitra A & Aatre V K, *Electron. Lett.*, **12** (1976), 226.
6. Tarmy R & Ghausi M S, *IEEE Trans. Circuits Theory*, **17** (1970), 358.

Communications

A New Type of Irradiation Head for Activation Analysis

A G JOGLEKAR, (Mrs) P S LAHOTI, M R BHIDAY & V N BHORASKAR

Department of Physics, University of Poona, Poona 411 007

The design and working of a new type of irradiation head, along with an electronic control system are described. The irradiation head can locate the sample vial in a precisely known horizontal position with an accuracy of ± 0·1 mm. The electronic system provides an automatic control for all the operations needed in the activation analysis experiments.

The activation analysis of samples by neutrons or gamma rays is usually carried out by pushing the sample vial pneumatically, through a PVC tube and allowing it to fall freely under gravity to occupy a stationary vertical position in front of the radiation source. However, this method is not suitable when the sample has to be irradiated in a horizontal position, which might be an experimental requirement. This problem was particularly realized in this laboratory, when we had to use electron beam of the 8 MeV racetrack microtron,[1] for sample irradiation, in all the eight orbits. The orbits of the microtron are in the horizontal plane, and moreover, the electron beam has an inherent horizontal spread larger than the vertical one (the horizontal and vertical dimensions of the beam are 12 mm and 5 mm respectively). The sample, therefore, has to be kept horizontally, perpendicular to the beam direction, to receive almost all the electrons, and therefore, the gamma rays. Further, the orbit separation is 3 cm and with the beam-spread of about 12 mm, it imposes a requirement for an accurate location of the sample with respect to the beam.

Similarly while making the use of 14 MeV neutrons of this laboratory, for the activation analysis, the horizontal position of the sample vial was essential, since the deuteron beam after coming out of the accelerating column develops a horizontal spread in the plane normal to its motion. The sample kept near the tritium target thus receives an average uniform flux, only when the sample vial is kept horizontal. An irradiation head, is therefore, designed and fabricated, which locks the sample vial in the horizontal direction, with precisely known position. An electronic control system which controls the various operations involved in the neutron activation analysis is made. The sample travel time can be reduced to 0·5 sec, and therefore, the system is useful in the study of nuclides with short half lives.[2]

Irradiation head—Details of the irradiation head are shown in Fig. 1. It consists of a rectangular polyethylene block B of dimensions : 46 mm length. 40 mm height, and 20 mm width. Two holes are drilled, one of 7 mm diameter along the length (H, horizontal hole), and the other of 5 mm diameter along the height (V, vertical hole) crossing each other at the centre of the block. At the surface of the hole H, a U-shaped groove G (3 mm depth and 3 mm wide) is made, which runs from the junction of the holes to one of the ends where a compressible spring is fitted. At the free end of the spring S, an L shaped stainless steel strip S_t (2 mm width, 5 mm height, 15 mm length) is spot welded. The long leg of the strip passes through the groove and terminates inside the junction of the holes where it holds an aluminium rod R (4 mm diameter, 12 mm height) kept in the upper half of the vertical hole. The top end of the vertical hole is closed and below it at a distance of about 4 mm a phototransistor assembly PT_1 is fitted, to monitor the position of the aluminium rod. The end of the horizontal hole where a spring is fitted, the bottom end of the vertical hole and the other end of the horizontal hole (for sample entrance) are connected by PVC tubing to air compressor through solenoidal valves V_A, V_B and V_0 respectively (not shown in Fig. 1).
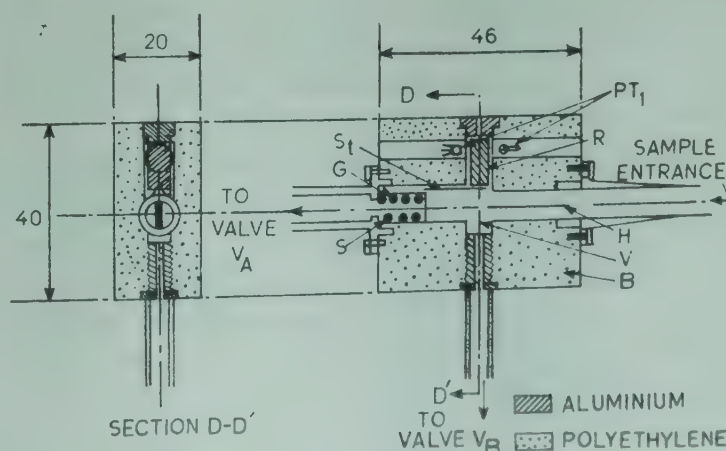

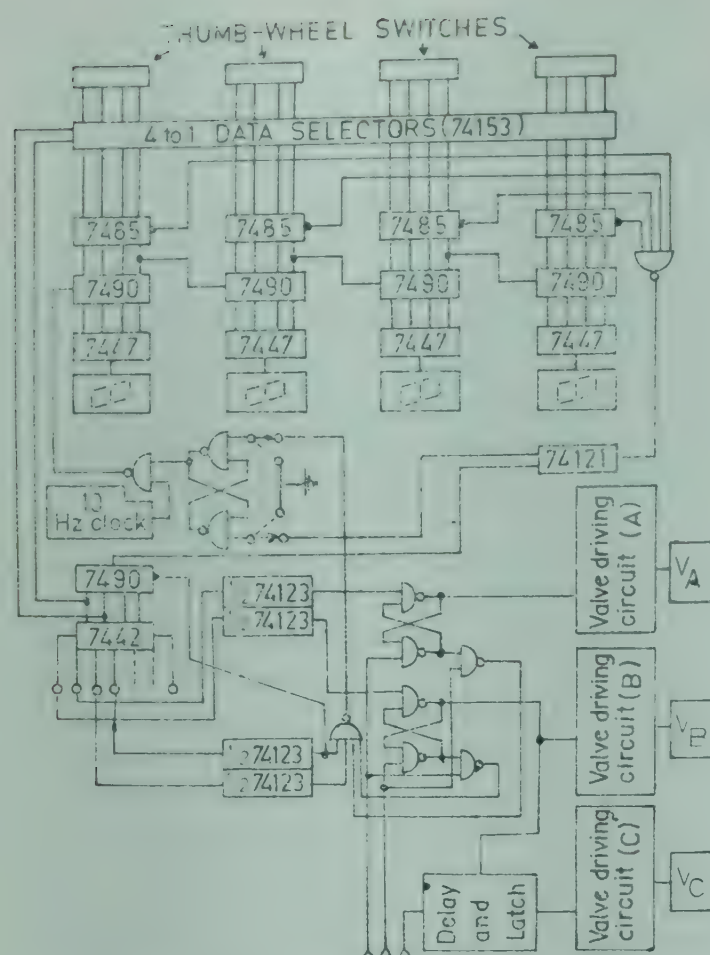Fig. 1—Schematic diagram of the irradiation head

Fig. 2—Electronic control system for the activation analysis

In the actual operation, the irradiation head is kept in such a way that the aluminium rod rests vertically on the strip end. The sample vial after coming from the counting station enters the horizontal hole and while compressing the spring gradually comes to rest. Compression of the spring moves the strip away from the junction of the holes and thereby clearing the path of the aluminium rod to fall down under gravity, (since the strip end now comes inside the grooves), and to rest on a screw fitted in the lower half of the vertical hole. In the meantime, the sample vial comes to rest, and the spring while expanding pushes the vial towards the centre. Finally, the sample vial is locked between the aluminium rod and the spring. The assembly, therefore, defines precisely the position of the sample vial in the horizontal direction, which is preset to receive the maximum radiation.

When the irradiation period is over, an electrical signal from the control circuit opens the solenoidal valve V_B and the aluminium rod is pushed up by air pressure and remains in the lifted position, touching the top end of the vertical hole, until the valve V_B is closed by the signal from the phototransistor assembly PT_1. The signal from PT_1 also opens the valve V_A and the sample is pushed pneumatically to the counting station. As the sample

vial reaches the counting station, an electrical signal from the phototransistor PT_3 closes the valve V_A. The action of the irradiation head is repeated, in the next cycle. The polyethylene block and the PVC tubes are fitted inside an aluminium tube casing, with one end closed, to enable the operation of the irradiation head inside the vacuum chamber.

Electronic system—One cycle of activation is divided into four parts[3]—(1) irradiation (2) waiting to reduce the interference (cooling), (3) counting of the induced activity, and (4) waiting to reduce back-ground build-up effects. For each part, one time interval is pre-selected, the duration of which, depends upon the element to be analyzed, and the interference and background present in the sample. The task of electronic control system is (i) to monitor time intervals for each operation and (ii) to maintain the sequence of operations with the help of pneumatic valves (V_A, V_B and V_C).

Fig. 2 shows the electronic control system schematically. It can be divided into two parts (1) programmable timer and (2) control circuitry. The programmable timer is used to preset and monitor time intervals for each operation, while the control part takes care of the sequence of operations, as well as, interfacing with the input-output devices. The programmable timer consists of 4 sets of 4 digit thumb-wheel switches (to preset time intervals for each of the four operations, from 0 to 999.9 sec, in the steps of 0.1 sec), 4 lines to 1 line data selectors (74153), magnitude comparators (7485), decade counters (7490) and a latch to start and stop the timer. The chain of decade counters (7490) counts the pulses of 10 Hz, derived from a crystal controlled clock, and produce corresponding BCD output. This output is compared, in the magnitude comparators (7485), with the BCD multiplexed data of the thumb-wheel switches. When the number of pulses counted in the decade counters becomes equal to that preset on the thumb-wheel switches, the magnitude comparators provide a signal, which stops the timer through the latch. The timer can be started either manually, or by a + 5 V TTL pulse, and when it stops, it provides a TTL pulse for the control circuitry. The control circuit provides the address signals for the multiplexers which select one time setting at a time, in a proper sequence.

The control circuit consists of a decade counter which counts the STOP pulses of the timer, and drives various latches through the decoder (7442). The latches receive the information from the phototransistor sensors which provides the TTL compatible pulses, when the sample reaches the either end.

The latches then drive the solenoidal valves V_A, V_B and V_C which limit the transfer process by controlling the air pressure. The PT_2 assembly at the entrance of the irradiation head (not shown in Fig. 1) controls V_B.

Performance of the system—This electronic control system was successfully tested for activation analysis with D-D and Li-D neutrons. The system is found very reliable in respect of the different timing circuits for the four operations. The Hewlett-Packard timer/counter model 5308A was used to calibrate the timer and travelling time measurement circuit. The horizontal position of the 15 mm long sample in the irradiation head could be known precisely within $\pm$ 0·1 mm for sample speeds from 60 m/sec to 150 m/sec. This measurement was limited only by the reproducibility of the mechanical properties of the spring and the measurement of sample dimensions. The present system can also be used for experiments with reactor neutrons.

References

1. Brannen E, Forelich H, & Sells V, *Can. J. Phys.*, 43 (1965), 1555.
2. Grass F, *Atomkernenergie (ATKE)*, Bd 25, Lfg. 4. (1975), 243.
3. Amemiya S, Itoh M, Kawade K, Yamamoto H & Katoh T, *J. nucl. Sci. Tech.*, 11 (1974), 395.

Notes

Luminescence of ZnO Phosphor in Green and Red Regions

R S SONI, P S DIWAN & S SIVARAMAN

Department of Physics, University of Saugar
Sagar

ZnO phosphors prepared by decomposing $ZnCO_3$, Zn $(NO_3)_2$, $ZnSO_4$, Zn $(CH_3COO)_2$ and $Zn(OH)_2$ have been found to be completely non-luminescent under UV excitation at room temperature. But ZnO phosphors prepared by firing with small amounts of Zn have been found to become luminescent under UV excitation (365 nm) at room temperature and emit two bands, one in the green region at 535 nm and the other in the red region at 750 nm.

The luminescence studies on ZnO phosphors show dissimilar features depending upon the method of preparation. Some investigators have reported that ZnO phosphors are luminescent under UV (365 nm) at room temperature, when prepared in vacuum[1] or in an atmosphere of nitrogen.[2] Bundel and Zhukov[3] and Joshi and Kumar[4] have also reported that the ZnO phosphors are luminescent under UV (365 nm) at room temperature, when prepared in air (oxygen); Lehmann[5] has, however, contradicted these results. Further, the ZnO phosphors have also been reported to be luminescent under 365 nm excitation at room temperature, when prepared in a reducing atmosphere.[4-6]

Emission bands in ZnO phosphors in green,[6-8] yellow[9] and orange[10] regions have been reported. A fourth band in the red region at 750 nm has also been reported by Lehmann,[7] Osiko,[11] Gerbshtein and Zelikin[12] and Lauer[13] at liquid air temperature. Though the emission of ZnO has been the subject of a large number of investigations, the results have been conflicting. Hence, the present study was undertaken to study the luminescence spectra of ZnO phosphors prepared from different sources, with a view to gaining further insight into the fluorescence characteristics.

Experimental details—ZnO phosphors were prepared from different sources, decomposing $ZnCO_3$, Zn $(NO_3)_2$, $ZnSO_4$, $7H_2O$ and zinc acetate (all AR grade) at high temperatures. ZnO was also prepared by dehydration of $Zn(OH)_2$ obtained by precipitation from a solution of $ZnSO_4$. $7H_2O$ to which 30% of ammonium hydroxide (A R grade) was added. ZnO so obtained was fired in air at 1000°C for 2 hr. These phosphors were completely non-luminescent under UV (365 nm) at room temperature. The non-luminescent ZnO phosphor was refired with small amounts (0·05, 0·1 and 0·5 mole%) of Zn for 2 hr at 700 and 1000°C respectively in evacuated (10^{-3} mm of Hg) quartz tubes. ZnO phosphor then became luminescent under UV (365 nm) at room temperature, though the more favourable for emission was the one with 0·1 mole% of Zn and 1000°C temperature. The cathode ray chamber designed and built by us consisted of a glass tube fixed to a metal box at one end. Electrodes, insulated from the body, were introduced at both ends. Provision was made for evacuation, light gathering, temperature control of anode, etc. The phosphor was placed in a holder attached to the anode. Cathode rays were produced after evacuating the chamber up to 10^{-4} mm of Hg and operating it at 5 kV and 3 mA current density. The fluorescence spectra were recorded at room temperature using Bellingham and Stanley spectrometer coupled with a photonmeter.

Results and discussion—ZnO phosphors prepared in air are completely non-luminescent under UV (365 nm) at room temperature which supports Lehmann's observations.[5] But when these phosphors are refired with an excess of Zn and excited by UV (365 nm), the fluorescence spectra of these phosphors show two bands peaking at 535 nm and 750 nm (Fig. 1) in the green and red regions respectively.

The non-luminescence of ZnO phosphors (prepared in air) under UV excitation at room temperature is also supported by the thermoluminescence study of ZnO crystals made by Shalimova *et al.*[14] at low temperatures. They have reported two peaks at 110 and 180 K for the green band (513 nm) and one peak at 150 K for the yellow band (upon excitation by UV 365 nm). The bands vanish at about 200K (far below room temperature). Thus the room temperature is in the range of quenching
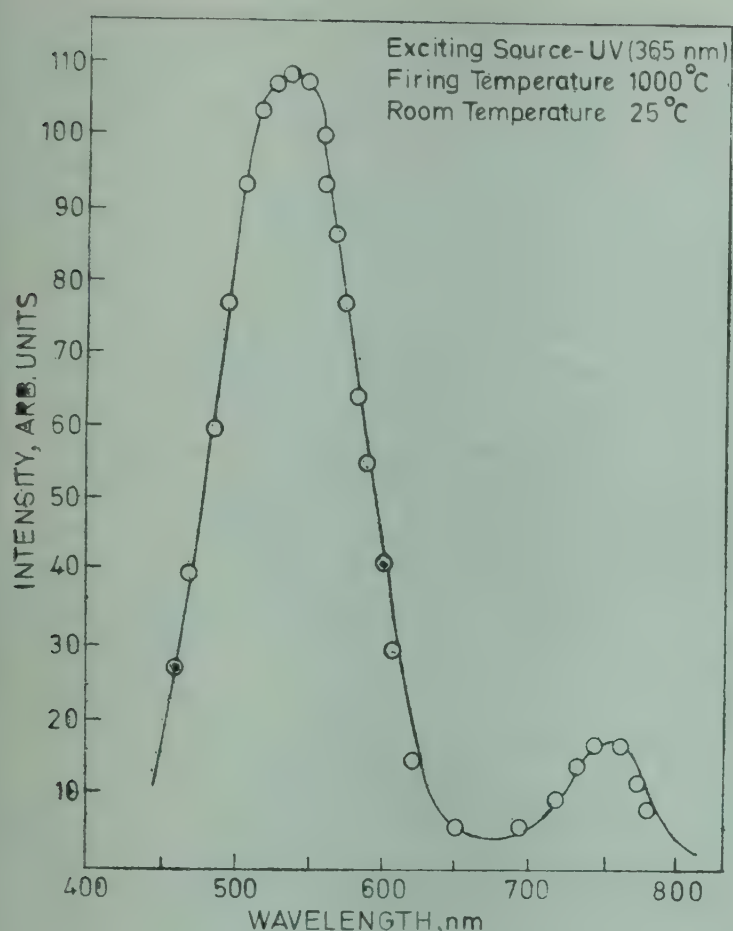
Fig. 1—Fluorescence spectra of ZnO with excess of Zn upon excitation by UV (365 nm)

Fig. 2—Fluorescence spectra of ZnO fired in air upon excitation by cathode rays

temperatures for such ZnO phosphors. However, if it is excited by a higher energy source, viz. cathode rays or X-rays, it becomes luminescent even at room temperature, giving two bands at 515 nm and 550 nm (Fig. 2) in the green region. The possibility of green emission of ZnO due to the presence of sulphur (few parts per million) as suggested by Lehmann[7] and Thomson[8] has been ruled out by Kröger and Vink.[6] This green emission may be due to the fact that ZnO is an n-type semiconductor with donor levels at 0·04-0·05 eV below the conduction band. These levels are caused by interstitial Zn in concentrations ranging from 10^{15} to 10^{18} atoms/cm³ depending upon the method of preparation of the phosphor.

The green emission band at 535 nm (upon excitation by UV 365 nm) at room temperature, possibly may be due to anion vacancies produced by firing the phosphor, either with traces of Zn or in a reducing atmosphere, resulting in an excess of zinc in the phosphor. The excess of Zn may be incorporated either in the interlattice or at the normal lattice sites with the formation of an equivalent amount of a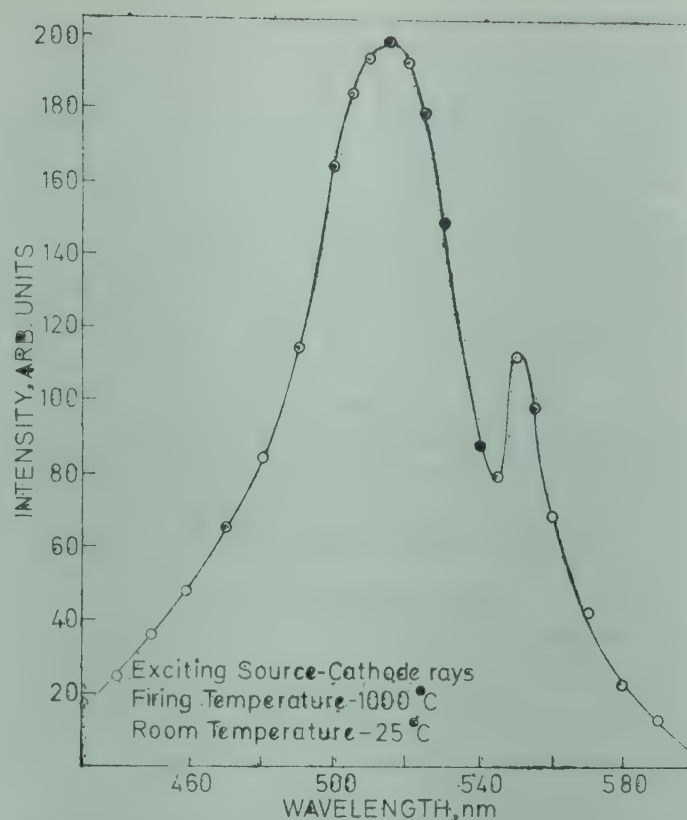nion vacancies $(V_A)^{2-}$. Due to deviation from stoichio-metry, a two-electron centre is formed which may be either interstitial Zn or $(V_A)^{2-}$. The second electron is ionized only optically and fluorescence occurs upon recombination.[5] Our investigation does not support a study made of green emission on the basis of comparison of Zeeman data and ESR, suggesting that one of the possibilities for the green centre is a substitutional Cu impurity at a regular lattice site.[15]

Osiko[11] and Zelikin[16] found that when ZnO phosphors showing green luminescence are refired with excess of Zn the annealing process at 450-500°C gives rise to red emission. In our investigation too, similar annealing has been done but at a higher temperature (1000°C). As the ZnO phosphors have been prepared by firing in air for several hours, it may be conveniently assumed that the red luminescence centres appear as a result of an oxidation process occurring in the surface layer of ZnO crystallites. We assume that the emergence of red luminescence centres is related to oxidation of Zn which is found on the ZnO surface.[12]

References

1. Bhusan S & Saleem M, *Phys. Status Solidi A.*, 38 (1976) K27.
2. Pandeya K N, Balkrishna S & Kanari P S, *Indian J. pure appl. Phys.*, 11 (1973), 227.
3. Bundel A A & Zhukov G V, *Optics Spectrosc.*, 22 (1967), 103.
4. Joshi J C & Kumar R, *Indian J. pure appl. Phys.*, 11 (1973), 422.
5. Lehmann W, *Solid-St. Electron.*, 9 (1966), 1107.
6. Kröger F A & Vink H J, *J. chem. Phys.*, 22 (1954), 250.
7. Lehmann W, *J. electrochem. Soc.*, 115 (1968), 538.
8. Thomson S M, *J. chem. Phys.*, 18 (1950), 770.
9. Zelikin Ya M & Zhukovskii A P, *Optics Spectrosc.*, 11 (1961), 397.
10. Morkovskii L Ya & Orshankaya N S, *Optics Spectrosc.*, 9 (1960), 40.
11. Osiko V V, *Optics Spectrosc.*, 7 (1959), 454.
12. Gerbshtein Ya M & Zelikin Ya M, *Optics Spectrosc.*, 28 (1970), 521.
13. Lauer R B, *J. Phys. Chem. Solids*, 34 (1973), 249.
14. Shalimova K V, Nikitenko V A & Pasko P G, *Optics Spectrosc.*, 39 (1975), 597.
15. Dingle R, *Phys. Rev. Lett.*, 23 (1969), 579.
16. Zelikin Ya M, *Vestn. Leningr. Univ. Fiz. Khim.*, 2 (1966), 51.

Effect of *in situ* Annealing on Electrical Properties of MnBi Films

P C ACHAR & R N KAREKAR

Department of Physics, University of Poona, Pune 411 007

MnBi Films of three different compositions (Bi to Mn wt ratio being 2·33, 2·63 and 3·37) were vapour deposited, and *in situ* dc resistances of the films were measured at various temperatures. A typical dependence of resistance on composition was observed, which can be used for controlling the compound formation of MnBi during the deposition process.

The properties of vapour-deposited films often vary in an unpredictable manner even when prepared by apparently identical processes. The present work on MnBi films was carried out as a preliminary study, especially to control the properties of the film during annealing, and is planned for use in magneto-optical studies. However, during this work some typical dependence of dc electrical resistance on composition was found, which is reported in this communication. The aim was to see whether annealing the films in vacuum could give better control. This was ascertained by *in situ* dc resistance measurement with variation of annealing temperature. Further such vacuum annealing may give better results compared to the films annealed in atmosphere after giving a protective layer.[1]

Thin planar films of MnBi were deposited between Al electrodes by sequential evaporation[1] of Bi and Mn on microslides, keeping the weight ratio Bi/Mn at 2·33, 2·63 and 3·37, Bi weight being kept fixed (i.e. volume ratio 1·71, 1·93 and 2·47 respectively); volume ratio of 1·93 is reported to be best for complete MnBi formation.[1] Substrate temperature was kept at 50°C which is reported to be favourable for achieving crystalline phase of bismuth.[2] Films were vacuum annealed at temperatures ranging from room temperature to 300°C in steps of 5°C/min and subsequently cooled back to room temperature. Heating and cooling time were kept at 1 hr and 2 hr respectively. The vacuum throughout the operation was better than 2×10^{-5} torr. *In situ* resistance measurement with variation of temperature was carried out by using Phillips VTVM GM 6001.

Average resistance-temperature curves (Fig. 1) are plotted for the three compositions. Some variability was observed in the three curves (e.g. the highest value of R/R_{NA} for the composition 3·37 was observed at 1·55 ± 0·23), which is indicated by bars at important points. All the three curves in Fig. 1 show a lowest final constant value of the resistance (R/R_{NA}) at a certain temperature (the annealing

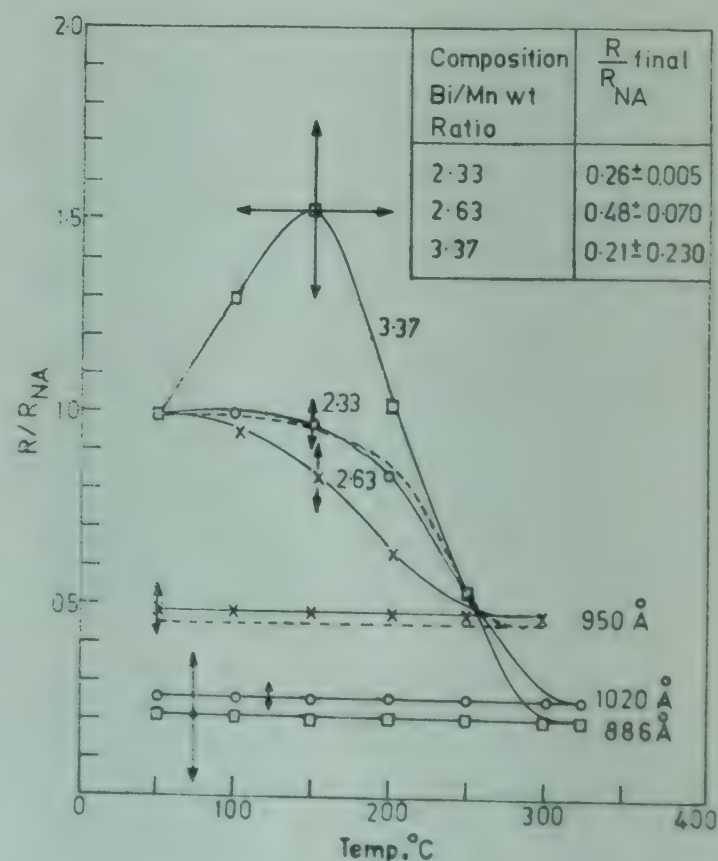| Composition Bi/Mn wt Ratio	$\dfrac{R}{R_{NA}}$ final
2·33	0·26 ± 0·005
2·63	0·48 ± 0·070
3·37	0·21 ± 0·230

Fig. 1—Variation of resistance (*R*) of annealed MnBi films with temperature at various compositions, [R_{NA} is the initial resistance of the films (not annealed); dashed curve shows Skalsky's curve.]

temperature). No change was observed in the final R/R_{NA} values on further temperature cycling.[3] For the compositions (Bi/Mn wt ratio) 2·33, 2·63 and 3·37, the lowest constant values of R/R_{NA} are found to be $0·26 \pm 0·005$, $0·48 \pm 0·07$ and $0·21 \pm 0·23$ respectively. The different types of behaviour shown by resistance-temperature curves for these different compositions may be of help in controlling the properties of the films, particularly for the required composition of 2·63.

Curves for composition 2·33 and 2·63 show almost similar type of variation, i.e. somewhat constant value up to 150°C and then gradual fall to constant irreversible resistances. However, the curve for composition 3·37 shows a rise in R/R_{NA} value up to about 150°C. It may be noted that the resistance fall is observed to start for all the three compositions, at about 150°C.

This approximate constancy of the R/R_{NA} value up to about 150°C for 2·33 and 2·63 compositions indicates that there is no major change in Mn-Bi structure with temperature, i.e. compound formation does not start below this temperature. The fall in resistance after 150°C can be attributed to the compound formation as suggested by Skalsky et al.[1] and partly to the decay of the lattice distortions like lattice vacancies and lattice excesses.[3,4]

The observed initial rise in the resistance for the composition 3·37 (where Mn thickness is least, Bi thickness being kept same throughout) can be ascribed to the temperature variation of the particle spacing. Different possibilities are as follows.

One is that the particle spacing may increase due to thermal expansion of the substrate, the Mn particles being strongly bound to the substrate (Bi layer). We assume here that Mn is in the form of islands on Bi substrate and hence an increase in resistance due to increase in temperature is observed.[4,5] The other possibility is agglomeration of Mn particles on Bi substrate. Agglomeration effect at higher temperature is reported to be due to mobility of particles on rigid substrate which may give rise to higher resistance.[6,7] However, this process is less probable than the first one as, in the present case, Bi substrate will soften earlier than Mn island-particles, and we will have to consider agglomeration of rigid Mn particles due to larger substrate mobility at higher temperatures.

From the nature of the curves in Fig. 1, it can concluded that for Bi/Mn weight ratio 2·63 maximum amount of Bi and Mn react to form MnBi, because the curve almost coincides with Skalsky's

curve, shown by broken lines in Fig. 1, wherein the curve shows almost constant R/R_{NA} value up to 150°C, slow decrease up to 250°C and constant final R/R_{NA} value of about 0·5.[1] The curves with other two compositions show a different trend, specially in their final R/R_{NA} values, thus providing the required predictive control to differentiate composition 2·63 films from others. Also the curve of composition 3·37 shows a peak, giving one more additional control. The error bars in Fig. 1 indicate that both these controls appear to be outside the error limits.

References

1. Skalsky M & Jurak K, *Thin Solid Films*, 34 (1976), 239.
2. Telesnin R V, Baranov A K, Grishechkin M I & Zavartsev Yu D, *Phys. Status Solidi (a)*, 24 (1974), 691.
3. Vand Vladmir, *Proc. phys. Soc. Lond.*, 55 (1943), 222.
4. Chopra K L, *Thin film phenomenon* (McGraw-Hill, New York), 340.
5. Naugebaur C A, *Trans. 9th Natl. Vac. Symposium* (MacMillan Co., New York), 1962, 45.
6. Maissel L I & Glang R, *Handbook of thin film technology* (McGraw-Hill, New York), 13-30.
7. Belser R B & Hicklin W H, *J. appl. Phys.*, 30 (1959), 313.

Behaviour of Screw-like Dislocations near an Interface in the Presence of Lattice Frictional Forces—Three Dislocations

N K GILRA

Basic Sciences Department, Higher Petroleum Institute
P O Box 201, Tobruk, Libya

Behaviour of three screw-like dislocations near an interface in the presence of lattice frictional forces has been analyzed taking into consideration the previous history. It has been shown that while three like-dislocations behave like a super-dislocation at infinite stress, two like-dislocations do not.

In previous communications, Gilra[1,2] has analyzed the behaviour of two screw-like dislocations near an interface in the absence and presence of the lattice frictional forces separately. Here the behaviour of three screw-like dislocations near the interface is analyzed in the presence of lattice frictional forces exactly in the same manner and under the same stress conditions as in Ref. 2.
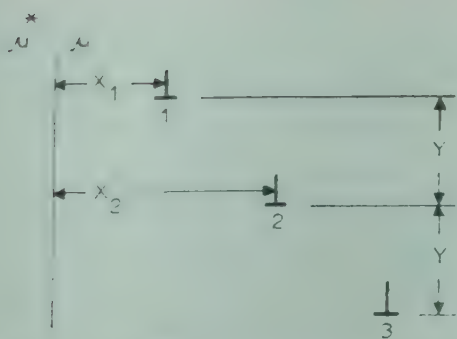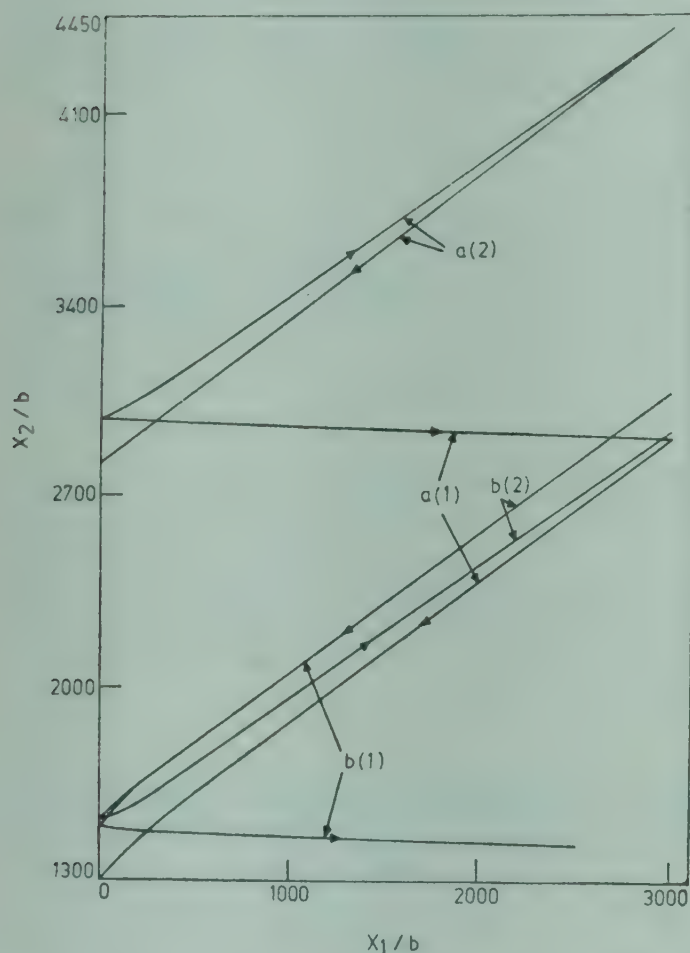
Fig. 1—Three dislocations near an interface

Fig. 2—Variation of X_2 with X_1 for three screw dislocations near an interface [Curves a(1) and a(2) represent the forward direction motion of dislocation 1 being done first under the first and second stress condition respectively.]

We consider three like dislocations near the interface as shown in Fig. 1 in a crystal containing no other dislocations with vertical separation (Y) as $200b$, where b is the Burgers vector of the dislocation. All the dislocations have the same Burgers vector. X represents the horizontal separation of the dislocation from the interface as shown in Fig. 1. The values of X_1 are varied from 1 (very close to the interface) to 3000 (infinite distance from the interface) in the forward direction of motion of dislocation 1 or from 3000 to 1 in the backward direction of motion. Two different cases are considered here. In case (i), forward direction of motion of dislocation 1 in gradual steps take places first and

backward direction of motion is considered of afterwards. In case (ii), the procedure of case (i) is reversed. Different values of applied stress (τ_a) and frictional stress (τ_f) have been used in computation. No stable equilibrium configurations are possible for $\tau_f < \tau_a$. Two sets of results are obtained under different stress conditions. The first stress condition is when τ_f is of the order of τ_a and the second stress condition is when $\tau_f \gg \tau_a$.

Under the first stress condition, when X_1 is increased from 1 to 3000, X_2 decreases uniformly at a slow rate but when the cycle is repeated by decreasing X_1, X_2 decreases at a uniform faster rate till the dislocation 1 is close to the interface as shown in Fig. 2. Dislocations pass each other in both the directions of motion of dislocation 1. Under the second stress condition, X_2 increases uniformly when X_1 is increased from 1 to 3000. When the dislocation 1 is brought back to the interface, X_2 decreases uniformly. There is a slight deviation from the uniform rate of variation in X_2 when the dislocation 1 is close to the interface in both the paths. Dislocations do not pass each other. The force due to internal stress on dislocation 1 has been computed as in Ref. 2 and is plotted in Fig. 3 for both the stress conditions. Under the first stress condition,
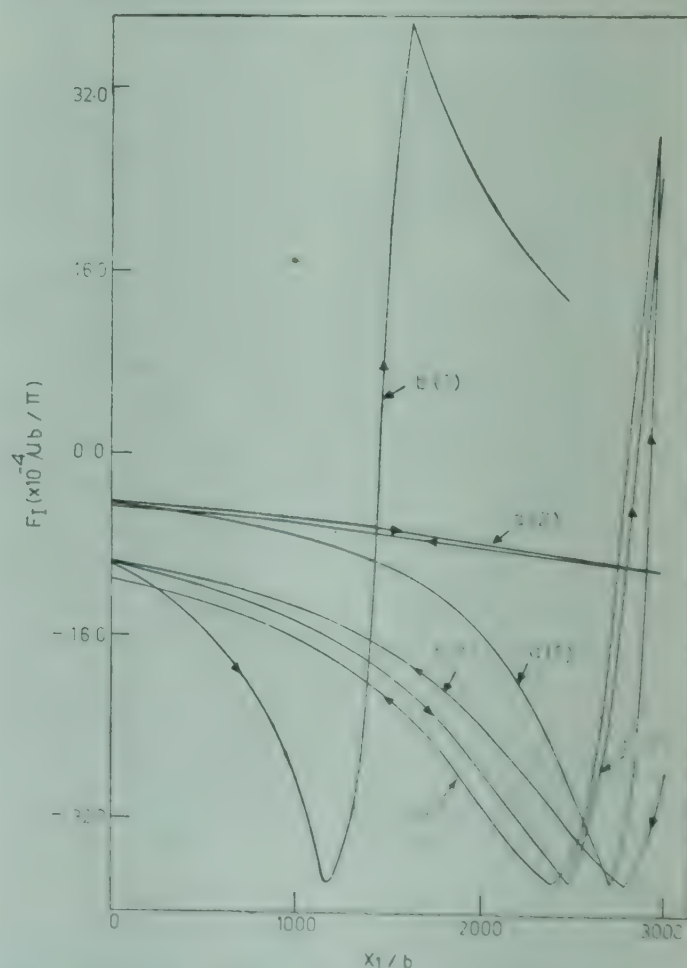

Fig. 3—Variation of force due to internal stress on dislocation 1 for three screw dislocations near an interface [Curves a(1), a(2), b(1) and b(2) have the same meaning as in Fig. 2]

this force decreases attains a minimum and changes sign as X_1 is increased from 1 to 3000. This force also changes sign, decreases to a minimum value and starts increasing as X_1 is decreased from 3000 to 1. This rate of increase of the force is less than the rate of decrease when X_1 is increased from 1 to 3000. Under the second stress condition, the force due to internal stress on dislocation 1 decreases very slowly and does not change sign when X_1 is varied from 1 to 3000. This force increases at a slow rate when the cycle is repeated with decreasing X_1. Cross slip force on dislocation 1 has also been computed as in Ref. 2 and is plotted in Fig. 4 for both the stress conditions. Under the first stress condition, the cross slip force on dislocation 1 increases slowly first, then sharply rises to a maximum and falls when X_1 is increased from 1 to 3000. The cross slip force increases, attains a maximum and decreases sharply first and then slowly when the cycle is repeated with decreasing X_1. Under the second stress condition, the cross slip force increases continuously but very slowly when X_1 is increased from 1 to 3000. This force decreases with approximately similar rate when X_1 is decreased from 3000 to 1.

Computations for the equilibrium configuration of dislocations are also made for case (ii) under the different stress conditions and results are shown in Fig. 2. Under the first stress condition, X_2 decreases at a uniform rate when X_1 is decreased from 3000 to 1 except when the dislocation 1 is near to the interface. Dislocations do not pass each other. When the cycle is repeated, X_2 continues to decrease at a much slower uniform rate except when dislocation 1 is close to the interface. Dislocations pass each other. There is no equilibrium configuration after X_1 has reached a value of 2500. Under the second stress condition, the results for X_2 are similar as in the first stress condition when X_1 is decreased from 3000 to 1 except when dislocation 1 is close to the interface. But there is a much faster uniform increase in X_2 when the cycle is retraced and dislocations pass each other. Under the first stress condition the force due to the internal stress on dislocation 1 has been computed and is shown in Fig. 3. This force increases when X_1 is decreased from 3000 to 1 and decreases, attains a minimum and changes sign as the cycle is repeated by increasing X_1. Under the second stress condition, results for the force due to internal stress are similar as in the first stress condition except when dislocation 1 comes very close to the interface, when X_1 is decreased from 3000 to 1. This force decreases, attains a minimum value and changes its nature as the cycle is repeated by increasing X_1 similarly as in the first
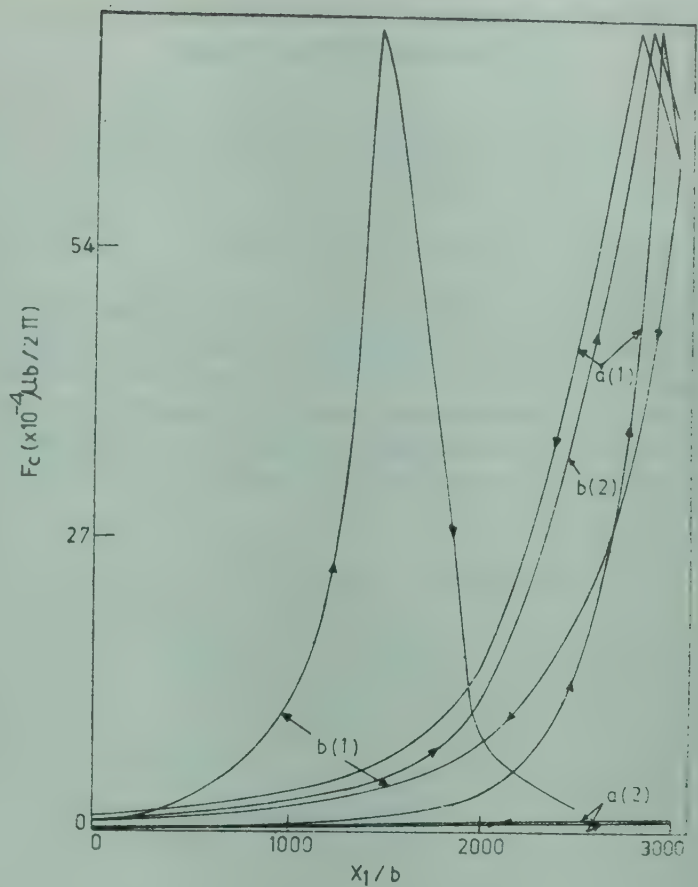

Fig. 4—Variation of cross slip force on dislocation 1 for three screw dislocations near an interface [Curves a(1), a(2), b(1) and b(2) have the same meaning as in Fig. 2.]

stress condition. The cross slip force on the dislocation 1 (Fig. 4) decreases quite rapidly initially when X_1 is close to 3000 and then slowly, when X_1 is close to 1. This force increases, attains a maximum rapidly and then falls as X_1 is increased from 1 to 3000. Under the second stress condition, the values of cross slip force are same as in the first stress condition when X_1 is decreased from 3000 to 1. The cross slip force increases, attains a maximum value and then decreases as in the first stress condition when the cycle is repeated.

For three like dislocations, different results are obtained for the different stress conditions whereas results are independent of stress conditions for two like dislocations.[2] Three like dislocations also pass one another very close to superdislocation at infinite stress, whereas two like dislocations never behaved like a superdislocation. By superdislocation, we mean that in the first stress condition, dislocation 2 remains almost stationary while the dislocation 1 moves from infinity to interface or vice versa. Therefore dislocation 2 behaves like a superdislocation.

References
1. Gilra N K, *Phys. Status Solidi*, a34 (1976), 79.
2. Gilra N K, *Phys. Status Solidi*, a40 (1977), 685.

A Function Generator Using Integrated Circuits for Mössbauer Effect Work

B R Pushpalatha & N G Puttaswamy

Department of Physics, Bangalore University
Bangalore 560 001

A function generator which can be used in Mössbauer effect work has been built using integrated circuits 8038 and 74121. Square, triangular, and sine wave outputs are provided. A synchronous pulse output required to trigger the channel reset of a multichannel analyzer is also provided. Mössbauer spectra taken using this function generator are found to be satisfactory.

Electromechanical transducers coupled with multichannel analyzers (MCA) are most widely used in Mössbauer spectroscopy.[1] The source is mounted on the transducer which is driven by a triangular wave so as to provide a parabolic motion to the source (constant acceleration mode) and the MCA is operated in the multiscaling mode for collecting the data. Kankleit has described a method[2] of deriving the driving waveform from the bistable output of the MCA. An ultrastable triangular-wave generator built using two operational amplifiers has been reported by Cohen.[3]

In this note, we describe a function generator built using the integrated circuits *Intersill* 8038 (waveform generator) and 74121 (monostable multivibrator). The circuit diagram of the generator is shown in Fig. 1. A square, triangular or sine wave output may be selected with amplitude variation

from 0 to 0·8 V peak-to-peak. The frequency of the waveforms is continuously variable from 2-20 Hz and is given by[4]

$$f = 3(V_s - V_c)/2 \; R_c \, C \, V_s$$

where the quantities R_c, $R_d = R_c$, V_s and V_c are indicated in Fig. 1. The unit can also be used as a ramp generator by choosing either R_c or R_d to be small. Two trimming potentiometers R_1 and R_2 are adjusted[5] to reduce the harmonic distortion of the sine wave to a value around 0·5%. The synchronous-trigger pulse, one for each cycle of the driving waveform, is generated by 74121 which is triggered by the square wave from 8038. The amplitude of the trigger pulse is 4V and the pulse width is set at 7 μsec.
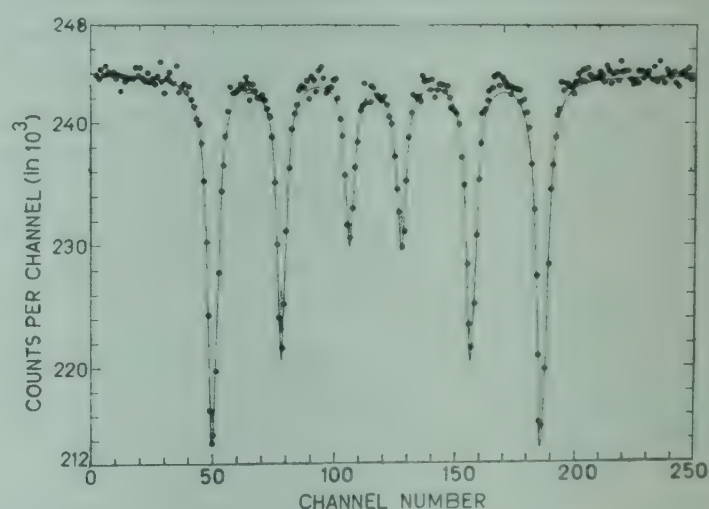

Fig. 2—Mössbauer spectrum of natural iron taken using the function generator of Fig. 1 [Velocity increases linearly with the channel number. The solid line is a computer fit to the spectrum]
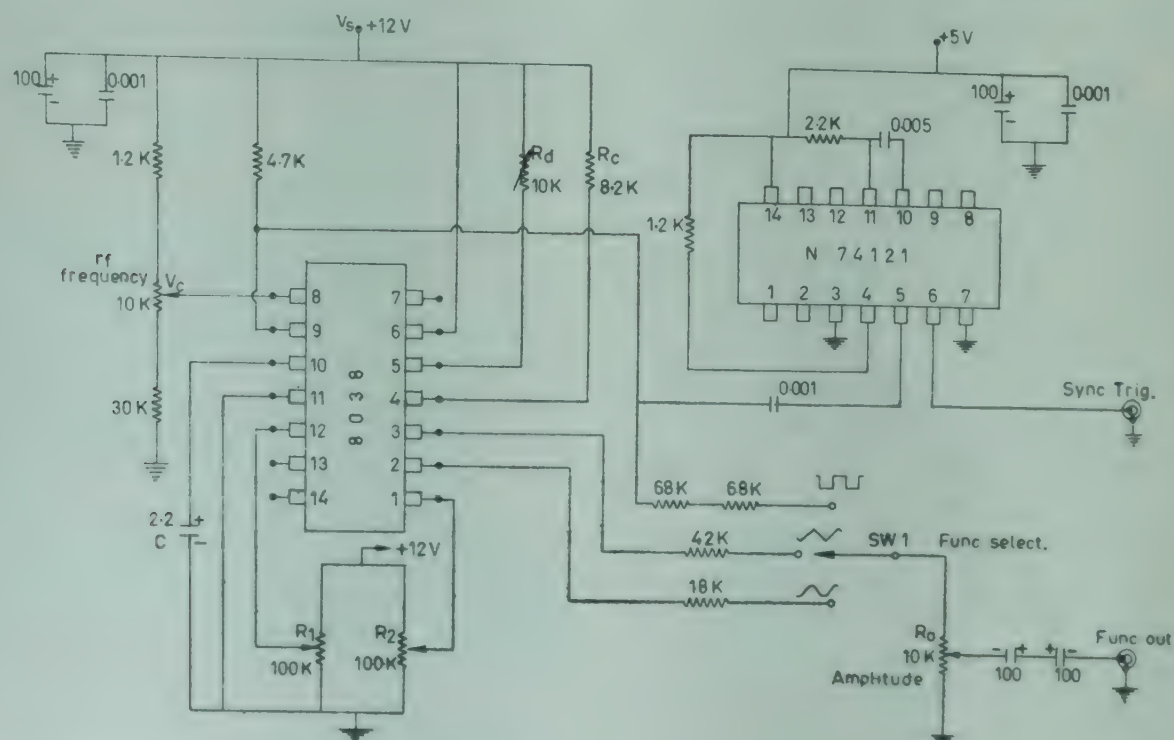

Fig. 1—Circuit diagram of the function generator [R_f and R_a are ten-turn potentiometers; R_d is a fourteen-turn trimming potentiometer. All capacitor values are in μF]

The triangular wave at a frequency of 10Hz is used to drive a transducer and the synchronous pulse is used to trigger the channel reset of the MCA operated in multiscaling mode. The transducer and the MCA were supplied to us by Electronics Corporation of India, Limited. The Mössbauer spectrum of an iron absorber taken with a ^{57}Co (Pd) source is shown in Fig. 2; a six-Lorentzian computer fit to the spectrum is shown by the solid line. The linewidth of the resonance peaks is approximately 0·35 mm/sec and, the linearity and stability are found to be satisfactory. The spectra taken with sine wave as the driving waveform are also fairly good and the observed line widths are of the same order as in the case of the triangular wave.

References
1. Wertheim G K, *Mössbauer Effect : Principles and applications*, (Academic Press, New York), 1964.
2. Kankleit G E, *Rev. scient Instrum.*, 35 (1964), 195.
3. Cohen R L, *Rev. scient Instrum.*, 37 (1966), 260.
4. Clayton G B, *Linear integrated circuit applications* (MacMillan, London), 1975, 113.
5. Flint E F, *Practical electronics*, 14 (1978), 666.

Infrared Absorption Spectra of 2,3,4- ; 2,4,5- & 2,4,6-Trichloroaniline

Nitish K Sanyal*

Department of Physics, University of Gorakhpur
Gorakhpur 273 001

&

R K Goel

Department of Physics, D N College, Meerut 250 002

The infrared absorption spectra of 2,3,4- ; 2,4,5- and 2,4,6-trichloroaniline have been recorded on Perkin-Elmer spectrophotometer in the region 250-4000 cm^{-1} in KBr, Nujol mull and in CS$_2$/CCl$_4$ and CHCl$_3$ solutions. The spectra have been analyzed assuming C_s/C_{2v} point group symmetry and the observed bands have been tentatively assigned to different fundamental modes. A correlation of the observed fundamentals in different phases has also been made.

The vibrational spectra of aniline have already been studied[1-10] in detail. Singh *et al.*[11] have reported the infrared spectra of a large number of mono-, di-, tri- and tetra-substituted anilines. So far, no work seems to have been carried out on the IR spectra of 2,3,4- and 2,4,6-TCA (TCA stands for tri-chloroani-

line). Thus the present investigation aims at giving the complete vibrational assignment of the frequencies of these molecules. Moreover, in order to check the assignment of C—Cl stretching frequencies and looking for any frequency shift, the spectra have also been studied in CS$_2$/CCl$_4$ and CHCl$_3$ solutions in addition to solid phase (KBr) and Nujol mull spectra. Tripathi and Pandey[7] have studied the IR spectra of 2,4,5- TCA in KBr in the region 200 to 700 cm^{-1} only. In view of the above, its spectra in various phases have also been studied and have been correlated with those of 2,3,4- and 2,4,6-TCA. Such a study may also throw light on some of the important frequencies, e.g. ν(C—N), ν(C—Cl), and will be helpful in the analysis of the electronic spectra of these molecules.

Pure chemicals obtained from M/s Tokyo Chemical Industry, Tokyo were used as such without further purification. The chemicals were in solid phase. The IR absorption spectra of 2, 3, 4; 2, 4, 5; and 2, 4, 6-TCA have been recorded on Perkin-Elmer spectrophotometer model-521 in solid phase (in KBr and nujol mull) and in CS$_2$/CCl$_4$ and CHCl$_3$ solutions in the region 250-4000 cm^{-1}. The observed bands have been calibrated with the help of the spectra of a thin sheet of polystyrene and are presented in Table 1. The C—Cl stretching frequencies have been compared with previous data in Table 2.

Assuming NH$_2$ group as single mass point and to lie in the plane of the ring, the title compounds 2, 3, 4-TCA and 2, 4, 5-TCA would belong to the C_s point group and 2,4,6-TCA to C_{2v} point group symmetry. The C—H stretching frequencies in benzene derivatives lie in the region 3000-3100 cm^{-1}. In the present case, out of the two C—H stretching frequencies, only one C—H vibration has been observed in each molecule without ambiguity, i.e. at 3094, 3084 and 3079 cm^{-1} in 2, 3, 4- ; 2, 4, 5- and 2, 4, 6-TCA respectively.

The NH$_2$ group will involve the symmetric and asymmetric N—H stretching vibrations. In the case of nearly all primary aromatic amines, two bands occur in the region 3300-3500 cm^{-1} [Ref. 12]. In the three molecules presently under study, the strong bands at 3504, 3464 and 3514 cm^{-1} respectively have been assigned to N—H asymmetric stretching vibration and those at 3424, 3374 and 3434 cm^{-1} respectively to N—H symmetric stretching mode. These symmetric and asymmetric frequencies of the present molecules also obey the empirical relation, $ν_{sym} = 345·53 + 0·876 ν_{asym}$ proposed by Bellamy and Williams.[13] It has been pointed out by Bellamy[12] that, in N-octamide in CHCl$_3$ solution, the NH$_2$ free

*Address to whom all correspondence should be made

Table 1—Assignment of Fundamental Vibrational Frequencies of Trichloroanilines*

(all values in cm^{-1})

2,3,4-Trichloroaniline				2,4,5-Trichloroaniline				2,4,6-Trichloroaniline				Assignment
KBr	Nujol-mull	CS_2/CCl_4	$CHCl_3$	KBr	Nujol-mull	CS_2/CCl_4	$CHCl_3$	KBr	Nujol-mull	CS_2/CCl_4	$CHCl_3$	
—	3504(s)	3514(vvs)	3519(vs)	3464(sb)	3464(m)	3514(vs)	3509(vvs)	—	3514(vs)	3514(vs)	3519(vvs)	ν(N—H) asym.
—	—	—	—	—	—	—	—	3464(ms)	3474(m)	—	—	ν(N—H)
3424(vs)	3414(vs)	3419(vvs)	3419(vs)	3374(vs)	3374(s)	3419(vs)	3414(vs)	3434(s)	3414(vs)	3414(vvs)	3414(vs)	ν(N—H) sym.
3324(vs)	—	—	—	—	—	—	—	3374(ms)	3384(ms)	—	—	ν(N—H)
—	—	—	—	—	—	—	—	3314(ms)	3324(m)	—	—	ν(N—H)
3094(w)	3099(w)	3059(mb)	—	3084(vw)	—	—	—	3079(vvw)	—	3099(ms)	—	ν(C—H)
1602(vvs)	1596(vvs)	1604(vvs)	1609(vvs)	1601(vs)	1596(vsb)	1609(vvs)	1609(vvs)	1606(vsb)	1604(vs)	1604(vs)	1604(vs)	ν(C—C), NH₂ scissoring
1566(vw)	1576(sh)	—	—	—	—	—	—	1566(s)	1578(ms)	—	1584(m)	ν(C—C), e_{2g} (1595)
—	1506(vw)	1539(m)	—	1501(vw)	1501(vw)	—	1549(mw)	1501(vw)	1551(vs) 1524(sh)	—	1554(s)	ν(C—C), e_{1g} (1485)
1457(vvs)	1457(vsb)	1465(vvs)	1465(vs)	1472(sb)	1442(vvsb)	1470(vvs)	1457(vvs)	1462(vvs)	1452(vvsb)	1470(vvs)	1470(vs)	ν(C—C), e_{1u} (1485)
1392(vvs)	1367(vsb)	1400(vvs)	1400(m)	1382(vs)	1367(vvs)	1386(vs)	1387(vvs)	1392(vs)	1377(vs)	1400(s)	1400(s)	ν(C—C), b_{2u} (1310)
1297(s)	1297(m)	1312(vs)	1313(s)	1292(ms)	1287(mb)	—	1280(msb)	1297(s)	1310(s)	1302(s)	1295(sb)	ν(C—N)
1282(s)	1277(ms)	1280(vs)	1285(m)	1277(ms)	1272(m)	—	—	1207(s)	1236 / 1218(m)	—	—	β(C—H)
1177(s)	1172(mb)	1180(ms)	—	1239(ms)	1237(m)	—	—	—	—	—	—	β(C—H)
1140(m)	1147(ms)	1150(ms)	—	1137(m)	1132(msh)	—	—	1137(vw)	1137(mb)	—	—	NH₂ twisting
1117(msb)	1117(msb)	—	—	1092(vvs)	1087(w)	—	—	1067(vvs)	1067(vs)	—	—	C—C—C trigonal bending, b_{1u} (1010)
987(vw)	967(msb)	—	—	962(vw)	959(mb)	—	935(msb)	—	972(ms)	—	—	γ(C—H)
912(vs)	909(vvs)	917(vs)	927(s)	932(s)	932(vs)	870(vs)	873(vvs)	862(sh)	864(s)	855(vvs)	860(vvs)	γ(C—H)
871(vvw)	867(vw)	—	—	863(vvs)	862(vs)	—	—	849(vvs)	854(vvs)	—	—	C—C ring breathing, a_{1g} (995)
812(vvs)	807(vvs)	797(vvs)	—	832(vs)	832(vs)	—	—	802(s)	802(s)	—	—	NH₂ wagging
775(vs)	775(vvs)	775(vvs)	—	—	767(mb)	—	—	777(vs)	782(vvs)	782(vvs)	—	ν(C—Cl)
712(ms)	717(vs)	—	—	733(s)	732, 717(vs)	735(s)	—	722(ms)	727(vvs)	725(vs)	—	ν(C—Cl)
697(ms)	—	680(s)	—	675(ms)	677(s)	675(vs)	—	705(s)	707(m)	705(s)	—	δ(C—C)
667(ms)	667(m)	667(m)	663(ms)	667(ms)	667(ms)	—	662(ms)	667(m)	667(m)	—	665(msb)	ν(C—Cl)
637(sh) 627(vw)	632(vsb)	—	—	623(m)	639(vw)	—	—	647(w) 612(w)	612(m)	—	—	C—C in-plane bending, e_{2g} (608)
572(s)	572(vs)	580(ms)	580(sb)	—	547(m)	—	553(m)	552(vs)	559(vs)	560(s)	561(s)	C—C in-plane bending, e_{2g} (608)

Table—1 Assignment of Fundamental Vibrational Frequencies of Trichloroanilines*
(all values in cm⁻¹) (condt.)

2, 3, 4-Trichloroaniline				2, 4, 5-Trichloroaniline				2, 4, 6-Trichloroaniline				Assignment
KBr	Nujol-mull	CS₂/CCl₄	CHCl₃	KBr	Nujol-mull	CS₂/CCl₄	CHCl₃	KBr	Nujol-mull	CS₂/CCl₄	CHCl₃	
492(ms)	487(s)	500(s)	—	—	472(vvw)	—	—	—	472(sb)	475(sb)	—	C—C out-of-plane bending, e_{2u} (404)
397(ms)	396(ms)	—	—	396(ms)	—	—	395(w)	395(m)	397(ms)	390(vvsb)	—	C—C out-of-plane bending, e_{2u} (404)
375(m)	372(m)	377(vs)	—	373(m)	375(m)	—	375(ms)	372(m)	372(ms)	—	—	β(C—NH₂)
332(w)	332(w)	—	334(mw)	332(m)	332(w)	335(vw)	335(m)	332(vw)	332(m)	—	—	β(C—Cl)
327(m)	—	—	325(m)	325(m)	325(vw)	327(m)	327(mw)	325(vw)	325(m)	325(w)	325(w)	β(C—Cl)
314(w)	312(vw)	—	317(mw)	312(w)	312(vw)	—	315(vw)	312(vw)	312(w)	—	—	γ(C—NH₂)
299(vw)	297(vw)	—	—	299(m)	298(vw)	300(ms)	300(vw)	397(m)	297(m)	300(vs)	300(w)	β(C—Cl)

*Intensities are shown in parenthesis against each wavenumber.

s = strong, vs = very strong, vvs = very very strong, b = broad, m = medium, ms = medium strong, w = weak, vw = very weak, vvw = very very weak, sh = shoulder, ν = stretching, β = in-plane bending, γ or δ = out-of-plane bending.

absorption occurs at 3530 and 3415 cm⁻¹, but it also shows additional bands at 3498, 3345, 3300 and 3182 cm⁻¹, which suggest the occurrence of different types of simultaneous association of free and bonded N—H bonds. In view of this, the strong bands observed at 3324 cm⁻¹ in 2, 3, 4-TCA and at 3464, 3374 and 3314 cm⁻¹ in 2, 4, 6-TCA have also been attributed to N—H stretching frequencies.

The appearance of a group of four bands between 1400 and 1650 cm⁻¹ in the spectra of substituted benzenes represent the characteristic skeletal stretching modes. The NH₂ scissoring mode has been suggested to lie in the region 1590-1650 cm⁻¹ in nearly all the primary aromatic amines.[12,14] Thus the intermixing of NH₂ scissoring mode may take place with one of the components of e_{2g} (1595) mode of benzene. Hence, the very strong bands observed at 1602, 1601 and 1606 cm⁻¹ in the three molecules respectively have been assigned to C—C stretching or NH₂ scissoring mode. The other bands corresponding to e_{2g} and e_{1u} modes are shown in Table 1. These assignments are in agreement with the assignments made by earlier workers.[6,8]

In substituted anilines, the strong C—NH₂ stretching vibration appears near 1300 cm⁻¹ [Refs. 11, 15, 16] but the C—C stretching mode corresponding to b_{1u} (1310 cm⁻¹) mode of benzene also lies in the same region and is not affected by substitution. Thus, due to near equality of these two vibrations, these modes may be modified. Hence the bands observed at 1297, 1282 cm⁻¹ in 2, 3, 4-TCA, at 1292 and 1277 cm⁻¹ in 2, 4, 5-TCA and at 1297 cm⁻¹ in 2, 4, 6-TCA have been assigned to (C—C) and (C—N) stretching modes.

It has been pointed out by several workers that under reduced symmetry C_s or C_{2v}, the C—C ring breathing a_{1g}(995 cm⁻¹) and C—C—C trigonal bending b_{1u} (1010 cm⁻¹) vibrations of benzene give rise to combined modified modes. As a result of this, one of the modified modes is reduced to about 800 cm⁻¹ while the other keeps itself around 1000 cm⁻¹. The bands corresponding to these modes are shown in Table 1 which find support from the assignments made by Sharma and Dwivedi,[17] Tripati et al.[6] and Sanyal et al.[8] in substituted anilines.

Many workers have assigned the C—Cl stretching mode in the region 550-750 cm⁻¹. The C—Cl stretching frequencies observed in the case of title compounds have been compared with other chloroanilines and trichlorophenols[18,19] in Table 2. Attempts were made to check the assignments of the C—Cl stretching frequency by taking the spectra in different solutions and looking for any frequency shift as has been done by Nabumi Oi and Coetzee.[20]

Table 2—Correlation of C—Cl Stretching Frequencies (All values in cm^{-1})

2,4,5-TCA [Ref. 7]	2,4,6-TCP [Ref. 19]	2,3,5-TCP [Ref. 19]	2,4,5-TCP [Ref. 19]	2,3,4-TCP [Ref. 18]	3,3,6-TCP [Ref. 18]	2,3-DCP [Ref. 18]	2,3,4-TCA	2,4,5-TCA	2,4,6-TCA
							(present work)		
	735(vvs)	700(ms)	740(vs)		720	744	712(ms)	733(s)	722(ms)
680(s)	670(ms)	670(ms)	690(vs)	685		704	697(ms)	675(ms)	705(s)
	620(mw)	605(vs)	620(mw)	670	623		637(sb)	623(m)	647(w)

DCP and TCP stand for di- and tri-chlorophenol respectively.

but the evidence is not conclusive. The bands observed at 332, 327 and 299 cm^{-1} in 2, 3, 4-TCA at 332, 325 and 299 cm^{-1} in 2,4,5-TCA and at 332, 325 and 297 cm^{-1} in 2, 4, 6-TCA, have been assigned to C—Cl in-plane bending modes. More intense bands have been observed in solution spectra corresponding to this mode.

One of the authors (RKG) is thankful to the University Grants Commission, New Delhi, for financial assistance and to Dr S N Sharma, Indian Institute of Petroleum, Dehra Dun, for useful discussions.

References

1. Evans J C, *Spectrochim. Acta*, 16 (1960), 428.
2. Green J H S, *Spectrochim. Acta*, 26A (1970), 1503, 1523, 1913.
3. Ferguson E E, Hudson R L, Nielson J Rud & Smith D C, *J. chem. Phys.*, 21 (1953), 1457, 1464, 1470 & 1727.
4. Verma P K, *Indian J. pure appl. Phys.*, 6 (1968), 144.
5. Singh S N & Singh N L, *Indian J. pure appl. Phys.*, 7 (1969), 250.
6. Tripathi G N R, Tewari B N & Verma R M, *Indian J. pure appl. Phys.*, 13 (1975), 608.
7. Tripathi G N R & Pandey V M, *Indian J. pure appl Phys.*, 13 (1975), 860.
8. Sanyal Nitish K, Srivastava S L & Goel R K, *Indian J. pure appl. Phys.*, 16 (1978), 719.
9. Tewari S K & Upadhya K N, *Indian J. pure appl. Phys.*, 6 (1968), 698.
10. Goel R K, Gupta S K & Sharma S N, *Pramana*, 11 (1978), 541.
11. Singh V B, Singh R N & Singh I S, *Spectrochim. Acta*, 22 (1966), 927.
12. Bellamy L J, *Infrared spectra of complex molecules* (John-Wiley, New York), 1959.
13. Bellamy L J & Williams R L, *J. chem. Soc.*, 3 (1956), 2753.
14. Rao C N R, *Chemical applications of infrared spectroscopy* (Academic Press, New York), 1963.
15. Srivastava S L, *Spectroscopic studies of some di- & tri-substituted benzenes*, Ph D thesis, Gorakhpur University, Gorakhpur, 1968.
16. Tripathi L N, *Vibrational and electronic absorption spectra of some di-derivatives of benzenes*, Ph D thesis, Gorakhpur University, Gorakhpur, 1966.
17. Sharma S N & Dwivedi C P D, *Indian J. pure appl. Phys.*, 13 (1975), 670.
18. Tripathi G N R & Ram S, *Indian J. pure appl. Phys.*, 12 (1974), 529.
19. Pandey S M & Singh S J, *Indian J. Phys.*, 48 (1974), 961.
20. Nabumi O I & Coetzee J F, *J. Am. chem. Soc.*, 91 (1969), 2473.

Bond Polarizability Derivatives & Force Constants of Some XY$_3$ Pyramidal Type Molecules & Ions

V K RASTOGI

Department of Physics, Lajpat Rai College, Sahibabad (Ghaziabad) 201 005

&

U P VERMA & A N PANDEY

Department of Physics, Meerut College, Meerut 250 001

Bond polarizability derivatives and force constants of MCl$_3$ (M = N, P, As, Sb), SiF$_3$, OH$_3^+$, SH$_3^+$, have been reported and are briefly discussed. It is found that the bond polarizability derivative is inversely proportional to the stretching force constant of a bond containing chlorine and a VA group element.

Cazzoli and coworkers[1-8] have, recently, studied some molecular parameters for the trichlorides of VA group elements in different papers. Milligan et al.[4] have observed the infrared spectra of SiF$_3$ in argon and nitrogen matrices and suggested that the molecule is pyramidal with an angle 71° between the molecular axis and a Si-F bond. This structure has also been established by ESR studies.[5] In the present communication, it is aimed to study the bond polarizability derivatives and force constants for the trichlorides of VA group elements and SiF$_3$, SH$_3^+$, & OH$_3^+$. An attempt has been made to obtain a relation between bond polarizability derivative and stretching force constant.

The pyramidal XY_3 type system belongs to C_{3v} point group and gives rise to four fundamental modes of vibration, which can be distributed in different species as

$$\Gamma_{\text{vib}} = 2A + 2E$$

All the four fundamentals are infrared and Raman active.

The bond polarizability derivatives $(\partial \bar{\alpha}/\partial R)$ have been computed using the relation[6]

$$\partial \bar{\alpha}/\partial R = \frac{1}{3} (n/2) (\sigma/a_0) A_{12} R^3$$

where $(n/2)$, σ, a_0 and R are the bond order, Pauling covalent character, first Bohr radius and interatomic distance respectively. A_{12} is the root mean square delta-function strength for heteronuclear bond determined by the relation $A_{12} = \sqrt{A_1 A_2}$, where A_1 and A_2 are the delta-function strengths of the atoms 1 and 2 forming the bond. Wilson's GF matrix method[7] has been used to determine the force constants and second order secular equations are solved by L-F approximation method.[8]

The spectral and structural data used in the present study are collected in Table 1. In the calculation of bond polarizability derivatives, recent values of A, reported by Verma and Pandey,[9] have been used and the results are listed in Table 2. It is apparent from Table 2 that there is a regular trend in the variation of bond polarizability derivatives from nitrogen trichloride to antimony trichloride, i.e.

$$\bar{\alpha}'_{\text{NCl}} < \bar{\alpha}'_{\text{PCl}} < \bar{\alpha}'_{\text{AsCl}} < \bar{\alpha}'_{\text{SbCl}}$$

Table 1—Vibrational Wavenumbers (in cm^{-1}), Bond Angle and Interatomic Distances (in Å)

Mol./Ion	$\nu_1 (a_1)$	$\nu_2 (a_1)$	$\nu_3 (e)$	$\nu_4(e)$	Bond angle (YXY)	R	Ref.
NCl₃	540·5	349·0	643·0	257·5	107°22′	1·7593	1
PCl₃	512·0	260·5	505·0	186·8	100°12′	2·0450	1
AsCl₃	420·0	193·0	396·0	151·0	98°54′	2·160	2
SbCl₃	360·0	158·0	330·0	134	97°11′	2·3217	3
SiF₃	832·0	404·0	954·0	290·0	111°54′	1·549	4
OH₃⁺	330·00	900·0	3150·0	1620·0	110°		10
SH₃⁺	2520·0	1028·0	2520·0	1180·0	110°		10

Table 2—General Valence Force Field Constants (in 10⁺N/m) and Bond Polarizability Derivatives (in Å²)

Mol./Ion	f_{rr}	f_{rr}	f_{α}	$f_{\alpha\alpha}$	$f_{r\alpha}$	$f'_{r\alpha}$	$\partial\bar{\alpha}/\partial R$	Ref.
NCl₃	2·733	0·400	0·413	0 056	0·414	0·086	2·642	
	2·630	0·260	0·439	0·081	0·393	0·033		1
PCl₃	2·706	0·357	0·277	0·039	0·206	0·056	2·880	
	2·545	0·286	0·281	0·040	0·120	0·037		1
AsCl₃	2·378	0·234	0·206	0·027	0·091	0·022	3·018	
	2·308	0·189	0·206	0·028	0·051	—0·007		2
SbCl₃	1·892	0·178	0·168	0·015	0·039	0·017	3·457	
	1·745	0·154	0·182	0·015	0·098	—0 005		3
SiF₃	5·840	0·780	0·460	0·203	0·230	0·055	0·507	
OH₃⁺	5·740	0·301	0 531	— 0·076	0·046	— 0·012		
SH₃⁺	3·658	0·038	0·412	0·095	0·016	0·000		

Internal force constants in GVFF model collected in Table 2 are compared with the results reported by others.[1-3] It is apparent from Table 2 that the agreement is satisfactory. It is also obvious that all the force constants show decreasing tendency in the order $NCl_3 > PCl_3 > AsCl_3 > SbCl_3$. An inspection of the results further shows that the variation in the stretching and bending force constants is smaller than that in the interaction force constants. This can be explained on the basis that for NCl_3 and PCl_3 where $m_z < m_y$, mass coupling will be more than for $AsCl_3$ and $SbCl_3$ where $m_x > m_y$.

A comparative study of the bond polarizability derivatives and stretching force constants (Table 2) for the trichlorides of VA group elements shows that the trends of variation of the two parameters are opposite in nature. The average value of the product of the bond polarizability derivatives (α') and stretching force constants (f_r) comes out to be 7·183. Deviations of the product of $\bar{\alpha}'$ and f_r for NCl_3, PCl_3, $AsCl_3$ and $SbCl_3$ from the average value of their products are respectively 0·018, 0·620, 0·000 and −0·649. Since the average of the deviations is very very small, we conclude that the bond polarizability derivative of a bond is inversely proportional to its stretching force constant.

References

1. Cazzoli G, *J. molec. Spectrosc.*, **53** (1974), 37.
2. Cazzoli G, Forti P & Lunelli B, *J. molec. Spectrosc.*, **69** (1978), 71.
3. Cazzoli G & Caminati W, *J. molec. Spectrosc.*, **62** (1976), 1.
4. Milligan D E, Jacox M E & Guillory W A, *J. chem. Phys.*, 49 (1968), 5530.
5. Hasegawa A, Sogabe K & Miura M, *Molec. Phys.*, **30** (1975), 1889.
6. Lippincott E R & Nagarajan G, *Bull. chem. Soc. Belg.*, 74 (1965), 551.
7. Wilson E B (Jr), Decius J C & Cross P C, *Molecular vibrations* (McGraw-Hill, New York), 1955.
8. Pandey A N, Sharma D K, Verma U P, Gupta S L & Singh B P, *Indian J. pure appl. Phys.*, 14 (1976), 815.
9. Verma U P & Pandey A N, *Z. Naturf*, 33a (1978), 495.
10. Christe K O, Schack C J & Wilson R D, *Inorg. Chem.*, 14 (1975), 2224.

Crystal Growth of Transition Metal Oxides from Potassium Pyrosulphate Flux

K RAVINDRAN NAIR & T R NARAYANAN KUTTY

Department of Inorganic and Physical Chemistry
Indian Institute of Science, Bangalore 560 012

Crystals of some transition metal oxides viz. NiO, ZnO, Fe_2O_3 and Mn_3O_4 have been grown from a $K_2S_2O_7$ flux. The crystals are found to be shiny, flaky and of 1 mm size.

Recently crystals of a number of materials are being grown by the flux method.[1] This has been mainly possible because of the fact that some flux material could be used to grow crystals of a wide variety of materials, e.g. PbO and PbF_2. In this note, we report the use of $K_2S_2O_7$ as a useful flux material for the growth of single crystals of a number of transition metal oxides.

In a typical experiment about 2 g of the oxide was mixed thoroughly with about 50 g of $KHSO_4$ or $K_2S_2O_8$ both of which on heating get converted to $K_2S_2O_7$. The mixture is heated, in a platinum vessel covered with a lid, to 1000°C in a box-type furnace with good controls. The operation should be done in a fume cupboard with good exhaust system to drive away the SO_3 evolved on heating. The melt is soaked at 1000°C for 5 hr. Then it is cooled down at the rate of 5°C/hr to 800°C and then to room temperature at the rate of 100°C/hr. During this period $K_2S_2O_7$ decomposes to K_2SO_4 according to

$$K_2S_2O_7 \rightarrow K_2SO_4 + SO_3$$

The K_2SO_4 is leached with warm water and crystals are separated.

The physical characteristics of the crystals of the oxides grown by this method are presented in Table 1, and photographs of some of the crystals are shown in Fig. 1.

A few experiments were carried out to throw some light into the basic processes involved in the crystal growth. The details and conclusions are as follows:

1. The end product of heating of $K_2S_2O_7$ at 1000°C is K_2SO_4. The conversion of $K_2S_2O_7$ to K_2SO_4 is complete in about 5 hr.

2. A few experiments carried out with K_2SO_4 as the starting flux material, keeping other experimental conditions the same, yielded no crystal.

3. A mixture of K_2SO_4 and iron sulphate $[Fe_2(SO_4)_3]$ was heated to 1000°C and allowed to remain at that temperature for 5 hr. During this period iron sulphate decomposes to give iron oxide, Fe_2O_3 and SO_3. When the mixture was cooled at the rate of 5°C/hr to 800°C and then rapidly to room temperature, flaky single crystals of Fe_2O_3 were obtained. The crystal size was 0·2 mm which is much smaller than those obtained when $KHSO_4$ was used as the starting flux material.

From the above results it is obvious that SO_3 present in the system facilitates the formation of a solution of oxide in the melt. More studies are required to ascertain its role.

There are very few flux inclusions in the crystals. The maximum amount of K_2SO_4 present in these crystals is 0·1%.

Some other advantages of $K_2S_2O_7$ flux are as follows:

1. Irrespective of the composition of the melt, the oxide is the only stable crystallized phase. No other unwanted compound is formed.

Table 1—Physical Characteristics of Transition Metal Oxide Crystals Grown from $K_2S_2O_7$ Flux

Oxide	Appearance	Size
NiO	Shining, greenish yellow flaky crystals	~ 1 mm
ZnO	mixture of yellowish white flaky crystals and	~ 1 mm
	hollow cylindrical crystals	~ 5-15 mm (length) ~ 0.5 mm (diam.)
Fe_2O_3	reddish brown, shining flaky crystals	~ 1 mm
Mn_3O_4	dark red, shining flaky crystals	~ 1 mm

Note: The identification of the oxides was confirmed by powder pattern and chemical analysis.

Fig.1—Photographs (× 23) of crystals prepared from $K_2S_2O_7$ flux: (a) nickel oxide, (b) manganese oxide (Mn_3O_4).

2. The flux is non-volatile. More studies are under way to use $K_2S_2O_7$ for the preparation of crystals of other oxide materials.

References
1. Wanklyn B M, Practical applications of flux growth by spontaneous nucleation in *Crystal growth*, edited by B R Pamplin (Pergamon Press, Oxford), 1975.

Force Constants of Some XY₄ Molecules by Modified Redington & Aljibury Method

M TRIPATHY, K C MISHRA & B S MOHANTY

Department of Physics, G M College, Sambalpur, (Orissa)

To calculate the parameter ϕ, the Redington and Aljibury method [*J. molec. Spectrosc.*, **37** (1971), 494] has been reformulated by choosing the triangular L-matrix ($L_{12} = 0$) as the initial L-matrix instead of $L_0 = A \Gamma^{1/2}$, as given in the original method. Force constants for halides of Sr, Ge, Sn, Ti, Zr, and Hf and, those of CH_4, GeH_4 and SnH_4 have been calculated in this formalism. The possibility of using the formalism to indicate the correct sign of ϕ is indicated.

In one of our recent calculations[1] on the parametric representation method developed on the basis of L-matrix approximation[2] we have indicated the importance of pre-knowledge of the sign of parameter ϕ when mean amplitude of vibration is to be used as additional vibration data. To obtain this information we thought it worthwhile to reformulate the Redington and Aljibury method[3] using the triangular L-matrix ($L_{12} = 0$) as the initial L-matrix. This approximate method is chosen in preference to other methods because of the fact that the constraint proposed on the basis of virial theorem in this method of calculation is a distinctly different condition from $L_{12} = 0$. Therefore, ϕ calculated by this formalism may indicate the correct sign, which will remove the ambiguity arising in exact force field studies using the mean amplitude of vibration. This formalism was used to calculate the force constants of halides of Si, Ge, Sn, Ti, Zr and Hf and, those of CH_4, GeH_4 and SnH_4. The calculated values of force constants of these molecules along with the observed frequencies and the values of ϕ are given in Table 1.

The following features regarding our calculated values of force constants are worth-noting:

(1) The parameters calculated in this formalism have been found to be close to zero.

(2) The calculated values of ϕ for Ge and Si show good agreement with those of the exact values obtained in the previous calculations.[1]

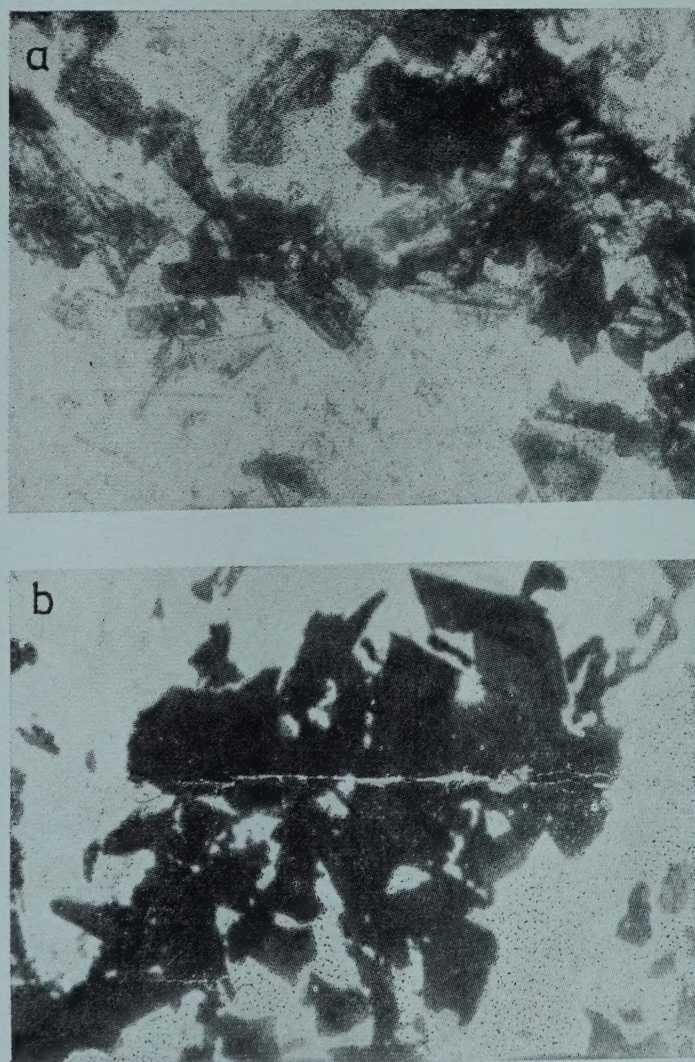(3) The values of ϕ for the halides of Ti, Zr, Hf, Ge and Si turn out to be almost the same ($1° \sim 2°$).

Table 1 —Force Constants (in mdyne/Å) of Some XY$_4$-Type Molecules

Molecule	Vibrational frequency, cm^{-1}		ϕ deg	F_{33}	F_{34}	F_{44}
CH$_4$	3008·75	1298·3	1	4·80	0·037	0·417
SiF$_4$	1031·8	389·35	4	5·69	0·150	0·433
SiCl$_4$	619·0	212·3	5	2·47	0·097	0·218
SiBr$_4$	494	133·6	3	1·99	0·152	0.166
SiI$_4$	404	88·8	5	1·12	0·0512	0 125
GeH$_4$	2195·0	846·0	0	2·81	0·00732	0·205
GeF$_4$	821·6	271·0	1	5 56	0·0809	0·273
GeCl$_4$	453·0	172	2	2·50	0·0814	0·173
SnH$_4$	1961·0	698·0	0	2·26	0·00313	0·141
SnCl$_4$	408·2	126·1	1	2·44	0·0329	0·105
TiCl$_4$	498	136	1	2·53	0·0671	0 0962
TiBr$_4$	393	88	1	2·16	0·0742	0·0762
ZrCl$_4$	418	113	1	2·33	0·0282	0·0784
ZrBr$_4$	315	72	1	2·073	0·0329	0·0583
ZrI$_4$	254	55	1	1·62	0·0424	0·045
HfCl$_4$	390	112	1	2·47	0·0112	0·0918
HfBr$_4$	273	71	1	2·16	0·02059	0·0677
HfI$_4$	224	63	2	1·86	0·0740	0·0740

It was observed by Ramaswamy et al.[4] that the method in its original form ($L0 = A\ \Gamma^{1/2}$) gives results as good as the exact force field for the boron trihalides. In the present calculation, the force constants are also satisfactory. This makes us hopeful to use the present formalism in extracting the true signs of ϕ at least for those types of molecules for which ϕ shows a similar trend. This can be used in choosing the correct ϕ, calculated from mean amplitude of vibration, when two values of ϕ are obtained with equal magnitude and opposite sign.[1]

The authors are extremely thankful to Dr K S R Murty, Principal, G M College for his kind encouragement during the work.

References

1. Mishra K C & Mohanty B S, *Indian J. pure appl. Phys.*, **15** (1977), 700.

2. Peacock C J & Muller A, *J. molec. Spectrosc.*, **26** (1968), 454.

3. Redington R L & Aljibury A L K, *J. molec. Spectrosc.*, **37** (1971), 494.

4. Ramaswamy K & Karunanithi S, *Acta Chim. hung.*, **87** (1975), 129.

Announcing completion of the series
THE WEALTH OF INDIA

An Encyclopaedia of Indian Raw Materials and Industrial Products, published in two series: (i) **Raw Materials**, and (ii) **Industrial Products**.

RAW MATERIALS

The articles deal with Animal Products, Dyes & Tans, Essential Oils, Fats & Oils, Fibres & Pulps, Foods & Fodders, Drugs, Minerals, Spices & Flavourings, and Timbers and other Forest products. Names in Indian languages, and trade names are provided.

For important crops, their origin, distribution, evolution of cultivated types, and methods of cultivation, harvesting and storage are mentioned in detail. Data regarding area and yield and import and export are provided. Regarding minerals, their occurrence and distribution in the country and modes of exploitation and utilization are given. The articles are well illustrated. Adequate literature references are provided.

Eleven volumes of the series covering letters A-Z have been published.

Vol. I (A-B) Rs. 25.00; Vol. II (C) Rs. 37.50; Vol. III (D-E) Rs. 40.00; Vol. IV (F-G) Rs. 25.00; Vol. IV : Suppl. Fish & Fisheries Rs. 10.50; Vol. V (H-K) Rs. 30.00; Vol. VI (L-M) Rs. 40.00; Vol. VI: Suppl. Livestock Rs. 60.00; Vol. VII (N-Pe) Rs. 30.00; Vol. VIII (Ph-Re) Rs. 70.00; Vol. IX (Rh-So) Rs. 83.00; Vol. X (Sp-W) Rs. 152.00; Vol. XI (X-Z) Rs. 102.00

INDUSTRIAL PRODUCTS

Includes articles giving a comprehensive account of various large, medium and small scale industries. Some of the major industries included are: Acids, Carriages, Diesel Engines, Fertilizers, Insecticides & Pesticides, Iron & Steel, Paints & Varnishes, Petroleum Refining, Pharmaceuticals, Plastics, Ship & Boat-building, Rubber, Silk, etc.

The articles include an account of the raw materials and their availability, manufacturing processes, and uses of products, and industrial potentialities. Specifications of raw materials as well as finished products and statistical data regarding production, demand, exports, imports, prices, etc., are provided. The articles are suitably illustrated. References to the sources of information are provided.

Nine volumes of the series covering letters A-Z have been published.

Part I (A-B) Rs. 20.00; Part II (C) Rs. 25.00; Part III (D-E) Rs. 25.00; Part IV (F-H) Rs. 25.00; Part V (I-L) Rs. 30.00; Part VI (M-Pi) Rs. 28.00; Part VII (Pl-Sh) Rs. 60.00; Part VIII (Si-Ti) Rs. 66.00; Part IX (To-Z) Rs. 80.00

Complete set is now available

Please Contact :

THE SALES & DISTRIBUTION OFFICER
PUBLICATIONS & INFORMATION DIRECTORATE, CSIR
HILLSIDE ROAD, NEW DELHI 110 012